LIGHT EMISSION FROM RARE EARTH-DOPED SILICON OXIDE THIN FILMS DEPOSITED BY ECR-PECVD

LIGHT EMISSION FROM RARE EARTH-DOPED SILICON OXIDE THIN FILMS DEPOSITED BY ECR-PECVD

By

JING LI

B.Sc., M.Eng. (TSINGHUA UNIVERSITY)

A Thesis

Submitted to the School of Graduate Studies

in Partial Fulfillment of the Requirements

for the Degree

Master of Applied Science

McMaster University

Master of Applied Science (2008)
(Department of Engineering Physics)

McMaster University
Hamilton, Ontario

TITLE: Light Emission from Rare Earth-Doped Silicon Oxide Thin Films Deposited by ECR-PECVD

AUTHOR: Jing Li, B.Sc., M.Eng. (Tsinghua University)

SUPERVISOR: Dr. Peter Mascher

NUMBER OF PAGES: x ii, 141

Abstract

Silicon oxide films (oxygen-rich or silicon-rich) doped with various rare-earth (RE) [cerium (Ce), terbium (Tb), europium (Eu) and erbium (Er)] elements have been by deposited by electron cyclotron resonance plasma-enhanced chemical vapour deposition (ECR-PECVD). The successful *in-situ* incorporation of high concentrations of RE elements has been confirmed by Rutherford backscattering spectrometry (RBS), and the optical properties of the films were analyzed by Photoluminescence (PL) spectroscopy.

Ce, Tb, Eu and Er related emission was observed from the films with corresponding doping and was found to be sensitive to RE concentration, the presence of Si nanoclusters (Si-ncs) and annealing induced structural evolution. The significant enhancement of Ce^{3+} emission in Ce-doped oxygen-rich films under annealing in flowing N_2 at 1200 ^{o}C was found to be related to the formation of cerium silicate whose presence was confirmed by Fourier transform infra-red (FTIR) spectra and high-resolution transmission electron microscopy (HR-TEM) images. The observation of intense Tb^{3+} emission from Tb-doped oxygen-rich films under nonresonant excitation revealed the presence of indirect excitation processes. The organic ligands introduced from the $Tb(tmhd)_3$ precursor during deposition was considered as the possible sensitizer. The presence of Si-ncs in Ce or Eu-doped silicon-rich films resulted in the quenching of both RE and Si-ncs PL, while in

Tb or Er-doped silicon-rich films the coupling between Si-ncs and RE ions can excite RE-related emission efficiently. The formation of Si-ncs with sizes of 2-3 nm in Tb-doped silicon-rich films under annealing in flowing N_2 at 1100 and 1200 ^{o}C was revealed by HR-TEM images.

Acknowledgements

I would like to thank my supervisor, Peter Mascher, not only for providing me the opportunity to work on this project, but also for his guidance and encouragement all the time.

Sincere thanks goes to Othman Zalloum for helping me with photoluminescence measurements on hundreds of samples and offering many valuable advices for the research work.

I would especially like to thank both Jacek Wojcik and Charlie Zhang not only for all the efforts and time they have contributed to film depositions but also for their willingness and patience in helping me understand many aspects of ECR-PECVD system.

I would like to acknowledge William. Lennard and Jack Hendriks from University of Western Ontario for their expert help in RBS measurements, Jim Garrett and Graham Pearson for technical support in annealing, Julia Huang and Fred Pearson for many hours TEM sample preparation training and the helps in obtaining TEM images, Zhilin Peng and Doris Stevanovic for many hours of clean room training, Doug Bruce for valuable discussion in potential gain measurement system set up, Tyler Roschuk, Darren Blakie, Chenglin Heng, Patrick Wilson and all other colleagues I co-worked with for all kinds of helps they have provided that related to this project.

I would like to thank the following organizations for providing the funding and making this research possible: the Ontario Photonics Consortium (OPC), Ontario Centre of Excellence (OCE), Centre for Photonics Fabrication Research (CPFR) and the Canadian Institute for Photonic Innovation (CIPI). I am also grateful for financial and technical support from Group IV Semiconductor Inc. (Kanata, Ontario) and Johnsen-Ultravac (Burlington, Ontario).

Finally, I would like to express my heartfelt gratitude to my parents for their unconditional love and encouragement, and my husband, Tao Wu, for his constant supports all through the project.

Contents

List of Figures

List of Tables

Chapter 1

Introduction

During the past 50 years, the silicon based integrated circuit (IC) has achieved unparalleled success. It literally brought the industry revolution into the information age and completely changed our world. At the very beginning, there were only a few semiconductor and passive components on a common substrate. Driven by the demand for higher speed and performance at lower cost, the technology improvements have followed the well known "Moore's Law" which is based on the fact that transistor gate time-delay decreases with device size, with the number of transistors on a chip roughly doubling every two years. Today, one square cm of Si can accommodate over 500 million transistors. According to the 2001 edition of the International Technology Roadmap for Semiconductors (ITRS), over one billion transistors per square cm can be expected and the transistor dimensions will shrink down to 22 nm by 2016 [1, 2]. Although theoretical studies have suggested that the conventional Si transistors of nanoscale can function properly and no fundamental fabrication limitations have been known so far, the rapid growth of Si microelectronics will still meet the great difficulties imposed by the

problems that come along with the increasing complexity. "Moore's Law" combining with internet explosion finally results in a situation where the computer performance is determined by the rate of transmitting and receiving data rather than processor speed. To connect the nano-size components to each other and to the outside, kilometers of metallic wires have to be placed on a very small chip which results in extremely low cross sections of metallic wires and very small spacing between them. The wire cross section shrinking will lead to decreasing interconnect speed and increasing parasitic resistive-capacitive coupling delay. Other consequences such as cross talk, power dissipation and low tolerance of noise will also become important [1, 3, 4].

More recently, optical communication technology has dominated long-haul systems by replacing copper wires with optical fibres to meet the bandwidth and distance requirements, and it is migrating to metropolitan area networks (MANs) and local area networks (LANs). Furthermore, by using dielectric optical waveguides instead of metallic wires the emerging technology of "microphotonics" is able to solve most of the problems related to the bandwidth limitation and "interconnect bottleneck" of microelectronic ICs. However, the integration of photonic components with current Si microelectronic technology is not easy. Most of photonic devices are not made from Si, and there is still no single dominant material. III-V semiconductors such as indium phosphide (InP), gallium arsenide (GaAs) or electro-optic crystals such as lithium niobate ($LiNbO_3$) are

widely employed, which are not compatible with Si VLSI technology. As a result, optical devices are comparatively large and bulky with low production yield. All these lead to high cost, complexity and low reliability in integration [5, 6].

To overcome these obstacles Si photonics has been proposed to develop photonic devices based on Si materials, e.g. silicon, silicon oxide, nitride and oxynitride which are compatible with standard Si processing technology. Through utilizing Si materials, the cost of fabrication of integrated optics can drop significantly by taking advantage of well-developed Si VLSI technology, the component size can decrease to nanoscale, packing density can reach the gigascale, and control and driving electronics from microelectronics can be employed directly. In addition, Si substrates are the largest substrates so far which opens the possibility to realize large-scale integration and mass production [5, 6, 7, 8]

To "siliconize" photonics, several building blocks haven been studied intensively, including generating light, selectively guiding and amplifying light, encoding light and detecting light [9]. To achieve Si based light sources has always been the most challenging task, with the first optically pumped silicon Raman laser being reported only very recently [10, 11]. It is well known that bulk Si is a poor light emitter due to its indirect band gap and the presence of nonradiative recombination pathways. In Si, the electron-hole radiative recombination lifetime is as long as several milliseconds, while the

defect related nonradiative recombination lifetime is only on the order of nanoseconds. It appears that in Si nonradiative recombination is much more efficient than radiative recombination in Si [12].

Many approaches and extensive studies have been attempted to overcome these obstacles and achieve efficient emission from Si. One promising solution is to introduce impurities such as rare earth (RE) elements into materials. Of the RE elements, Er has attracted the most extensive attention because of the coincidence between its 4f-4f transition at 1535 nm and the transparency window used for telecommunications. However, the demand to realize full color light emission from silicon structures extends technology interests to many other RE elements such as Ce, Eu and Tb which can emit ultraviolet (UV) /blue and green light, respectively [13, 14].

Luminescence from RE ions has been studied extensively since the beginning of the 20th century [15]. Currently various RE-doped materials are playing important roles in many areas such as display, solid state lasers, detectors and data storage [16, 17, 18, 19, 20]. For example, their visible luminescence has been deployed in the cathode ray tube (CRT) phosphors to generate red, green and blue light for many years [13]. The enormous demands for developing optical sources and amplifiers compatible with Si VLSI technology attract increasing interest for one type material: RE-doped Si materials.

This thesis investigated silicon oxide (oxygen-rich or silicon-rich) thin films doped

with various RE elements including Ce, Eu, Tb and Er, deposited by electron cyclotron resonance plasma-enhanced chemical vapour deposition (ECR-PECVD). The successful *in-situ* incorporation of high concentrations of RE elements has been achieved. The photoluminescence (PL) properties of the films with different compositions under various annealing conditions have been studied and RE-related PL intensities have been optimized. The correlation between PL properties of the films and their structure evolution during annealing was elucidated through the Fourier transform infrared (FTIR) spectroscopy and high resolution transmission microscopy (HR-TEM). The possible luminescence centers have been identified and the interpretation of their excitation pathways has been attempted. The coupling of these luminescence centers and the thermal structural evolutions reflected by the changes of their PL signatures have been studied.

The general background for RE luminescence and state of the art for RE-doped silicon oxides is reviewed in Chapter 2. A detailed description of the ECR-PECVD system is presented in Chapter 3. Chapter 4 presents the fundamentals of Rutherford backscattering spectrometry (RBS). Chapter 5 gives the experimental details employed in this study including experimental set up, deposition parameters and annealing conditions. Chapter 6 summarizes the composition, thickness and refractive index of the films studied in the present work. The correlation between deposition parameters and film compositions is reviewed. Chapters 7 to 10 discuss the influence of film composition and

annealing conditions on the PL properties of the films containing various RE doping. Finally, Chapter 11 presents the conclusions of this study and suggestions for future work.

Chapter 2

Luminescence from RE-Doped Silicon Oxides

2.1 Luminescence from RE Ions

Ce, Eu, Tb and Er are all in the sixth row of the Periodic Table and have an electronic configuration [Xe] $4f^{n+1}.6s^2$ with n=1, 6, 8 and 11, respectively. Optically active RE ions often exist as trivalent formed by losing one 4f electron and both two 6s electrons and have an electronic configuration [Xe] $4f^n$ [13].

Conventionally the energy states of RE ions are labeled as $^{2S+1}L_J$ according to the angular momentum properties of the ions. The multiplet can be described by L and S, which denote orbital angular momentum quantum number and spin quantum number, respectively. The Stark levels of each multiplet can be described by J, the total angular momentum quantum number, which is determined by the Russell-Sauders spin-orbit coupling scheme. The total spin of the ion is given by 2S+1.

Luminescence from RE ions is mainly attributed to their 4f-4f or 5d-4f transitions. The 4f-4f transitions are usually parity forbidden for free ions. Since all the energy levels have the same parity (parity of a single configuration wave function is even or odd

depending on whether the sum of the single electron orbital angular momentum quantum numbers is even or odd), the electric dipole matrix element between two energy levels of the same parity is zero, and electric dipole transitions between any two levels of the particular ion are forbidden. RE ions incorporated into crystal fields are subject to electric fields, and each energy level is split into Stark levels. The existence of the Stark levels breaks the inversion symmetry of the RE ion's environment, therefore the electric dipole transitions between Stark levels of different multiplets are partially allowed. The corresponding emission is usually a sharp band with long lifetime of the order of milliseconds and small oscillator strength around 10^{-6}. Because the incomplete 4f shells are shielded from the external environment by outer 5s and 5p orbits, the 4f-4f transitions are relatively insensitive to the surrounding field. Since the inter-Stark levels transitions happen ultra-fast, the population in any multiplet can be considered in a local thermal equilibrium approximation. The consequent Boltzmann distribution within the multiplet makes it possible to consider each multiplet as a "broadened" single energy band.

In contrast, 5d-4f transitions are parity permitted, they have relatively shorter luminescence lifetimes and much stronger oscillator strengths. Additionally, 5d-4f transitions are very sensitive to the surrounding ligands because 5d states are directly exposed to the local environment. Thus, changes in the spectral shapes, peak positions and intensities may suggest the evolution of the matrix structure [13, 21, 22].

2.2 Limiting Factors

There are two major obstacles that have to be overcome to achieve efficient emission from RE-doped silicon oxides: inefficient excitation of the 4f-4f transition for RE ions and low solubility of optically active RE ions in most Si based host materials.

Generally there are two ways to optically excite emission from RE ions in insulators such as silicon oxides: direct and indirect excitation. In the first way, pump photons with the appropriate energy are resonantly absorbed by the RE ion, interact with its absorption band and bring it to the excited state. Direct excitation is not very efficient for many RE ions thanks to the low 4f-4f transition probability and consequent low absorption and emission coefficient. In addition, there are strict constraints on excitation wavelength [13, 15]. For example, Er ions in silica can be only directly excited at a few wavelengths including 488, 514, 800, 980 and 1480 nm and the absorption cross section is as low as 10^{-21} to10^{-20} cm^2 [23]. In contrast, the indirect excitation mechanism introduces broadband sensitizers into the material which may transfer energy to the RE ions by dipole-dipole Förster-Dexter coupling. As a result, RE emission can be enhanced significantly [23, 24].

The solubility of optically active RE ions in various Si materials is universally low thanks to the mismatch of ionic radius between RE ion and matrix and the rigid covalent bonding of the matrix network. Above the critical concentrations, RE ions often tend to precipitate which results in severe luminescence quenching through ion-ion interaction or

formation of optically inactive phases. It is very difficult to incorporate high concentrations of optically active RE ions in Si materials through equilibrium techniques such as sol-gel method [25]. Low temperature techniques such as ion implantation or PECVD are able to increase the solubility limit by up to one order of magnitude, which is attributed to less diffusion of doped ions. Particularly, ECR-PECVD can generate a uniform distribution of RE-doping through the entire thickness of the film and create less defects due to the low impinging ion energy [26, 27 , 28, 29, 30, 31, 32].

2.3 Er-doped Silicon Oxides

Er usually exists as a trivalent ion in Si materials. Figure 2.1 shows the energy level diagram of Er ions in glass. Its characteristic emission around 1535 nm corresponds to the transition from its first excited state $^4 I_{13/2}$ to the ground state $^4I_{15/2}$. The common absorption bands are around 800, 980 and 1480 nm, which are related to the transitions from ground state $^4I_{15/2}$ to the higher $^4I_{9/2}$, $^4I_{11/2}$ and $^4I_{13/2}$ states, respectively [33, 34]. As aforementioned, these 4f-4f transitions are relatively independent of host material.

Er-doped materials have received the greatest attention due to the coincidence between the Er emission band around 1535 nm and the third low loss window of silica optical fibers. Er-doped fiber amplifiers (EDFA) have been a very mature technology and widely used in telecommunications, while the technical shift to Er-doped waveguide

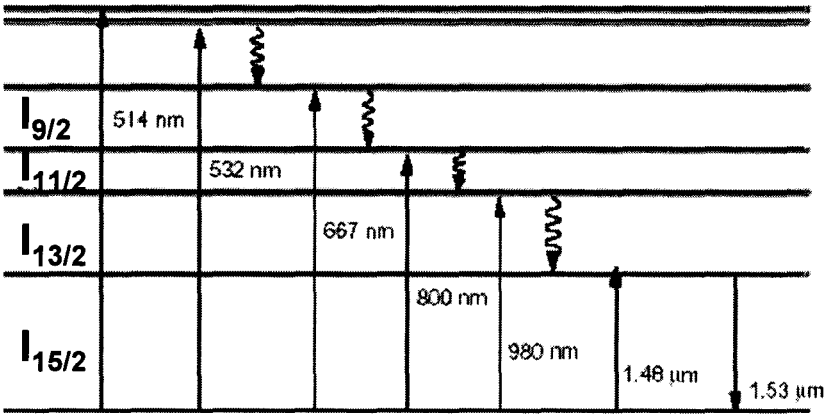

Figure 2.1 Electronic energy level diagram of Er^{3+} doped in silicon oxide (adapted from [33]).

amplifiers (EDWA) or Er-based light emitters in integrated optical circuits is problematic. The maximum gain per unit length of amplifier is determined by the product of the stimulated emission cross section σ_e and the optically active Er concentration. Typical σ_e values are as low as 10^{-21}~10^{-20}cm^2. At the same time, Er ions have very low solubility that ranges from 10^{18} to 10^{19} cm^{-3} in amorphous SiO_2, since they need to be bond to non-bridging oxygen (NBO) atoms, while the available NBOs are quite limited [35, 36]. Unlike the EDFA, which can extend several to tens of meters to compensate the limited Er doping to achieve decent gain, waveguide amplifiers and light sources for integrated photonic circuits usually have much smaller size. Simply increasing Er doping or pump power can not solve the problem due to the concurrence of severe side effects such as cooperative upconversion and excited state absorption (ESA) at high Er

concentrations and high pump power [13, 23]. Network modifiers such as phosphors were added in the glass matrix to change the composition continuously, increase the fraction of NBOs, and consequently enhance Er solubility [37]. Another solution is utilizing sensitization mechanism to increase the excitation efficiency. A number of sensitizers have been exploited including Ytterbium (Yb) ion, silver ion, Si-nanoclusters (Si-ncs) and some organic complexes [38, 39, 40, 41].

One structure that has been receiving particular attention is Er-doped silicon-rich silicon oxide (SRSO) containing Si-ncs, which can enhance Er emission significantly through exciton-mediated energy transfer processes. Si-ncs can be considered as a three-dimensionally confined structure and its band gap increases with the decrease of the size due to quantum confinement effects. SRSO itself has been considered a promising candidate for Si-based light emitter., The emission is in the near IR even when Si-ncs sizes reduce to the magnitude of nanometers, and the emission band is very broad due to the wide distribution of silicon cluster sizes [42, 43, 44, 45].

An Er excitation and energy transfer model has been well established for Er-doped SRSO and is depicted in Figure 2.2 [45]. After a Si-nc absorbs a photon, an exciton bound in the Si-nc is generated. The exciton may recombine nonradiatively by transferring energy to an Er ion nearby and excite it to the excited state. Then the Er ion decays to the ground state by emitting a photon of 1535 nm wavelength. It was found that the emission

from all the Si-ncs coupled to the Er ions can be quenched completely by transferring energy to them [46].

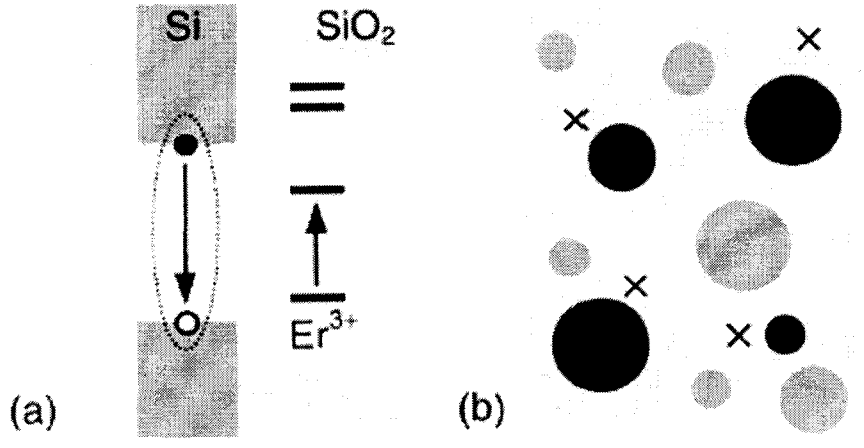

Figure 2.2 Er^{3+} excitation and energy transfer model; (a) a schematic band diagram of SiO_2 containing a Si-nc and Er; (b) a schematic representation of SiO_2 containing Er (crosses) and Si-ncs (circles) (adapted from [45]).

The Si-ncs sensitized excitation mechanism offers many unique advantages. First, since it is Si-ncs that absorb pump photons, the excitation cross section of Er ions can be increased by over 10^3 times, which makes greater emission intensities at lower Er concentrations possible. Second, since the absorption band of Si-ncs covers the entire visible spectrum, the utilization of broad band excitation sources becomes possible. The successful excitation of Er emission in SRSO using broad band visible excitation sources such as commercial camera flashguns or blue LEDs have been demonstrated [47, 48]. In

addition, by choosing appropriate pump wavelengths, the ESA effect could be avoided.

2.4 Ce-doped Silicon Oxides

Ce ions may occur as either trivalent or tetravalent in silicon oxides by losing two 6s electrons and one or both of its 4f electrons. Ce^{4+} is optically inactive since it has no usable 4f electron, while Ce^{3+} still has one 4f electron and its luminescence is attributed to 5d-4f transitions. The energy level diagram of Ce^{3+} is shown in Figure 2.3. Since the transition is parity allowed, its oscillator strength is much higher than that of 4f-4f transitions and ranges from 0.01-0.1. As a result, luminescence from Ce^{3+} is much more intense than that of other RE elements. Because the 4f electron is shielded by 5s and 5p electron shells from the external environment, the overall splitting of ^2F_J states is small. When the 4f electron is excited to the outer 5d state, it is exposed to the surrounding ligands directly. The degeneracy of the 5d state is partially or completely removed, and the overall splitting is large. Consequently, Ce^{3+} usually has a broad absorption band in the UV range and a broad emission band in the UV to blue range. The lineshape and intensity for Ce^{3+} luminescence are very sensitive to film composition, deposition process and post-deposition treatments [49, 50, 51].

Reisfeld et al. [52] pointed out that the wavenumber (ν) of the 4f -5d transition of Ce^{3+} is related to the differences between optical electronegativity (χ_{opt}) of the surrounding ligands and that of Ce^{3+} by equation:

$$\nu = (\chi_{opt}(\text{ligand}) - \chi_{opt}(\text{Ce})) \times 3000 \quad (2.1)$$

which indicates that the absorption and emission bands of Ce^{3+} may red shift with increasing electronegativity (χ_{opt}) of the surrounding ligands. This phenomenon is called nephelauxetic shift.

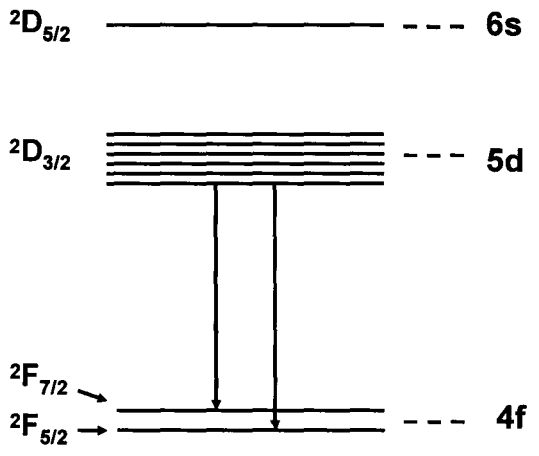

Figure 2.3 Electronic energy level diagram of Ce^{3+} in silicon oxide (adapted from [49]).

Generally there are two ways to achieve Ce-doped silicon oxides. One way is direct synthesis of Ce-doped silicon oxide or silicate by a sol-gel method, implantation or CVD [52, 53, 54, 55, 56]. The other way is by depositing epitaxial CeO_2 on a Si substrate. Ce silicate at the interface can be achieved through a diffusion process during the subsequent high temperature treatment. Pulsed laser ablation and radio frequency (RF) sputtering techniques have been employed to deposit CeO_2 [57, 58, 59, 60, 61, 62].

Sol-gel method has been employed most widely because of its low cost and particular

convenience for high yield and large area production. Ion implantation or regular CVD methods are also reported. There is very limited information about *in-situ* incorporation of Ce ions by PECVD technique.

Reisfeld et al. [52, 53] reported Ce-doped silica containing 0.02-0.1 equivalent mol% CeO_2 prepared by sol-gel method at 1000 °C using ammonium ceric nitrate as Ce source. The absorption spectra peaking at 250 and 300 nm were observed for samples prepared in O_2 and N_2 atmosphere, respectively. This difference is due to the fact that Ce^{4+} is dominant in the former sample while Ce^{3+} is dominant in the latter. Emission bands between 400 and 450 nm under 337 nm excitation were observed from the sample prepared in N_2. It appeared that the emission arises from Ce^{3+} instead of the oxide defects in the silica matrix, since the peak of latter is broader and the decay time is shorter. Severe concentration quenching effects were observed for the samples with Ce concentrations higher than 0.5%.

Xu et al. [54, 55] reported that Ce-doped silica synthesized by sol–gel method using $Ce(NO_3)_3$ solution as Ce source. For 0.1% Ce-doped samples heat treated in air at 1000 °C, after additional annealing in H_2 at 850 °C, the main absorption band shifts from 265 to 320 nm. A broad emission band peaking at 445 nm excited at 330 nm was observed. The emission intensity increases significantly with increasing annealing temperature until it reaches a maximum at 850 °C. This was attributed to the transitions from Ce^{4+} to Ce^{3+}

during the annealing process. It was also found that the decoration of S^{2-} and Cl^- anions cannot only increase the luminescent intensity significantly but also blue-shift the luminescent wavelength to 430 and 400 nm, respectively. This was attributed to the nephelauxetic shift with change of covalency degree of Ce^{3+} bonds.

As the most widely employed synthesis technique, sol-gel method suffers from several drawbacks such as porous final products, quenching of Ce^{3+} emission through coupling with -OH and low solubility of Ce ions. Extensive work has been conducted to overcome these limitations, control the emission wavelength and enhance the emission intensity [37, 63, 64, 65].

It is well known that densification processes during the annealing can reduce the porosity efficiently. Comparing with oxidation ambient, annealing in inert or reducing anneal ambient usually results in much higher emission intensity with a red shift of the absorption and emission bands. This phenomenon was explained by the reduction of Ce^{4+} ions in inert or reducing ambients, which is optically inactive and has a strong charge transfer band. An enhancement of the emission intensity and blue shift of the emission band with increasing annealing temperature was also observed. It was suggested that the progressive removal of –OH groups during annealing not only can reduce nonradiative combination channels, but also give rise to the formation of NBOs and contribute to the coordination of Ce^{3+} within the silica net work [54, 55, 56] .

Severe concentration quenching effects were observed universally at Ce concentrations higher than 0.1 mol% and a related aggregation process was proposed. During the heat treatment Ce^{3+} ions remain in the liquid phase, filling the pores of the wet gel at the beginning. After the water is removed, Ce^{3+} ions aggregate within the pores. It is evident that both the precursors and preparation process affect the dispersion of Ce ions strongly. It was proposed that a high purity stoichiometric matrix is desired with the aim to minimize intrinsic defects. An enhancement of the emission from Ce ions by adding Al was demonstrated. Al can help to disperse Ce^{3+} ions by acting as a network former to attract those Ce^{3+} ions to their location as a result of charge compensation, or a network modifier to increase the solubility of Ce^{3+} ions directly through increasing NBOs [64, 65].

A number of groups observed similar UV/blue light emission from CeO_x/SiO_x or Ce/Si films subjected to thermal treatment in inert or reducing ambients at high temperatures. The origin of the emission still remains a controversy. Morshed et al. [57] achieved an emission band peaking at 400 nm from CeO_2/Si films after rapid thermal annealing in Ar at 1000 °C. The emission was attributed to Ce_6O_{11} formed near the CeO_2/Si interface. Choi et al. [59, 60] achieved weak 388 nm emission from CeO_x/Si films and intensive 358 nm emission from (CeO_x+Si)/Si and (CeO_x+Si)/SiO_x/Si films under annealing in N_2 at 1100 °C. The significant diffusion of Si from the substrate into CeO_2 and the formation of two cerium silicate phases, $Ce_2Si_2O_7$ and $Ce_{4.667}(SiO_4)_3O$ at

the interface were observed. The 358 nm emission was attributed to the $Ce_2Si_2O_7$ phase, and the weak 388 nm emission to the $Ce_{4.667}(SiO_4)_3O$ phase. Kepinski et al. [61, 62] obtained similar emission peaking at 400 nm from the CeO_2/SiO_2 system subjected to annealing in H_2 at 1050 and 1100 °C. The emission was assigned to the observed unidentified cerium silicate with some structure similarity to tetragonal $Ce_2Si_2O_7$ silicate.

2.5 Eu-doped Silicon Oxides

Eu ions can exist as either trivalent or bivalent, and both of them are optically active. Their energy level diagrams are given in Figure 2.4. The Eu^{2+} luminescence is related to the $4f^65d^1$-$4f^7$ transition. The 5-fold degeneracy of the $4f^65d^1$ state which is due to the surrounding crystalline field gives rise to two broad bands in the range 400-600 nm [66]. For example, the environment in tetrahedral and octahedral symmetry would cause a splitting of 5700 and 12849 cm^{-1}, respectively [67]. The lifetime of the transition is on the order of several hundred ns. A series of Eu^{3+} characteristic narrow emission bands from 570 to 700 nm corresponds to the 4f-4f transitions from $^5D_0$ to ^7F_j (j = 0 to 6) states. The Eu^{3+} luminescence lifetime values are usually from 1.5 to 2.0 ms [68].

As noted previously, 5d-4f transitions have relatively higher oscillator strength since they are parity allowed. Therefore, Eu^{2+} ions are highly desired in practice because of their intense luminescence with intensity 10^6 times higher than that of Eu^{3+}. Eu^{2+} ions can be achieved through using reducing atmosphere [69, 70] or reductive lattice such as

silicate, silicon-nitride and silicon-sulfide [71]. Eu ions have been introduced into silicon oxide in several ways including sol-gel method, ion implantation and RF sputtering [69, 70, 71, 72, 73], while sol-gel method again is most widely adopted because of its low cost and easy mass production. It should be noted that due to the nature of 4f-5d transition, the excitation and emission of Eu^{2+} are also very sensitive to film composition, deposition process and post-deposition treatments.

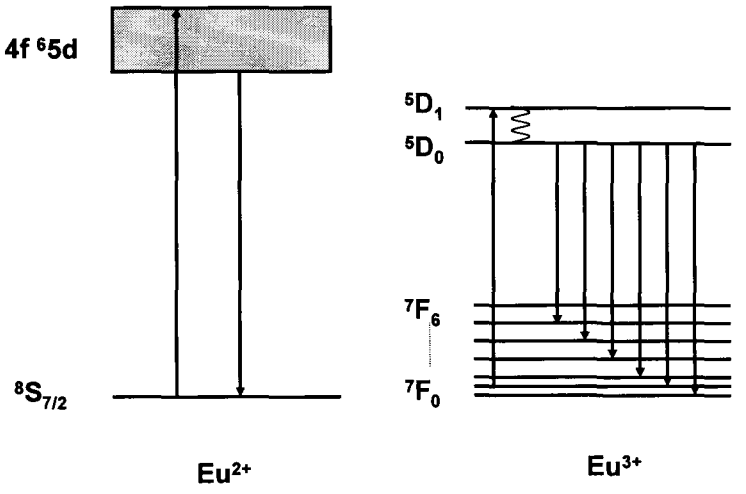

Figure 2.4 Electronic energy level diagram of Eu^{2+} and Eu^{3+} in silicon oxide (adapted from [66, 68]).

Although Eu^{2+} complexes in solution or gel can be easily oxidized to Eu^{3+} in air, the successful incorporation of Eu^{2+} in silica through sol-gel method has been realized by several groups. Garcia et al. [69] prepared Eu-doped silica by dissolving $EuCl_2$ in silica gel directly or adding $EuCl_3$ followed by reducing the solidified gel in hydrogen

atmosphere at 500 °C. In photoluminescence excitation (PLE) measurements, for 480 nm emission the reduced sample exhibited a more intense excitation band at 360 nm which was attributed to $4f^7$-$4f^65d^1$ transition of Eu^{2+}. This excitation band was decomposed into two Gaussian components peaking at 307 and 367 nm, respectively. Their separation (5293 cm^{-1}) revealed the splitting of $4f^65d^1$ state caused by the weak crystalline field of tetrahedral symmetry. Under 355 nm excitation, the reduced sample also exhibited a stronger emission peaking at 489 nm which was assigned to the $4f^65d^1$-$4f^7$ transition of Eu^{2+}. From excitation and emission spectra, it was concluded that the reduced gel showed a greater concentration of Eu^{2+}. Similarly, Nogami et al. [70] reported that Eu^{2+} incorporation in SiO_2 co-doped with Al_2O_3 was achieved by reducing Eu^{3+} in 20% H_2 – 80% N_2 at 800 °C for 2 hours. The excitation spectrum for 444 nm emission exhibited a band peaking at 390 nm, and a broad emission band peaking at 450 nm was observed for 390 nm excitation. They were both assigned to the Eu^{2+} related transitions. However, Eu^{2+} emission decreased significantly when the sample was reheated in air which implied the conversion from Eu^{2+} to Eu^{3+}. To protect Eu^{2+} from oxidation in air, Tsuboi et al. [73] prepared Eu^{2+}-complex-doped SiO_2 gel at room temperature, in which Eu^{2+} was encapsulated in 1,4,7,10,13–pentaoxa-cyclopentadecane (crown ether 15-crown-5) or its derivative. The absorption band peaking at 250 nm and the emission band around 420 to 430 nm under 330 nm excitation were assigned to Eu^{2+} related transitions. After drying,

50-70% of Eu ions were found to have remained as Eu^{2+}. Therefore it was suggested that Eu^{2+} complexes inside gels can be protected through encapsulation effect of 15-crown-5 and were stable against oxidation in air.

Liu et al. [72] investigated the PL and PL excitation spectra for thermally grown SiO_2 implanted with Eu ions. The annealing was performed in N_2 at temperatures from 1000 to 1200 °C for 30 minutes. The excitation wavelengths are 377 and 464 nm. For 464 nm excitation, a broad band emission peaking at 604 nm was observed from as-implanted samples. This band was decomposed into three Gaussian components centered at 585, 604 and 620 nm which were assigned to the $^5D_0$-^7F_j (j=0 to 4) transitions of Eu^{3+}. The intensity of the band increases with annealing temperature and reaches a maximum at 1100 °C, then decreases at 1200 °C. For excitation at 377 nm, PL band peaking at 440 and 510 nm were observed from the as-implanted samples. This band was attributed to $4f^6\,5d^1$ to $4f^7$ transitions from Eu^{2+}. A monotonic increase of the band intensity with increasing annealing temperature was observed. Thus it was considered that the conversion from Eu^{3+} to Eu^{2+} can be achieved by annealing in N_2 at 1200 °C.

Eu^{2+} can exist in the form of europium silicate such as Eu_2SiO_4 and $EuSiO_3$ and produce very strong and stable luminescence, while the preparation of pure europium silicates has been found to be very difficult due to their high formation temperature. The formation of pure Eu_2SiO_4 and $EuSiO_3$ requires temperatures of 1800 and 1400 °C,

respectively [74, 75]. However, according to the phase diagram for the EuO-SiO_2 system, the formation of multiphase europium silicate only requires temperatures from 900 to 1000 °C [76]. Qi et al. [71] reported the fabrication of europium silicate at this temperature. The films were deposited by RF magnetron sputtering using Si disk and $EuSi_2$ powder targets. Film A was prepared using pure Ar as sputtering atmosphere and annealed in air at 1000 °C for 30 minutes, while film B was prepared using mixed Ar/O_2 gas as sputtering atmosphere and annealed in air at 900 °C for 15 minutes. XRD analysis confirmed the presence of Eu_2SiO_4, $EuSiO_3$, Eu_2O_3, SiO_2 and Si in film A, and Eu_2SiO_4, SiO_2 and Si in film B. X-ray photoelectron spectroscopy (XPS) analysis revealed the sensitivity of film composition on both sputtering and annealing conditions. It was suggested that the density of europium silicate can be increased by increasing both the concentration of $EuSi_2$ in the sputtering target and the annealing temperature.

2.6 Tb-doped Silicon Oxides

Tb ions usually exist as trivalent in silicon materials. Figure 2.5 shows the energy level diagram of Tb^{3+}. A series of characteristic sharp emission lines of Tb^{3+} from 400 to 600 nm are related to the transitions from $^5D_4$ to ^7F_j states, respectively. Emission lines corresponding to the transition from $^5D_4$ to $^7F_5$ centered at around 543 nm is the strongest in most host materials because of the high probability of the electric-dipole and magnetic-dipole transition. Tb^{3+} emission has a broad excitation band from 220 to 300 nm

which corresponds to 4f-5d transition from $4f^8$ to 4 $f^7 5d^1$ states. It can also be excited at 351 and 488 nm which correspond to 4f-4f transition from $^7F_6$ to $^5L_9$-$^5G_5$ (multiplets) and $^5D_4$ states, respectively [14, 77, 78].

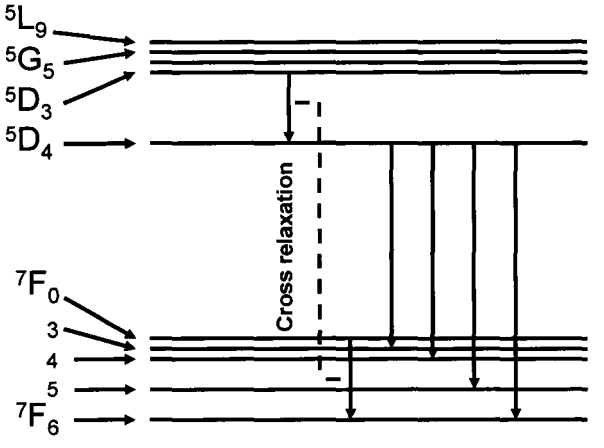

Figure 2.5 Electronic energy level diagram of Tb^{3+} doped in silicon oxide (adapted from [77]).

The energy difference between $^5D_3$ and $^5D_4$ states and the energy difference between $^5D_4$ and $^5F_6$ states are approximately the same. When Tb ions are located closely, the energy transfer between them becomes possible. An excited Tb ion at the $^5D_3$ state may relax to the $^5D_4$ state by transferring energy nonradiatively to a neighbouring Tb ion at the ground state. This leads to two simultaneous consequences: the reduction of the emission from the $^5D_3$ state and the enhancement of the emission from the $^5D_4$ state. This effect is called cross-relaxation and usually observed when the Tb concentration is high or Tb ions

form clusters [79].

Tb-doped SiO_2 is commonly prepared through ion implantation and PECVD methods [79, 80, 81, 82, 83, 84]. Although the luminescence of Tb^{3+} originates from intra 4f transitions and its luminescence wavelength only varies slightly with the host materials and the preparation condition, its luminescence intensity can be highly dependent on them.

The local structures around Tb ions in SiO_2 were investigated by Ofuchi et al. [80] through fluorescence X-ray absorption fines structure (XAFS) analysis at the Tb L_{III} edge. Tb ions were introduced into thermally grown SiO_2 through ion implantation, and the annealing was performed in vacuum at 900 ° C for 30 minutes. According to X-ray absorption near-edge structure (XANES) spectra, as-deposited and annealed Tb:SiO_2 exhibit the same peak position as that of Tb_2O_3, thus Tb ions in the films are considered as trivalent. The Tb ions in the as-deposited sample are mainly coordinated with two oxygens (Tb-2O) and the Tb-2O bond length is 2.09 Á. There are two types of Tb-O bonds coexisting in the annealed sample whose bond lengths are 2.10 and 2.27 Á, which correspond to Tb-2O and Tb-6O structures, respectively. At the same time, an enhancement of the Tb-related PL intensity (excitation at 488 nm) was observed after annealing. Therefore it was proposed that the formation of Tb-6O structures was responsible for this enhancement.

The effects of Tb concentration and annealing dependence on the PL spectrum for Tb ions implanted in SiO_2 were studied by Amekura et al. [79, 81]. Three sequential implantation steps were performed to achieve a uniform and flat Tb distribution, and Tb concentrations varied from 0.18 to 2.7 at.%. Annealing was performed in vacuum or mixed gas of 8% H_2 + 92% N_2 at temperatures from 500 to 1050 °C. The excitation source for PL measurements was 351 nm. It was found that Tb^{3+} PL increases stronger than linear for concentrations of up to 1 at.% and reaches saturation at greater concentrations. The superlinear increase of the PL intensity was attributed to cross-relaxation effects. Unlike Er:SiO_2 or Eu:SiO_2 whose lifetime decreases significantly with increasing concentration, the PL lifetime of Tb:SiO_2 was confirmed to remain almost constant at concentrations as high as 2.7 at.%. Therefore the PL saturation at high Tb concentrations was assigned to the exhaustion of optically active sites of Tb^{3+}. It was found that the Tb^{3+} PL increases with annealing temperature until 900 °C. This was explained by the annihilation of radiation damage and increase of optically activated Tb ions. The decrease of Tb^{3+} PL at higher temperatures was attributed to the clustering of Tb ions via thermal diffusion.

The PL properties of Tb:SiO_2 prepared by PECVD using *tris--(2,2,6,6-tetramethyl-3,5-heptanedionato) Tb (III)* as Tb source were studied by Yoshihara et al. [82]. Tb concentration varied from 0.2 to 7.6 at.%. Annealing was performed in N_2

for 0.5 hours at 500 to 900 °C. The excitation wavelength for PL measurements was 248 nm. The Tb^{3+} PL intensity increased linearly with annealing temperature. Since the PL from the $^5D_3$ state began to appear at 800 and 900 °C, the observation of the PL increase was attributed to the redistribution of Tb ions during annealing and the consequent enlargement of their mutual separation.

As noted previously, Er ions embedded in SRSO can be excited indirectly through a Förster-Dexter energy transfer process at wavelengths away from the Er absorption bands. In principle, similar excitation mechanisms can operate in SRSO with other RE doping as long as the band gap of Si-ncs wide enough. The indirect excitation of SRSO doped with a range of RE ions including Pr, Tm, Eu and Tb has been demonstrated [85, 86, 87].

The Si-ncs PL peaks are usually in near IR range, while the characteristic peaks of Tb^{3+} PL are in the range of 400 to 600 nm. Therefore, the extension of the indirect excitation mechanism to Tb-doped SRSO may give rise to a question: how can the exciton bound in Si-nc excite Tb ions when it has a longer emission wavelength? It has been widely accepted that as a result of quantum confinement, the band gap of Si-nc increases with decreasing size when it is smaller than 5 nm and push the PL to the visible region. In practice, however, its PL peak does not go beyond to 2.1 eV (590nm) even when the crystalline size decreases to 2-3 nm [88, 89]. Wolkin et al. [42] proposed an explanation for this apparent contradiction through the study on PL of silicon quantum

dots in porous silicon. It was found that when the sample was kept in Ar ambient, the PL peak can be tuned from near IR to UV. However, when the sample was exposed to air, a red shift of the PL peak by as much as 1 eV was observed. It was suggested that the electronic states of silicon quantum dots was determined by both quantum confinement and surface passivation. When exposed to oxygen, the formation of Si=O bonds produces oxygen-related localized states in the bandgap and results in the red shift of the PL peak. Therefore, the actual band gap of a Si-nc embedded in silicon oxide could be much larger than that indicated by its emission wavelength. The actual band gap of a 2-3 nm Si-nc could be as high as 2.5 eV according to quantum confinement theory, which is sufficient to excite Tb^{3+}.

So far, the only demonstration of the indirect excitation of Tb-doped SRSO was reported by Seo et al. [83]. Tb-doped SRSO with C co-doping was deposited by ECR-PECVD with concurrent sputtering of Tb. The concentration of Si and C were in the range of 34-41 at.% and 0-10.4 at.%, respectively, and the Tb concentration was fixed at 0.1 at.%. The films were annealed in Ar at 950 ^{o}C for 5 minutes to precipitate Si-ncs and mixed 10% H_2 + 90% N_2 ambient at 700 ^{o}C in sequence. Tb emission was excited at 325 nm which is not resonant with any Tb^{3+} absorption band. No Tb^{3+} PL was observed from carbon-free samples at Si contents lower than 34 at.%. Tb^{3+} PL exhibited a strong dependence on Si content, and the maximum PL corresponded to a Si content of 35 at.%.

It was found that the Tb^{3+} PL increases with increasing C content and the maximum PL was observed at a C content of 4.5 at.%. The observation of Tb^{3+} PL was assigned to exciton-mediated energy transfer between Si-ncs and Tb ions. The composition dependence of the Tb^{3+} PL was explained through the formation of small Si-ncs at low excess Si content which have a wide enough band gap. The co-doping of C was suggested to enhance Tb^{3+} PL through increasing the formation of very small Si-ncs by acting as nucleation sites and the effective coupling between high energy excitions and Tb ions.

Chapter 3

ECR-PECVD System

RE (Ce, Eu, Tb and Er) doped silicon oxide films discussed in the thesis were deposited by McMaster's ECR-PECVD system. CVD is a class of techniques widely used to deposit dielectric films, during which the precursor gases are cracked producing chemically active species to react with each other and form desired reaction products for the deposition on a given substrate. PECVD employs high energy electrons in plasma cracking the precursor molecules at low temperature. ECR refers to a specific way to generate plasma, during which the electrons are continuously accelerated by resonantly absorbing energy from circularly polarized electromagnetic field.

ECR-PECVD has two advantages over conventional PECVD methods. First, The ECR technique can generate highly ionized plasmas, which are more efficient in cracking precursor molecules. As a result, films with less contamination can be achieved. Second, the ECR technique allows the separation of the main plasma region and the substrate, and only the ions with moderate energies are extracted for the deposition. This can reduce the damage of the films caused by the bombardment of high energy particles. This chapter

presents ECR plasma generation theory followed by a detailed description of the McMaster ECR-PECVD system.

3.1 ECR Plasma Generation Theory

When an electron moves in a magnetic field, it is subjected to a Lorentz force, $\vec{F}$, which can be expressed as:

$$\vec{F} = e\vec{v} \times \vec{B} \tag{3.1}$$

where e is the charge of the electron, $\vec{v}$ is the particle velocity, and $\vec{B}$ is the magnetic field strength. The force causes a circular motion of the electron. The frequency ω_c (cyclotron frequency) and radius r_l (Larmour radius) of the circular motion can be determined by balancing the magnetic and centripetal forces:

$$\omega_c = eB / m_e \tag{3.2}$$

and

$$r_l = \frac{v_\perp}{\omega_c} \tag{3.3}$$

where m_e is the mass of the electron, and $v_\perp$ is the velocity component perpendicular to B.

The traveling path of the electron is helical when its velocity is not completely vertical to B, since its velocity component parallel to B is unaffected. This is desired for the plasma generation since the increase of the effective traveling path of the electron can

increases the collision probability between the electrons and the plasma gas molecules. When an additional circularly polarized electric field along the B direction with proper phase is applied at the cyclotron frequency, the electron will resonantly absorb energy from the electric field and both $v_{\perp}$ and r_l increase accordingly.

The ECR plasma zone is defined by the magnetic field generated by the two electromagnets as depicted in Figure 3.1 [90]. At first, there exist only a few free electrons. They continuously gain energy from the electric field (the microwaves) through a resonant absorption process. Eventually they obtain enough energy to excite, ionize and dissociate the plasma gas molecules during the inelastic collisions with them. More secondary electrons are generated and undergo similar processes to create an avalanche effect. As a result, plasma is initialized and stabilized.

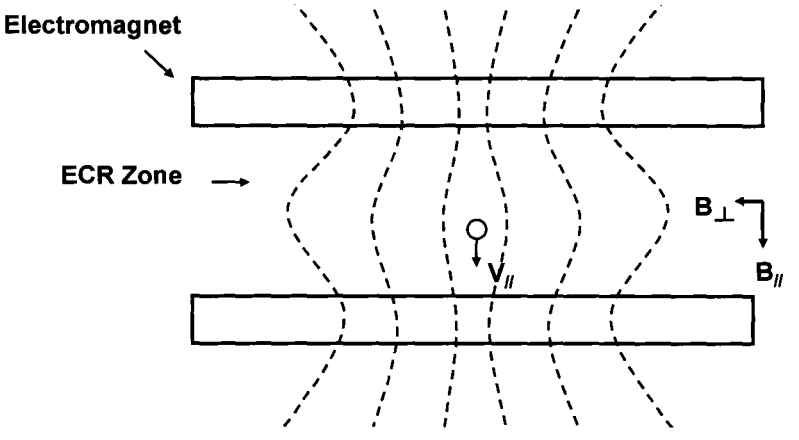

Figure 3.1 Magnetic field profile for the ECR-PECVD system (adapted from [90]).

The plasma properties such as stability, uniformity, ionization density and species details are quite dependent on the types of plasma gas molecules. The gas molecules with better ability to absorb energy and dissipate it through non-ionizing interactions usually form more stable plasmas. Comparing with diatomic gas molecules such as O_2, Ar tends to generate more uniform plasmas since the former can dissipate energy in more ways due to their more complex molecular structures. In addition, the ionization energy itself also varies significantly with the species of gas molecules.

A "mirror confinement" magnetic field profile is established by which most of the energetic particles can be confined in the plasma region. At lower magnetic fields, the non-uniform magnetic field produces a component $B_{\perp}$ perpendicular to the predominant magnetic field direction $B_{//}$. $B_{\perp}$ exerts a force $F_{\perp}$ on the particle in the opposite direction to that of the magnetic field. When the particle moves downward, energy is transferred from the motion parallel to $B_{//}$ to the motion perpendicular to $B_{//}$. The parallel momentum will decrease accordingly. Since the magnetic field does not do any work, the total energy of the particle should be conserved. If there is not enough parallel momentum to meet the energy conservation requirement, the particle will be reflected back to the ECR plasma zone.

There exists a loss cone in the velocity space for the particles. The particles can escape from the loss cone only when the ratio of parallel momentum to total momentum

of the particle exceeds a critical value. This critical value is determined by the magnetic profile which can be adjusted to control the number and energy of the escaped particles. As a result, only the particles with moderate energies are extracted for the deposition, therefore the bombardment by high energy particles of the substrate is avoided. In addition, since most of the energetic particles are reflected back to the plasma zone, they can continue to excite, ionize and dissociate more gas molecules to further increase the plasma density.

3.2 McMaster ECR-PECVD System

Figure 3.2 shows the schematic diagram of McMaster ECR-PECVD system [91]. A magnetron operates at a frequency of 2.45 GHz. Although the magnetron is capable of generating power up to 1200 W, the value varies from 300 to 700 W for the depositions in this thesis.

The microwaves are coupled into a circulator and directional coupler, which measure and limit the reflected power seen by the magnetron. Then the microwaves are guided into the impedance-matching waveguide whose impedance can be manually adjusted through three stub tuners to maximize the output power. Finally the microwaves pass through an aperture-coupled cylindrical microwave cavity, impinge on the quartz coupling window and enter the ECR plasma zone.

The ECR plasma zone is defined by the upper and lower electromagnets. To satisfy the resonance condition, the magnetic field is set at 875 Gauss. The upper and lower

magnets carry currents of 180 and 115 A, respectively, which produce an asymmetric mirror confinement magnetic field. The gases Ar and O_2 are introduced from the upper dispersion ring for the plasma generation. O_2 also serves as the source of O in the films. Once the microwaves are applied, the plasma will be initialized and stabilized in a short time, typically a few seconds. The Ar and O ions, as well as electrons with appropriate energy will be extracted from loss cone and stream down to the reaction zone.

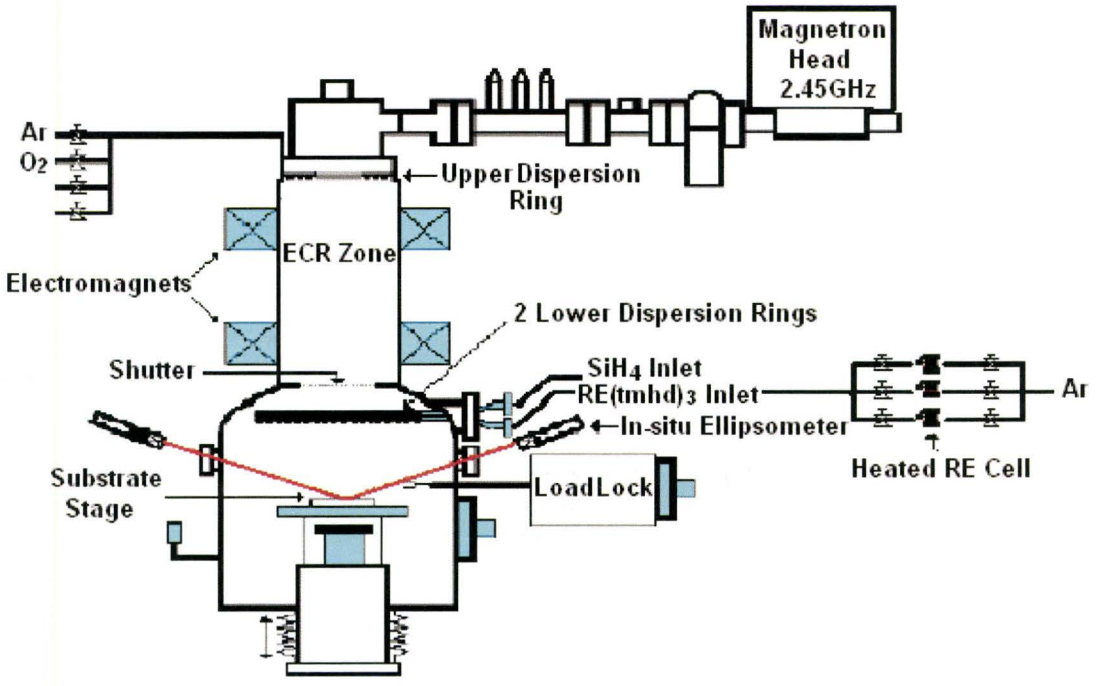

Figure 3.2 Schematic diagram of the McMaster ECR-PECVD system (adapted from [91]).

There is a retractable shutter between the ECR plasma zone and the reaction zone

which can be closed before the plasma becomes stable or after the desired deposition is completed. The Si and RE sources, SiH_4 and RE metal-organic precursors, are introduced from two lower dispersion rings below the shutter. The dispersion rings are carefully designed so that the gas is delivered uniformly to the substrate. The SiH_4 and RE sources are introduced from the downstream instead of the main body of the plasma, because they are easier to dissociate than O_2 molecules.

A multidopant delivery system allowing the simultaneous incorporation of up to three types of RE elements is installed which opens the possibility for fabrication of white light emitting Si structures. The dispersion ring for the RE source is connected to the RE transmission line. The other end of the transmission line is connected to three RE manifold containers. Additionally, the manifold has two spare containers which can be charged with different RE elements and replaced any time with the existing ones .This gives tremendous flexibility in terms of RE selection. The VCR-4 connection of the manifold containers also allows for exchange and/or charging process with little wasted time. The temperature of three RE manifold containers, the transmission line and the RE dispersion ring can be independently controlled by five Eurotherm temperature controllers. The RE manifold containers can be heated up to 200 ^{o}C to sublime the precursor inside. The temperatures of the transmission line and dispersion ring should always be set about 40 ^{o}C higher to avoid the condensation of the residual gas inside.

Additional Ar carrier gas is used to transport the RE precursor vapour. The flow rates of all the gas sources (including Ar and O_2 introduced from the upper dispersion ring) are controlled independently by a central mass flow controller panel. The gas flow fluctuation is about 7-8%.

Once SiH_4 and RE metal-organic molecules are introduced into the reaction zone, they are dissociated during the collisions with the energetic particles extracted from the ECR plasma zone, and highly reactive radical species are created. Those species react with each other on the substrate surface and lead to the film deposition. The energies of the particles impinging the substrate are determined by the difference between the plasma potential and the floating potential of the substrate. Usually the energies of the impinging ions are less than 20 eV.

Although the correlation between film composition and deposition parameters is complicated, the Si and O content of the film still is largely a function of the ratio of SiH_4 to O_2 gas flows. The efficient incorporation of RE elements is determined not only by the RE manifold temperature, but also many other parameters such as microwave power and absolute gas flow rates. It should be noted that different RE exhibit different dependences of incorporation efficiency on the deposition parameters and require individual studies. A detailed discussion of the correlation between the RE incorporation and various deposition parameters is given in Chapter 6.

The substrate stage is placed directly below the center of the dispersion ring. Although the stage location can be adjusted vertically, and the stage temperature can be varied from room temperature to 800 °C, for the depositions in the thesis they were fixed at 15 cm below the dispersion ring and 350 °C, respectively. During the deposition, the stage is rotated at a frequency of 20 revolutions per minute (rpm) to achieve a better film uniformity. The thin film growth can be monitored during the deposition by an *in-situ* ellipsometer operating at 632.8 nm.

The ECR-PECVD system base pressure is kept at 10^{-7} Torr and the deposition pressure varies from 2 to 5 millitorr depending on the gas flow rates. The vacuum pumping system is composed of four pumps. The chamber is continuously evacuated by a diffusion pump for which a roots blower pump and a mechanical rotary vane pump are used for backing and rough pumping. The load lock is pumped by a turbomolecular pump, for which the same mechanical rotary vane pump is used for backing.

Chapter 4

Fundamentals of Rutherford Backscattering Spectrometry

RBS is a non-destructive technique for quantitative analysis of both surface composition and the composition depth profile of a material. The experimental setup is given in Figure 4.1 [92]. A collimated beam of MeV He ions is incident on a planar sample. Particles scattered backwards to an angle θ are detected by a solid state nuclear particle detector which has an output voltage pulse proportional to the energy of detected particles.

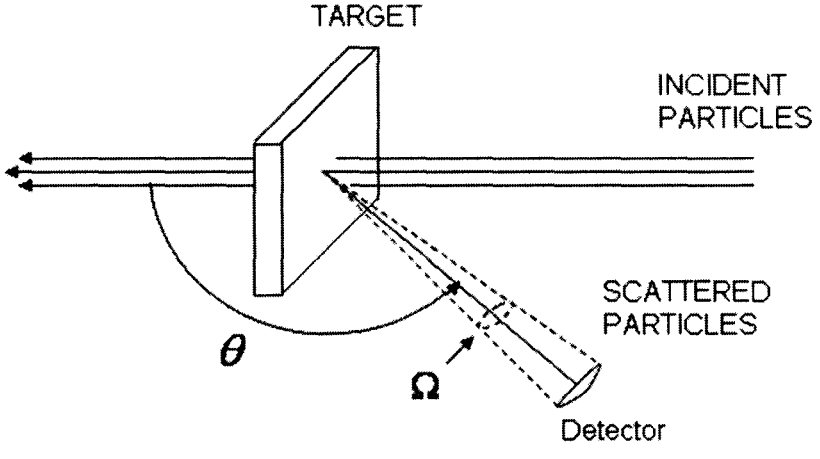

Figure 4.1 Schematic of the experimental set up for RBS (adapted from [92]).

This technique is based on the model of single-collision, large-angle scattering of incident particles by the nucleus of target atoms. The scattered particle energy after the collision provides the identity of the target atoms, while the probability of the collision determines the number of target atoms per unit area.

The collision between incident particle and stationary target atom is considered as elastic, so the energy transfer and kinematics of two particles can be fully solved by applying the principles of conservation of energy and momentum.

For a projectile of mass M_1 with initial kinetic energy E_0 and a stationary target atom of mass M_2, the energy of the projectile and the target atom after collision are E_1 and E_2 respectively. The scattering angle is θ. The ratio of the projectile energy E_1/E_0 for $M_1<M_2$, is given by:

$$\frac{E_1}{E_0} = \left[\frac{(M_2^2 - M_1^2 \sin^2 \theta)^{1/2} + M_1 \cos\theta}{M_1 + M_2} \right]^2 \tag{4.1}$$

This ratio is defined as the kinematic factor K which suggests that the particle energy after the collision is only determined by the particle masses and the scattering angle. The preferred location for the detector is θ=180°, since at this point the atomic mass difference between constituent elements of target give the largest change of K, while in practice θ is around 170° because of detector size.

The physical law governing the interaction between the projectile and the target atom is Coulomb's law. The scattering cross section (or probability) $\sigma(\theta)$ of the

collision can be derived from there and is given by:

$$\sigma(\theta) = (\frac{Z_1 Z_2 e^2}{4E_0})^2 \frac{4}{\sin^4 \theta} \frac{\left(\left\{1-\left[(M_1/M_2)\sin\theta\right]^2\right\}^{1/2} + \cos\theta\right)^2}{\left\{1-\left[(M_1/M_2)\sin\theta\right]^2\right\}^{1/2}} (1 - V_{interaction}) \tag{4.2}$$

where

$$V_{interaction} = \frac{0.04873\ Z_1 Z_2{}^{4/3}}{M_2 E_0 /(M_1 + M_2)} \tag{4.3}$$

in which Z_1 and Z_2 are the atomic numbers of the projectile and target atoms, and $V_{interaction}$ is a correction for electron screening.

For a thin surface coverage, the areal density of the constituent of interest Ns and yield of elastically scattered particles Y is related by the scattering cross section $\sigma(\theta)$ and is given by:

$$Y = \sigma(\theta) \cdot \Omega \cdot Q \cdot N_s \tag{4.4}$$

where Q is the total number of the incident particles in the beam and Ω is the detector solid angle. In practice, the above yield equation can also be used to calibrate the solid angle value of the detector by measuring a reference sample with known areal density of a dopant.

When an incident particle penetrates the target material, it loses energy continuously through excitation and ionization in inelastic collisions with electrons. Energy loss can be

expressed by the stopping cross section $\frac{dE}{dx}$. For targets that contain more than one element, the total stopping cross section dE/dx of a material of composition A_mB_n is given by:

$$\frac{dE}{dx} = m\frac{dE}{dx}\bigg|_A + n\frac{dE}{dx}\bigg|_B \tag{4.5}$$

This postulate is known as Bragg's rule, in which $\frac{dE}{dx}\big|_A$ and $\frac{dE}{dx}\big|_B$ are the stopping cross sections of the atomic constituents A and B. The energy width of the signal from a thin film of thickness t is:

$$\Delta E = t\ (K\frac{dE}{dx}\bigg|_{in} + \frac{1}{|\cos\theta|}\frac{dE}{dx}\bigg|_{out}) \tag{4.6}$$

where $\frac{dE}{dx}\big|_{in}$ and $\frac{dE}{dx}\big|_{out}$ refer to the stopping cross sections for the incident particle on the way in and out. It is explicit that the energy width is directly proportional to the thickness of the material [93].

The RBS spectrum represents the superposition of signals for all the existing elements from different depths in the film. Figure 4.2 shows a representative RBS spectrum for sample Ce031. The energies related to the surface Ce, Ar, Si and O atoms are as indicated. The signal from O sits on the signal from Si in the substrate and depresses the signal from Si in the film. Si, O and Ce all exhibit a uniform concentration distribution through out the whole depth. It can be seen that the Ce peak is well removed

from that of other elements, since its large atomic mass gives rise a large kinematic factor K. This feature makes the RBS technique particularly sensitive for the detection of heavy RE elements doped in a light matrix, such as SiO_2.

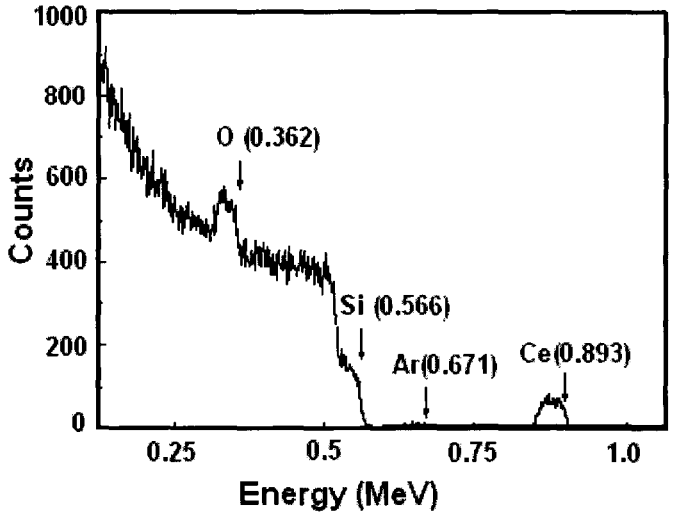

Figure 4.2 A representative RBS spectrum for sample Ce031. The surface energies of Ce, Ar, Si and O are indicated by arrows.

Chapter 5

Experimental Details

This chapter presents the preparation and characterization details of the RE-doped silicon oxide films discussed in the thesis. The deposition conditions, post-deposition annealing treatments, ellipsometry, RBS and PL measurement details are described. The films were also analyzed by FTIR spectroscopy and HR-TEM to elucidate the correlation between PL properties and the film structures.

5.1 Deposition Conditions

A total of thirty RE(Ce, Eu, Tb and Er) doped silicon oxide samples were deposited by ECR-PECVD including eleven Ce-doped samples, seven Eu-doped samples, nine Tb-doped samples and three Er-doped samples. Each sample was designed containing no more than one type of RE element. They can be further subdivided into oxygen-rich and silicon-rich films according to containing either excess O or Si relative to stoichiometric SiO_2.

For all the depositions involved in this study, the upper and lower electromagnet currents were fixed at 180 and 115 A, respectively. The discharged microwave power was

fixed at 500 W for Ce, Eu and Er-doped samples, while it was varied from 300 to 700 W for Tb-doped samples to study the effect of microwave power on the amount of Tb incorporation. In order to achieve the expected discharge power, the forward power was set at 10 to 30 W higher than the expected value, then the stub tuners were adjusted to minimize the reflected power. For all the depositions, the temperature of the substrate heater was fixed at 350 °C. As a result, the actual substrate stage temperature was around 120 °C. The substrate was rotated at 20 rpm to improve the film uniformity.

The plasma gases were 10% O_2 diluted in Ar, and pure Ar. The silicon precursor was 30% SiH_4 diluted in Ar. The RE sources were volatile metal-organic chemicals, *Tris(2,2,6,6-teramethyl-3,5- heptanedionato)- RE(III)* ($RE(tmhd)_3$). Their sublimation products in Ar carrier gas were used as RE precursors. For all the depositions, the chamber vacuum was maintained below 3 millitorr.

It is well known that the Si/O ratios in the films can be controlled by the relative SiH_4 and O_2 gas flow rates. Although in principle, the RE incorporation in the films can be increased by increasing the RE source container (or RE cell) temperature, which determines the RE precursor vapour pressure in the reaction chamber during the deposition, there are certain limits to this in practice. The transmission line and the dispersion ring have to be heated to temperatures 20 - 40 °C higher than that of the RE cell to avoid the possible condensation occurring in the delivery pathway. Heating at

temperatures over 220 °C will break through the currently employed thermal isolation layer around the transmission line. Therefore the upper limit of the RE cell temperature is around 200 °C for the depositions in this study. Obviously this limit can be increased through updating the thermal isolation layer in the future. The ultimate limit, however, would be around 300 °C, since a greater temperature may cause conventional thermal CVD processes to occur around the dispersion ring. Under this limit, several other parameters including absolute SiH_4 and O_2 gas flow rates, Ar carrier gas flow rates and microwave power were varied to enhance RE incorporation in the films. Two types of Si substrates were used to meet the requirements for different characterization techniques: the single-side polished Si substrate for RBS, PL and TEM experiments and the double-side polished Si substrate for FTIR spectroscopy analysis. The deposition was monitored by an *in-situ* ellipsometer operating at 632.8 nm, and the deposition time was varied accordingly to produce the desired thickness. Considering the contraction of the films during the cooling process, the actual thicknesses of all samples were determined by an *ex-situ* ellipsometer operating at 632.8 nm. The detailed deposition parameters for all the samples are given in Table 5.1. The table is colour-coded according to dopant type.

There are two types of gas flow rate units involved in this study, since the mass flow controller (MFC) was changed once during the experiments. Both MFCs are from MKS Instruments. The gas flow unit is mV for the former MFC, and standard cubic centimetres

per minute (sccm) for the latter one. The two sets of flow rates can be converted by matching the deposition pressure caused by various gas flows, and the conversion work is under way.

Table 5.1 Summary of the deposition parameters that were controlled and their values for all the depositions in this study.

Sample	Forwarded Power [W]	Reflected Power [W]	SiH_4 Flow Rate	O_2 Flow Rate	RE Cell Temp [°C]	Ar Flow Rate	Deposition time [min]
Ce003[1]	515	5	25	70	161	12	7:40
Ce009[1,2]	510	5	11	78	100	12	20:40
Ce010[1,2]	506	6	11	78	120	12	20:40
Ce011[1, 2]	506	6	11	78	140	12	20:40
Ce012[1,2]	506	6	11	78	160	12	20:40
Ce024[3]	509	9	5	30	120	25	8:30
Ce025[3]	509	9	5	30	140	25	8:30
Ce026[3]	503	6	5	30	160	25	10:10
Ce029[3]	507	7	4	40	180	25	10:10
Ce030[3]	509	7	3	30	180	10	15:00
Ce031[3]	509	7	2	30	200	10	15:00
Eu016[1]	510	10	12	94	120	25	17:00
Eu017[1]	510	10	12	94	140	25	17:00
Eu018[1]	510	10	12	94	160	25	17:00
Eu019[1]	510	6	12	94	160	50	17:00
Eu020[3]	508	8	5	30	120	25	8:30
Eu021[3]	512	12	5	30	140	25	8:30
Eu022[3]	508	8	5	30	160	25	8:30
Tb007[1]	610	10	20	60	150	25	9:00
Tb008[1]	607	7	20	60	140	25	9:00
Tb009[1]	608	7	20	60	160	25	9:00

[1] It is deposited using old mass flow controller, and the corresponding flow rate unit is mV.

[2] It is deposited on double-side polished Si substrate.

[3] It is deposited using new mass flow controller, and the corresponding flow rate unit is sccm.

Table 5.1 (continued)

Sample	Forwarded Power [W]	Reflected Power [W]	SiH_4 Flow Rate	O_2 Flow Rate	RE Cell Temp [°C]	Ar Flow Rate	Deposition time [min]
Tb011[1]	327	27	20	56	156	25	9:30
Tb012[1]	500	5	20	56	153	25	9:30
Tb013[1]	705	5	20	56	155	25	9:30
Tb015[1]	420	10	7	24	160	30	30:00
Tb016[1]	420	10	7	24	160	20	30:00
Tb017[1]	420	10	7	24	160	10	30:00
Er242[3]	508	8	5	30	120	25	8:30
Er243[3]	512	12	5	30	140	25	8:30
Er244[3]	508	8	5	30	160	25	8:30

5.2 Post-deposition Annealing Treatments

After deposition, the samples were cleaved into small pieces for annealing. The annealing temperatures were 600, 700, 800, 900, 1000, 1100 and 1200 °C, and three annealing durations were used: 5 minutes, 1 hour and 3 hours.

For the 5-minute anneals, a JetFirst 100 rapid thermal annealing furnace was used which can precisely control the ambient gas flow, ramp rate and resultant annealing temperature through an annealing recipe. In this study, the samples were annealed under flowing pure N_2 gas, the system was programmed to ramp up from room temperature to the set temperature in 1.5 minutes, staying at set temperature for 5 minutes and cooling down in another 1.5 minutes.

For 1-hour and 3-hour anneals, a regular quartz tube furnace was employed. To

accommodate the samples, a quartz boat with a rod for loading and unloading was used. The samples were annealed in one of two flowing gases: pure N_2 or Ar+5% H_2. The furnace was preheated to the set temperature and purged by the flowing gas for 5 minutes, then the samples were slid to the center of the furnace tube. The samples were cooled down in the flowing gas after the annealing.

5.3 Post-deposition Characterizations

RBS measurements were done at the University of Western Ontario (UWO) to determine the compositions of all the as-deposited samples. The detector angle was fixed at 170°. A $^4He^+$ ion beam of 1 MeV was used. A dose of 1uC was collected for each sample. A reference sample with 4.7x $10^{15}/cm^2$ Bi implanted in Si was used for the calibration.

Ellipsometry experiments were done using a single-wavelength Philips PZ2000 ellipsometer with a HeNe laser operating at 632.8 nm to determine the optical thickness and refractive index of the films.

A single wavelength laser-excited PL spectroscopy system was used to study the emission properties of the films. The excitation source was a continuous wave 325 nm He-Cd laser with an output power of 17 mW and spectral bandwidth of 3 nm. The PL set up is capable of both room temperature and low temperature measurements in the wavelength ranges from 350 to 950 nm (visible) and 900 to 1700 nm (IR). A schematic

diagram of the PL measurement set-up is shown in Figure 5.1. Both mirror 1 and 3 are removable. The light paths for visible PL measurement have both mirror 1 and 3 are removed, for IR PL measurement only mirror 1 is removed. For low temperature PL measurements only mirror 3 is removed. However, only room temperature measurements were taken for this study.

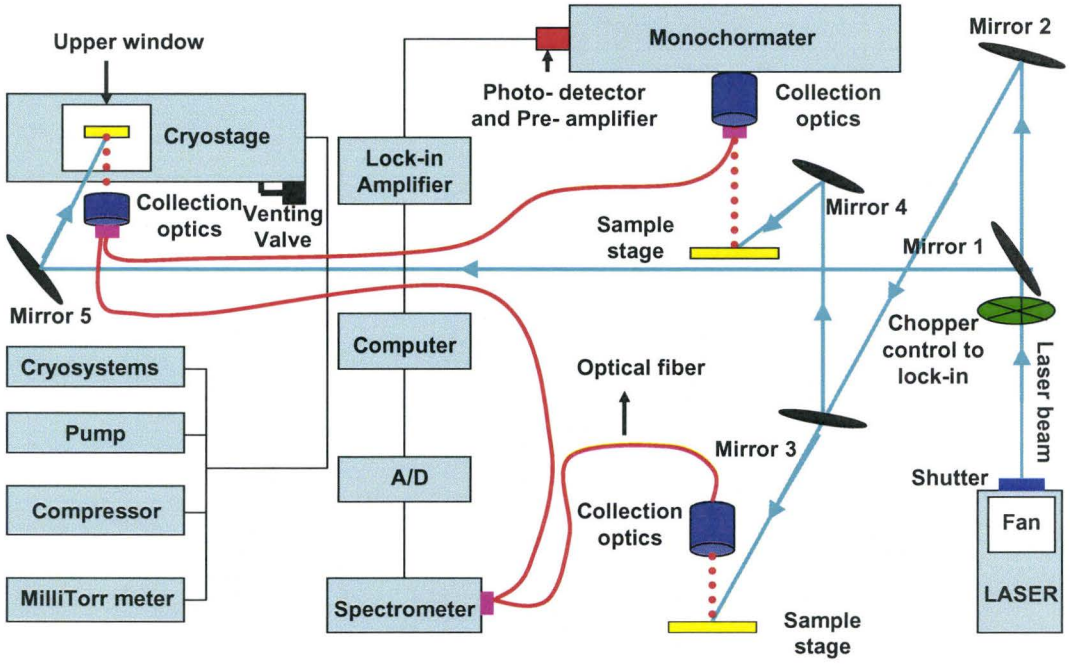

Figure 5.1 Schematic diagram of the room temperature and low temperature PL spectroscopy setup for visible and IR range measurements.

For visible PL measurements, the PL emission from the sample is collected by a collimating and focusing lens and coupled into an optical fiber, which is coupled to an

Ocean Optics 2000 grating spectrometer in which the signal is dispersed. The entire dispersed signal is incident on a linear charge coupled device (CCD) array. The signal is then converted by an A/D converter and analyzed using software OOII rad from Ocean Optics. For all the measurements in this study, the background spectrum was subtracted in advance. Since the measured value is the output optical energy per unit time per unit area per unit bandwidth, which is wavelength dependent, a conversion from spectral radiance to photon flux was conducted to achieve a flat spectral response.

For IR PL measurements, the incident laser beam was modulated at the chopper frequency and resulted in a modulated PL emission from the sample. The emission was collected by a collimated and focusing lens and directed into a SpectraPro-500i grating monochromator followed by an ID441 InGaAs photodetector. A stepper motor was used to rotate the grating, so only light of a narrow wavelength band enters the photodetector at any given time. The emission of a range of wavelengths was scanned in sequence. The output from the photodetector then was directed into a lock-in amplifier which is also connected to the chopper. The signal is converted by an A/D converter and read by a custom written Labview software. Since the spectral response of the system is flat from 1350-1650 nm, no correction of the PL spectra is necessary [91, 94].

FTIR absorbance spectra were acquired using an ABBomen Work IR 100 FTIR spectrometer to study the bonding structures in the films. The scans were in the range

from 400 to 4000 cm^{-1}, and the resolution was set at 4 cm^{-1}. The FTIR samples were deposited on double-side polished Si substrates. The substrate signals were subtracted from the measured spectra. To facilitate the comparison between the measured spectra and the spectra from the literature, several absorbance spectra were converted to transmittance spectra through:

$$\text{absorbance} = -\log_{10}(\text{transmittance}) \tag{5.1}$$

HR-TEM images were obtained using a JEOL JEM-2010F scanning transmission electron microscope (STEM) to explore the formation of new crystal structures in the films. In order to study the local compositions of some specific spots and the interface diffusion induced by high temperature annealing, elemental mapping and line scan analysis was also conducted using x-ray energy dispersive spectroscopy (XEDS). The cross-section TEM samples were prepared following standard procedures including polishing, dimpling, buffering and ion milling [95].

Chapter 6

Studies of Film Compositions

The RE emission is highly dependent on the film composition with two main variables involved: RE concentration and excess Si content. The RE concentration determines the upper limit of available optically active RE ions, while the presence of excess Si can result in the formation of Si-ncs which may affect the excitation mechanism of RE ions. This chapter summarizes the composition, thickness and refractive index of all as-deposited films discussed in this study. The correlation between some deposition parameters and RE incorporation is discussed.

6.1 Summary of Film Composition and Thickness

Table 6.1 shows the composition, optical thickness and refractive index of the as-deposited samples studied in this thesis. The table is colour-coded to organize the sample compositions into two categories: oxygen-rich (orange) and silicon-rich (yellow). The composition of the samples was determined quantitatively by RBS measurements, and the optical thickness and refractive index were determined by ellipsometry measurements. For the reader's convenience, portions of this table will be reproduced at

the beginning of the discussion for a particular group of samples.

Table 6.1 Summary of the composition, thickness and refractive index for all the as-deposited samples involved in this study.

Sample	Absolute Atomic Areal Density[4] [x10^7 atoms/ cm^2]				Si[5] [at.%]	RE[6] [at.%]	Thickness [Å]		Index of Refraction[8]
	Si	O	RE	Ar			RBS[7]	Optical[8]	
Ce003	2.53	3.76	0.002	0.004	40.16	0.04	950	970	1.70
Ce009	2.6	5.19	0.0009	0.081	33.33	0.01	1150	1241	1.47
Ce010	2.52	5.29	0.0015	0.093	32.26	0.02	1150	1227	1.47
Ce011	2.62	5.51	0.0037	0.097	32.26	0.04	1200	1254	1.47
Ce012	2.58	5.29	0.0057	0.088	32.79	0.07	1180	1230	1.47
Ce024[9]	N/A	N/A	0	N/A	N/A	0	N/A	940	1.58
Ce025[9]	1.99	3.59	0	0.038	35.71	0	840	845	1.56
Ce026[9]	2.32	4.18	0	0.044	35.71	0	980	984	1.55
Ce029	1.82	3.81	0.0052	0.086	32.26	0.09	850	870	1.48
Ce030	2.27	4.65	0.0125	0.128	32.26	0.18	1050	1037	1.51
Ce031	1.42	3.00	0.0408	0.055	32.04	0.90	700	684	1.51
Eu016[10]	2.00	4.49	0.010	0.076	30.77	0.16	970	970	1.48
Eu017[10]	1.96	4.42	0.011	0.061	30.77	0.17	950	947	1.48
Eu018[10]	2.00	4.39	0.007	0.064	31.25	0.11	950	947	1.48

[4] The error for the areal atomic densities is around 2-3%.

[5] It refers to the atomic fraction [Si]/ ([Si]+[O]).

[6] It refers to the atomic fraction [RE]/ ([Si]+[O]).

[7] It is based on the assumption that film density equals that of SiO_2 (2.26g/cm^3).

[8] It is achieved through ellipsometry measurements for as-deposited films and based on the assumption that the absorption coefficient of the films is 0.

[9] The composition of this film actually cannot be determined quantitatively. The perfect match between simulation and experimental spectrum can only be achieved when the Si/O ratio of the film is estimated as an unreasonable value. Since no appreciable RE peak was observed in the RBS spectrum, the RE content was taken to be 0.

[10] According to RBS and PL results, the film contains significant Tb and Er contamination and no or very little Eu. Therefore, the related characterization results are excluded from the discussions in this thesis.

Table 6.1 (continued)

Sample	Absolute Atomic Areal Density [x10^7 atoms/ cm^2]				Si [at.%]	RE [at.%]	Thickness [Å]		Index of Refraction
	Si	O	RE	Ar			RBS	Optical	
Eu019[10]	2.35	5.28	0.012	0.056	30.77	0.15	1130	1129	1.48
Eu020	2.26	4.07	0	0.04	34.78	0.02	974	975	1.59
Eu021	2.14	4.06	0.008	0.02	34.48	0.12	940	946	1.59
Eu022	2.58	4.76	0.185	0.026	35.16	2.15	1350	1270	1.58
Tb007	2.38	4.21	0.00689	0.038	36.1	0.1	1000	1053	1.57
Tb008	2.37	4.22	0.0064	0.043	35.97	0.1	1000	1025	1.58
Tb009	2.37	4.22	0.00687	0.042	35.87	0.1	1000	1015	1.57
Tb011	1.64	2.7	0.00851	0	37.74	0.2	662	716	1.65
Tb012	2.09	3.76	0.00163	0.004	35.71	0.28	900	938	1.66
Tb013	2.65	4.91	0.00903	0.066	35.09	0.1	1150	1151	1.61
Tb015	2.13	4.59	0.0517	0.083	31.75	0.75	1060	1059	1.50
Tb016	1.88	4.17	0.0256	0.072	31.25	0.42	922	920	1.49
Tb017	2.14	4.6	0.0248	0.043	31.75	0.36	1020	1018	1.50
Er242	2.08	3.86	0.00721	0.040	35.09	0.12	900	903	1.57
Er243	2.75	5	0.132	0.024	35.48	1.46	1370	1352	1.59
Er244	6.34	11.4	1.01	0	35.7	4.76	766	731	1.72

There are two types of thickness given: RBS thickness and optical thickness. The optical thickness is taken as the accurate value, since the thickness achieved from RBS simulations includes the assumption that the film volume density equals that of thermally grown SiO_2 (2.26g/cm^3). The areal density achieved from RBS measurements is an absolute value and it equals the product of the film thickness and volume density. So the actual volume density can be estimated by comparing RBS and optical thickness, and a lower optical thickness indicates that the actual volume density of the films is higher than

2.26g/cm^3. A higher density was seen in Ce-doped samples with 0.2 at.% or greater doping, Eu-doped samples with 2.15 at.% doping, Tb-doped samples with 0.36 at.% or greater doping, and Er-doped samples with 1.46 at.% or greater doping. In general, higher RE doping leads to a higher volume density of the films.

The refractive index can be used to estimate the approximate Si concentration in the films. The refractive indexes of stoichiometric SiO_2 and pure Si are 1.46 and 3.52, respectively. Therefore a refractive index higher than 1.46 indicates that the film contains a higher Si concentration than that of stoichiometric SiO_2 due to the increase of Si-Si bonds in the films. The results in this study are completely consistent with this trend. In addition, it appears that only extremely high RE incorporation can increase the refractive index of the film (see Er244, on p.56).

6.2 Correlation between the Film Composition and the Deposition Parameters

Although there are a number of parameters in ECR-PECVD system that can be varied to control the deposition process, only three types of parameters were varied in this study to achieve the desired composition: precursor gas flow rates for SiH_4, O_2, and Ar carrier gas, RE cell temperature and microwave power. The effects of these parameters on the film composition are summarized in this section.

For all the samples studied in this study, it appears that the Si content in the films is

largely determined by the relative SiH_4 and O_2 gas flow rates regardless of different RE types and RE cell temperatures. It was also found that a greater microwave power may produce a lower Si/Si+O ratio (see Tb011, 012 and 013), which is probably due to the more efficient dissociation of O_2 molecules in the ECR plasma zone.

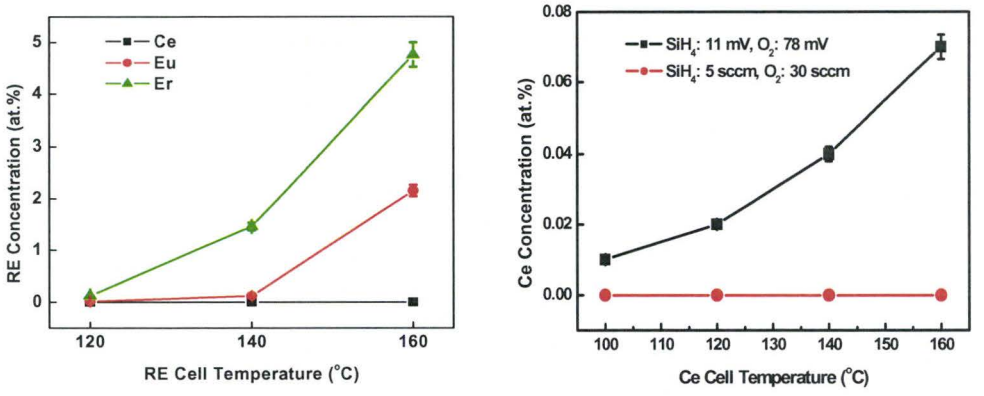

(a) (b)

Figure 6.1 RE concentration as a function of RE cell temperature for Ce, Eu and Er-doped samples using two sets of SiH_4 and O_2 gas flow rates (a) Ce, Eu and Er-doped samples, SiH_4: 5 sccm, O_2: 30 sccm, (b) Ce-doped samples[11].

Figure 6.1 (a) and (b) depict RE concentrations as a function of RE cell temperature, two sets of gas flow rates were employed. The RE concentration increases monotonically with increasing RE cell temperature for Eu and Er-doped samples, while no appreciable Ce incorporation was observed for the same gas flow rates. For the other set of gas flow rates, the Ce concentration was observed to increase with increasing cell temperature,

[11] Two types of mass flow controllers (MFC) are employed here (see more detailed information on p.48)

while the maximum concentration is as low as 0.07 at.%.

Generally a greater RE cell temperature leads to a higher RE precursor vapour pressure in the reaction chamber through enhancing the sublimation yield of the RE source. Thus a higher species ratio of RE to Si and O in the reaction chamber results in a higher RE concentration in the film. A high RE source sublimation point corresponds to a low sublimation yield at a certain cell temperature and results in a low RE concentrations. Therefore the high sublimation point is mainly responsible for the relatively inefficient incorporation of Ce in the films. However, the relative ratio of RE to Si and O can also be increased by reducing the quantity of Si and O species which is determined by the absolute value of SiH_4 and O_2 gas flow rates. The dependence of the Ce concentration on gas flow rates illustrates this point. It should be noted that the incorporation of RE ions is also influenced by the relative SiH_4 and O_2 flow ratios. A previous study on Er-doped silicon oxide deposited by ECR-PECVD [26] found that a higher O_2/SiH_4 ratio resulted in a greater Er incorporation. It was suggested that the increase of oxygen may facilitate the formation of Er_2O_3 which has a lower vapour pressure than pure Er and tends to be absorbed by the film surface.

The effects of microwave power on Tb incorporation are shown in Figure 6.2, and the optimum microwave power is 500 W. It is possible that microwave powers less than 500 W are incapable of efficiently cracking the plasma gas molecules to produce sufficiently

energetic particles for dissociation of Tb precursor molecules, and result in a less Tb incorporation. For powers greater than 500 W, a high yield of oxygen-related energetic species causes a smaller ratio of Tb to Si and O in the reaction chamber and less Tb incorporation.

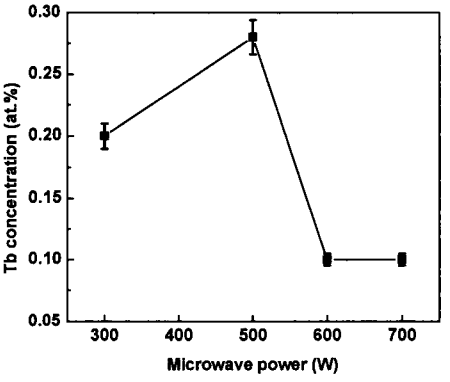

Figure 6.2 Tb concentration as a function of microwave power with other parameters kept constant.

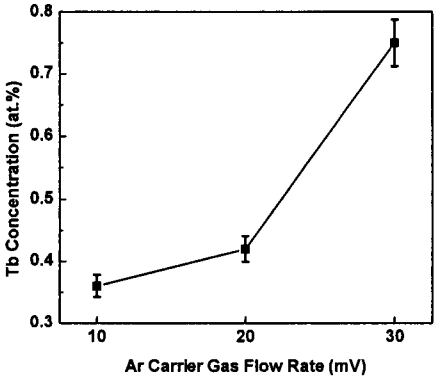

Figure 6.3 Tb concentration as a function of Ar carrier gas flow rates with other parameters kept constant.

The effect of Ar carrier gas flow rate on Tb concentration is depicted in Figure 6.3. Generally, Tb incorporation increases with increasing Ar carrier gas flow rates. The increase of Ar carrier gas flow may facilitate the delivery of Tb precursor sublimation product and increase its vapour pressure in the reaction chamber. As a result, Tb incorporation was enhanced with Si/O ratios largely unaffected.

In summary, although many deposition parameters for ECR-PECVD are coupled to each other, there are certain rules that can be followed to achieve a desired composition. The optimum microwave power is 500 W. The relative Si and O contents of the films are determined by SiH_4 and O_2 gas flow ratios. RE doping can be increased by increasing the RE cell temperature and Ar carrier gas flow rate or by reducing the absolute value of SiH_4 and O_2 gas flow rates. A relatively higher O_2 gas flow may lead to a more efficient RE incorporation. By applying these rules, silicon oxide with close to stoichometric compositions and Ce doping as high as 0.9 at.% has been achieved. A greater Ce incorporation can be expected by further increasing Ar gas flow rates or reducing SiH_4 and O_2 gas flow rates proportionally. In addition, lower SiH_4 and O_2 gas flow rates may also lead to a lower deposition rate and a higher film quality. A previous study on SiO_xN_y deposited by ECR-PECVD [90] suggested that whole SiH_4 molecules were incorporated into the films. During the subsequent annealing process, densification occurred by driving SiH_4 molecules out of the films. This process is possibly responsible for the delamination

observed from many annealed film, which often exhibit no or very weak emission in PL measurements. At lower SiH_4 and O_2 gas flow rates, SiH_4 molecules may have a greater chance to be cracked efficiently before streaming down to the film surface. Therefore, less SiH_4 incorporation and delamination effects of the films can be expected.

Chapter 7

Studies of Ce-doped Silicon Oxides

7.1 Evolution of PL with Nitrogen Annealing

7.1.1 Oxygen-rich Films

Sub-section of Table 6.1

Sample	Absolute Atomic Areal Density [x10^7 atoms/ cm^2]				Si [at.%]	RE [at.%]	Thickness [Å]		Index of Refraction
	Si	O	RE	Ar			RBS	Optical	
Ce009	2.6	5.19	0.0009	0.081	33.33	0.01	1150	1241	1.47
Ce010	2.52	5.29	0.0015	0.093	32.26	0.02	1150	1227	1.47
Ce011	2.62	5.51	0.0037	0.097	32.26	0.04	1200	1254	1.47
Ce012	2.58	5.29	0.0057	0.088	32.79	0.07	1180	1230	1.47
Ce029	1.82	3.81	0.0052	0.086	32.26	0.10	850	870	1.48
Ce030	2.27	4.65	0.0125	0.128	32.26	0.18	1050	1037	1.51
Ce031	1.42	3.00	0.0408	0.055	32.04	0.90	700	684	1.51

7.1.1.1 PL spectral features for Ce-doped Oxygen-rich Silicon Oxide (Ce:ORSO)

To illustrate the structural features of the PL spectra for Ce:ORSO samples, the representative PL spectra for Ce011 and Ce031, as deposited and annealed in flowing N_2

at various temperatures for 1 hour are depicted in Figure 7.1. PL spectra of the low Ce concentration sample, Ce011, exhibit two broad bands for various annealing temperatures. The first band is in the range 350-700 nm with a primary peak centered at about 450 nm and a weak shoulder at longer wavelengths. The second band is in the range 800-950 nm. The peak positions and line-shapes of these two bands change slightly with the annealing temperature. PL spectra of the high Ce concentration sample, Ce031, exhibit two PL bands comparable to that of Ce011, while the weak shoulder of the 350-700 nm band becomes much less pronounced.

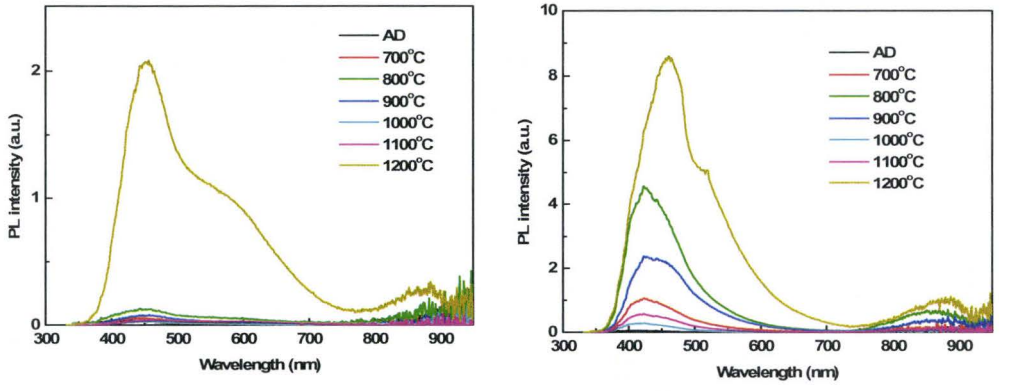

Figure 7.1 Representative PL spectra for Ce:ORSO as deposited and after annealing in flowing N_2 at various temperatures for 1 hour. (a) Ce 011 (b) Ce031

There are two classes of luminescence centers that may be responsible for the 350-700 nm band: Ce^{3+} ions and radiative oxide defects. As noted previously, the 5d-4f

transition of Ce^{3+} has a broad absorption band in the UV range and a broad emission band in the UV to blue range. Although there are no characteristic line-shapes and peak positions for Ce^{3+} luminescence due to the nature of the 5d-4f transition, the 350-700 nm band is still comparable to that of Ce:SiO_2 prepared by CVD or sol-gel methods [52, 57]. Ce^{3+} ions appear as the main contributor to the 350-700 nm PL band since the structural features and PL intensity of this band are strongly correlated with the Ce concentration. Although a number of radiative oxide defects with a wide range of emission wavelengths from 300 to 650 nm have been found in amorphous SiO_2, three of them are most likely to exist in ORSO including weak oxygen bonds (WOB), peroxy radicals and non-bridging oxygen hole centers (NBOHC) whose typical emission wavelengths are 415, 550 and 620 nm, respectively. The formation of these defects is related to the large quantity of interstitial oxygen atoms existing in ORSO [96, 97, 98, 99, 100, 101].

It is tempting to ascribe the 800-950 nm band to the formation of a small quantity of Si-ncs, since Si-ncs PL is usually peaked in a similar range. It is true that although there is no excess Si in oxygen-rich films as determined by RBS measurements, a small quantity of Si-ncs may still form in local areas due to the local imbalance of the Si distribution. However, if this PL band were indeed due to the Si-ncs, one would expect two phenomena according to the study on Ce:SRSO in this thesis (See section 7.1.2): the enhancement of the PL intensity with increasing temperature for annealing temperatures

below 1200 °C due to quantum confinement effects, and significant quenching at 1200 °C due to the coupling between Si-ncs and Ce^{3+} ions. In actuality, they were not seen to occur. On the other hand, the same dependences of the peak position and PL intensity on the annealing temperature are observed for 350-700 nm and 800-950 nm bands. One possibility is that the 350-700 nm band is related to those radiative oxide defects coupled to Ce^{3+} ions. Although most of oxide defects tend to be removed during annealing, it is impossible to eliminate all of them due to the large quantity of excess oxygen in oxygen-rich films. Of the three types of radiative oxide defects, NBOHC is the most stable and most likely remained. As noted previously, typical emission wavelengths for NBOHCs are about 620 nm. However, the emission for radiative oxide defects are quite sensitive to their local environments, consequently their peak position, spectral shape and intensity vary significantly with film compositions and annealing treatments. Therefore, the emission wavelength for NBOHC can possible shift to longer wavelengths, since its local environment has been changed by the presence of Ce^{3+} ions in the vicinity.

7.1.1.2 Gaussian Deconvolution of PL spectra

In order to find the overlapping peaks and discriminate the luminescence centers, the PL spectra for four low Ce concentration samples, as deposited and annealed at various temperatures were decomposed into two Gaussian components, peak 1 and 2. Excellent fits were achieved for every individual spectrum and chi-square values were not greater

than 10^{-4}. Figure 7.2 shows three representative Gaussian fits for Ce011, as deposited and annealed at 800 and 1200 °C. A summary of the details for all achieved Gaussian components is given in Table 7.1.

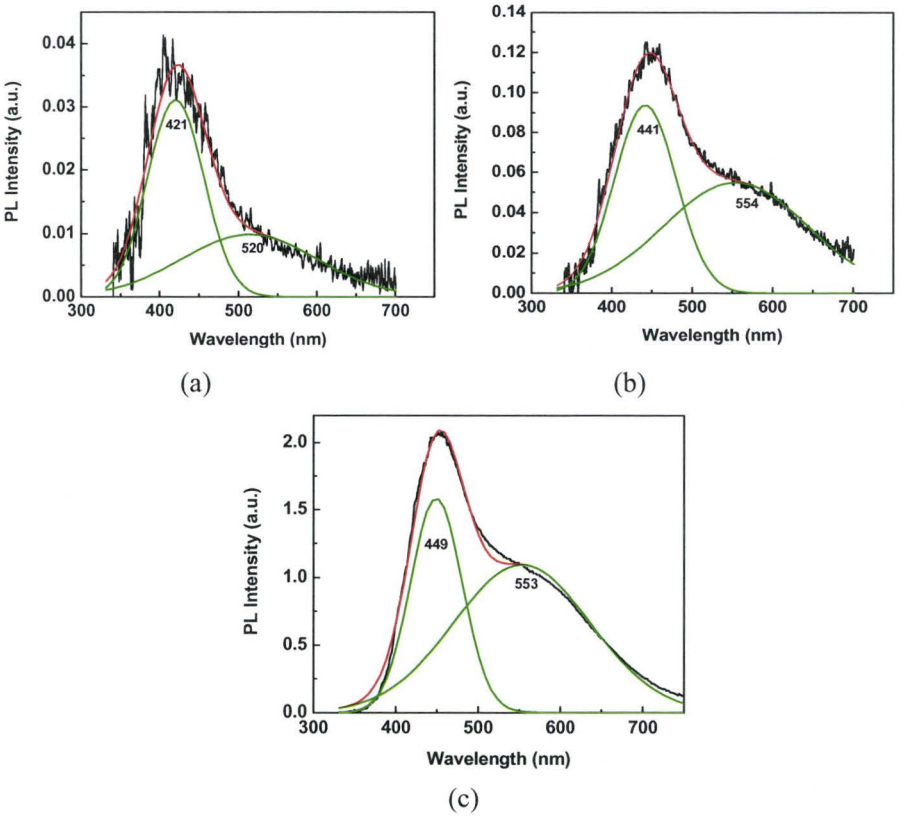

Figure 7.2 Gaussian deconvolution of representative PL spectra for Ce011. (a) as deposited, (b) annealed at 800°C and (c) annealed at 1200°C. The PL spectra were decomposed as two Gaussian shapes. Red lines are the fit curves, and the green lines are Gaussian components.

Peaks 1 and 2 for as-deposited samples are centered at about 420 and 520 nm, respectively, and they are ascribed to both Ce^{3+} and radiative oxide defects. Annealing

Table 7.1 Summary of the deconvolution results for Ce009, 010, 011 and 012.

Sample	Anneal Temp (°C)	Peak 1 (nm)	Width 1 (nm)	Intensity 1 (a.u.)	Peak 2 (nm)	Width 2 (nm)	Intensity 2 (a.u.)
Ce009	AD[1]	422	78	0.009	520	161	0.004
	800	438	75	0.032	556	168	0.015
	900	444	73	0.029	552	164	0.015
	1000	447	78	0.025	546	176	0.012
	1100	448	81	0.025	540	161	0.013
	1200	446	64	0.24	542	162	0.11
Ce010	AD	424	74	0.015	515	163	0.006
	800	437	79	0.044	550	191	0.024
	900	449	79	0.041	570	189	0.031
	1000	447	74	0.023	544	159	0.013
	1100	450	80	0.024	549	168	0.014
	1200	446	64	0.7	545	169	0.35
Ce011	AD	421	72	0.031	515	181	0.01
	800	442	77	0.093	554	181	0.055
	900	447	72	0.06	551	166	0.032
	1000	449	75	0.02	547	166	0.012
	1100	453	71	0.023	569	186	0.032
	1200	449	62	1.58	553	166	1.1
Ce012	AD	420	73	0.051	535	212	0.011
	800	443	73	0.125	544	160	0.063
	900	448	74	0.08	545	173	0.033
	1000	447	74	0.025	534	185	0.009
	1100	452	74	0.034	554	150	0.035
	1200	451	60	1.6	563	169	1.43

treatments result in about 20 and 35 nm red-shifts for peaks 1 and 2, respectively. These can be related to both the conversion from Ce^{4+} to Ce^{3+} and the reduction of radiative oxide defects. The peak separation between peak 1 and 2 (about 0.45-0.5 eV) is probably related to the splitting between $^2F_{5/2}$ and $^2F_{7/2}$ states (0.25-0.3 eV) of Ce^{3+}, while this

splitting is quite difficult to be discriminated at room temperature. The largely constant peak positions and the similarities in dependence of spectral width and peak intensity on Ce concentration and the annealing temperature suggest that peak 1 and 2 both originate from one luminescence center: Ce^{3+}. In addition, after spectral width reductions in the range of 9-20 nm were observed for peak 1 under annealing at 1200 °C. It reflects the major change of the Ce^{3+} environment which is related to the formation of cerium silicate. A more detailed discussion will be given later in this section in combination with the analysis of PL intensity results.

7.1.1.3 Effects of Annealing Temperature on PL Intensity

Figure 7.3 depicts the normalized integrated PL intensities in the 350-700 nm band for various samples as a function of the annealing temperature. The PL intensities have been normalized to a thickness of 1000 Á with the assumption that the PL intensity increases linearly with increasing film thickness, and this will be the case for all the PL intensity results discussed in this thesis. Plots for samples with low (0.01-0.07 at.%) and high (0.1-0.9 at.%) Ce concentrations are presented separately for clarity.

In most cases, the as-deposited samples exhibit the lowest PL intensities. The PL intensities vary with the annealing temperature in a similar trend: They increase with increasing annealing temperature up to 800 °C reaching a secondary peak, then decrease at higher temperatures until 1100 °C, followed by a sudden increase at 1200 °C to the

highest observed values. Generally, PL intensities increase with increasing Ce concentrations. The only exception is Ce030 which contains a higher Ce concentration than Ce029 but exhibits lower intensities for most of the annealing temperatures.

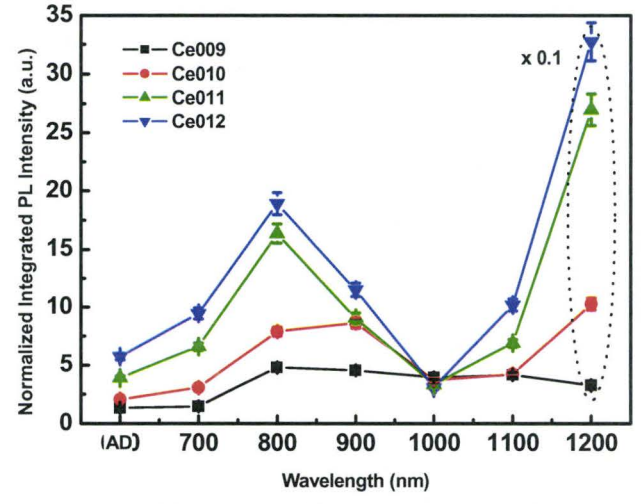

(a)

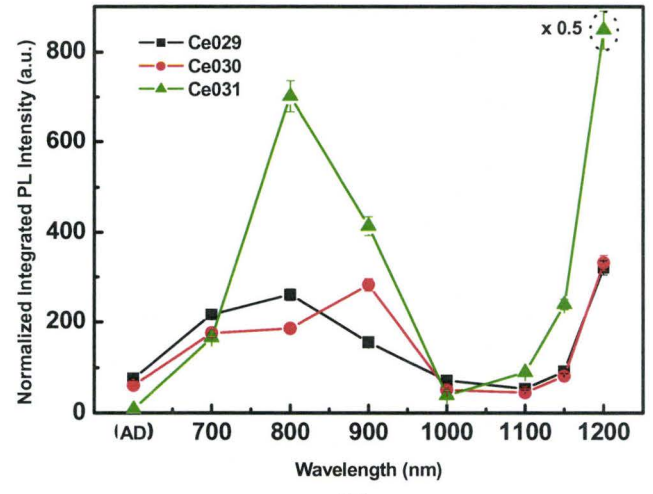

(b)

Figure 7.3 Integrated PL intensities in the range of 350-700 nm for the Ce:ORSO samples with various Ce concentrations as a function of annealing temperature. (a) Ce concentration from 0.01 to 0.07 at.%; (b) Ce concentration form 0.1 to 0.9 at.%.

Both Ce^{3+} and radiative oxide defects may contribute to the weak PL for the as-deposited sample. The films were deposited under oxygen rich conditions, and most of the Ce ions exist as quadrivalent. Thus, only very few optically active Ce^{3+} ions exist in the as-deposited films. At the same time, the non-equilibrium deposition process may introduce many defect precursors such as strained Si-O bonds and interstitial oxygen atoms which may give rise to various radiative and nonradiative oxide defects.

Under annealing at 700-800 °C, the significant increase of PL intensity is attributed to the conversion from Ce^{4+} to Ce^{3+} and the reduction of nonradiative oxide defects. Previous studies of CeO_2 showed [57] that at this temperature crystallized stoichiometric CeO_2 tends to form Ce_6O_{11} to lower the O/Ce ratio through migration of oxygen vacancies. It appears that Ce^{3+} ions are more thermodynamically stable than Ce^{4+} ions at this condition. Although N_2 is not a reducing gas, there is an oxygen concentration difference between the film and the surrounding environment. So, oxygen may release to the environment and result in a local oxygen deficiency in the film which can facilitate the deoxidization of Ce^{4+} ions.

The deconvolution results in this study support this argument. As noted previously, red shifts of two Gaussian components were observed from annealed samples. Malashkevich et al. [58] pointed out the presence of two types of Ce^{3+} sites: Ce^{3+} ions whose nearest surrounded ions are Ce^{4+} or Ce^{3+}. The former causes a shorter emission

wavelength than the latter. In this study, the Ce^{4+}-Ce^{3+} conversion during annealing leads to the situation that more Ce^{3+} ions are surrounded by Ce^{3+} instead of Ce^{4+}, and results in the red-shifts of the Gaussian components. On the other hand, the typical emission wavelength for WOB is 415 nm, its reduction during the annealing is also likely responsible for the observed red-shifts.

The decrease of PL intensity between 800 and 1000 °C can be explained by the precipitation of Ce^{3+} ions. One consequence of the progressive reduction of oxide defects during the annealing is the significant reduction of available NBOs which lodge Ce^{3+} ions. Thus at greater temperatures, more Ce^{3+} ions tend to precipitate to share the limited amount of NBOs. As a result, Ce^{3+} PL is quenched by ion-ion interaction. The quenching effects appear more evident in the samples with higher Ce concentrations which exhibit a more sharp decrease of PL intensity in this range.

At annealing temperatures higher than 1000 °C, both the abrupt increase of PL intensity and the reduction of the spectral width of the Gaussian components reveal the major change of the surrounding structures of Ce^{3+} ions. At this high temperature, SiO_2 network begins to re-organize, and Ce ions may acquire enough energy to interact with the surrounding Si and O to form a more stable structure. As noted previously, several groups have observed UV/blue light emission from CeO_x/SiO_x or Ce/Si films subjected to thermal treatment in inert or reducing ambients at temperatures higher than 1000 °C [57,

59, 60, 61, 62]. In all cases, the emission was assigned to the formation of new structures in the films, while the identification of the origin of the emission still remains controversial. In this study, the abrupt increase of the UV/blue emission intensity is assigned to the formation of cerium silicate in the films. The FTIR spectra and HR-TEM images which support the argument are presented in sections 7.3 and 7.4.

7.1.1.4 Effects of Annealing Duration on PL Intensity

Figure 7.4 depicts the normalized integrated PL intensity in the 350-700 nm band for various samples annealed at 800 and 1200 °C as a function of Ce concentration for three different annealing durations. Each coloured curve corresponds to a different annealing duration. The plots for samples with low and high Ce concentration are presented separately for clarity. For annealing at both 800 and 1200 °C, PL intensities generally increase with increasing Ce concentration regardless of different annealing durations (except for the 0.2 at.% Ce case). The severe quenching effects which were usually seen from similar films with high Ce concentration prepared through other methods were not observed here.

For annealing at 800 °C, maximum PL intensities were observed at 1 hour annealing for most of samples (except for the 0.1 and 0.2 at.% Ce cases). This implies that the conversion from Ce^{4+} to Ce^{3+} instead of reduction of oxide defects is mainly responsible for the increase of the PL intensity, since at this annealing temperature, oxide defects can

be reduced significantly in a very short time such as 5 minutes [91]. For 3 hour annealing, it is possible that the precipitation of Ce ions becomes dominant in its competition with Ce^{4+}- Ce^{3+} conversion and quenched Ce^{3+} PL.

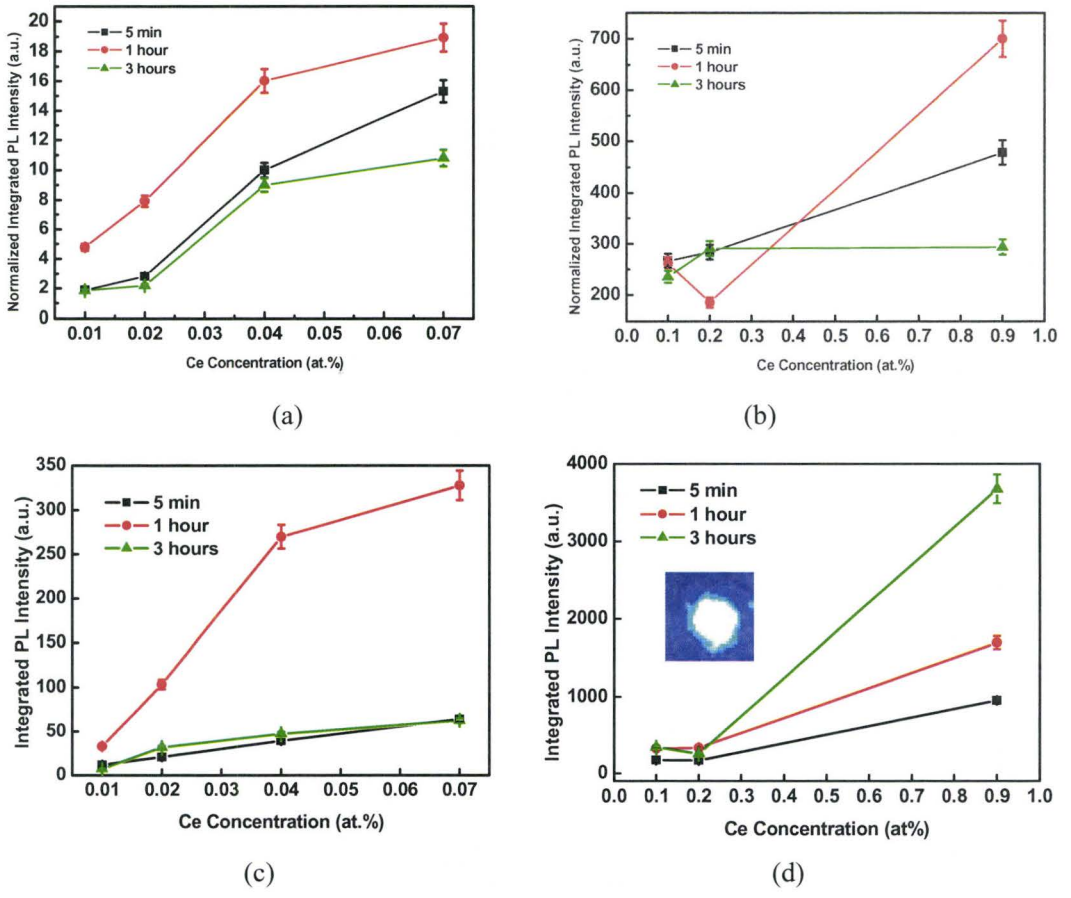

Figure 7.4 Integrated PL intensities in the 350-700 nm band for various Ce:ORSO samples as a function of Ce concentration. (a) low Ce concentration annealed at 800 °C (b) high Ce concentration annealed at 800 °C (c) low Ce concentration annealed at 1200 °C (d) high Ce concentration annealed at 1200 °C. The inset shows the image taken for the Ce031 under annealing in flowing N_2 at 1200 °C for 3 hours.

For the points corresponding to 0.1 and 0.2 at.% Ce concentration, the different

dependence of the PL intensity on the annealing duration is likely due to the inherent non-uniform distribution of Ce ions in the films during the deposition. In the as-deposited samples, some Ce ions have lower Ce-Ce spacing comparing with other ions. These Ce ions tend to precipitate in a shorter annealing time, since less diffusion is required. Consequently, PL intensities begin to decrease after 1 hour instead of 3 hour annealing. On the other hand, Ce^{4+}-Ce^{3+} conversion progressively occurs through the whole annealing duration. Therefore, the change of Ce^{3+} PL intensity is dependent on which process is dominant. This may explain why these two samples behave in a different way for 3 hour annealing.

At 1200 °C, for low Ce concentration samples the maximum Ce^{3+} PL intensity was observed for 1 hour annealing, while for high Ce concentration samples the PL intensity generally increases with increasing annealing duration. As mentioned previously, the formation of cerium silicate is mainly responsible for the increase of the PL intensity at 1200 °C. According to classical nucleation theory [102, 103] only when nuclei exceed a critical radius free energy will decrease and crystallization of cerium silicate may begin. To reach the critical radius size, Ce ions of certain numbers are required. Therefore a higher Ce concentration should lead to a greater possibility of forming nuclei due to the availability of more Ce ions. This may explain the different effects of annealing duration on Ce^{3+} PL intensity for different Ce concentration. There are two simultaneous processes

in competition: the precipitation of Ce ions and the formation of cerium silicate. At lower Ce concentration, the number and size of cerium silicate crystals is limited by the quantity of available Ce ions instead of annealing duration. Therefore a decrease of PL intensity for 3 hour annealing was observed due to the clustering of Ce ions. At higher Ce concentrations, the number and size of cerium silicate crystal is limited by the annealing duration (for the annealing durations discussed in this study), since once the nuclei reached critical size, crystal growth should occur continuously through the annealing duration. As a result, the increase of Ce^{3+} PL intensity with increasing annealing duration was observed.

7.1.2 Silicon-rich Films

Subsection of Table 6.1

Sample	Absolute Atomic Areal Density [x10^7 atoms/ cm^2]				Si [at.%]	RE [at.%]	Thickness [Å]		Index of Refraction
	Si	O	RE	Ar			RBS	Optical	
Ce003	2.53	3.76	0.002	0.004	40.16	0.04	950	970	1.70

Figure 7.5 shows the PL spectra for a Ce-doped silicon-rich silicon oxide (Ce:SRSO) film, Ce003, as deposited and annealed in flowing N_2 for 1 hour at various temperatures. There is no appreciable emission from the sample as deposited. The sample annealed at 800 °C shows a broad emission band in the range 600-1000 nm. Its PL intensity increases with increasing annealing temperature until reaching a maximum at 1100 °C. When

annealed at 1200 °C, the 600-1000 nm band decreases significantly, at the same time another weak broad band in the range 400-600 nm emerges.

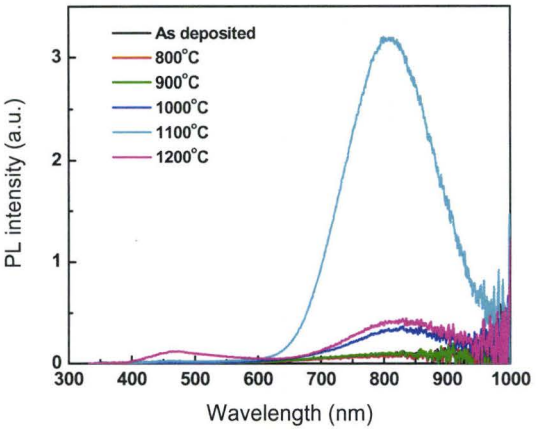

Figure 7.5 PL spectra of Ce003, as deposited an annealed in flowing N_2 for 1 hour at various temperatures.

It is possible that the 600-1000 band originates from Si-ncs, while the 400-600 nm band is related to Ce^{3+} ions present in the film. The enhancement of Si-ncs PL intensity with increasing annealing temperature indicates the formation of more Si-ncs. The quenching of Ce^{3+} PL at annealing temperatures lower than 1200 °C is possibly due to the competition between Si-ncs and Ce ions on the absorption of excitation photons. The simultaneous quenching of Si-ncs PL and enhancement of RE-related PL is usually considered as the evidence for the coupling between Si-ncs and RE ions and implies the existence of the indirect excitation processes. In this study, it appears that the indirect excitation of Ce^{3+} PL is much less efficient than direct excitation, since Ce:ORSO of

similar Ce concentration (Ce011) subjected to the same annealing treatment exhibits 10 times stronger PL in a similar wavelength range.

7.3 Evolution of Microstructure with Nitrogen Annealing

7.3.1 FTIR Results

Figure 7.6 depicts the representative FTIR spectra for Ce012, as deposited and annealed in flowing N_2 for various temperatures and annealing durations. The absorbance spectrum for the as-deposited sample is similar to that of high quality thermally grown silicon oxide. The three main peaks are centered at 460, 800 and 1080 cm^{-1} which correspond to Si-O-Si rocking vibration, symmetric Si-O-Si stretching and anti-symmetric Si-O-Si stretching bonds. In addition, a weak broad band in the range 1350-1800 cm^{-1} is observed. It may originate from O-H bonds from water captured from the air ambient, since it can be almost eliminated after purging in N_2 for 12 hours.

When annealed at 800 or 1200 ^{o}C, the peak positions remain the same, while decreases of the peak widths and increases of the peak intensities were observed for 1200 ^{o}C, which suggest the enhancement of film uniformity and the crystallization of silicon oxide network at this temperature.

Samples as deposited or annealed at 1200 ^{o}C for 1 hour have similar transmittance

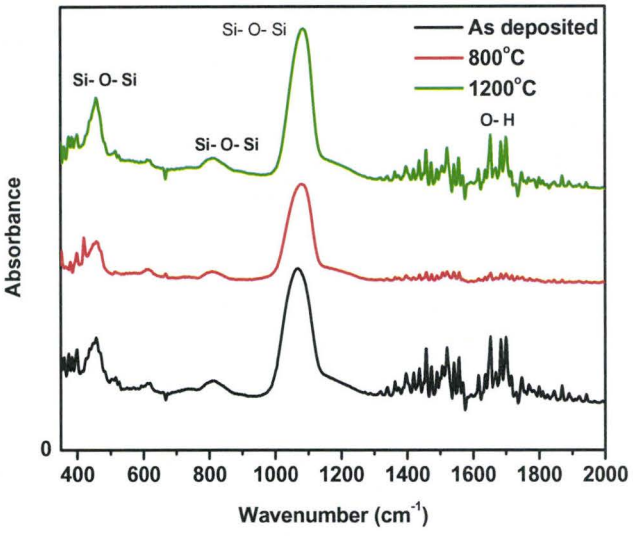

(a)

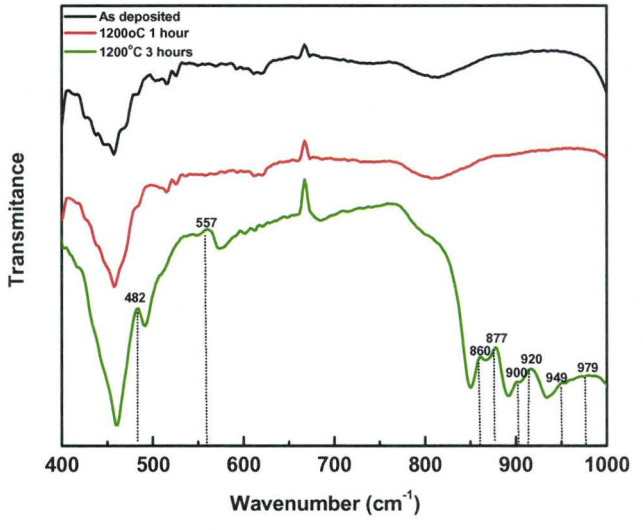

(b)

Figure 7.6 FTIR spectra for Ce012, as deposited and annealed in flowing N_2 for various temperatures and annealing durations. (a) absorbance spectra for Ce012, as deposited and annealed at 800 and 1200 ^{o}C for 1 hour, (b) transmittance spectra for Ce012, as deposited and annealed at 1200 ^{o}C for 1 and 3 hours

spectra, while annealing at 1200 ^{o}C for 3 hours resulted in a number of new sharp bands

emerging at 482, 557, 860, 877, 900, 920, 949 and 979 cm^{-1} which have similar positions as some of the peaks observed from $Ce_2Si_2O_7$ [61, 62]. However, there are still differences in both numbers and positions between them. FTIR spectra for Ce009, 010 and 011 all exhibited similar peaks and dependences on annealing conditions as those of Ce012, while no new sharp bands were observed for 3 hour annealing at 1200 °C. (data not shown). This could be due to the very low Ce concentrations in these films.

7.3.2 HR –TEM Results

Figure 7.7 shows a HR-TEM image of Ce031 annealed in flowing N_2 at 1200 °C for 1 hour. The image shows three distinct layers from right to left, which correspond to substrate, film and glue layers, respectively. The interface between the film and the glue appears zigzag, and there are many worm shape grey strips containing black particles.

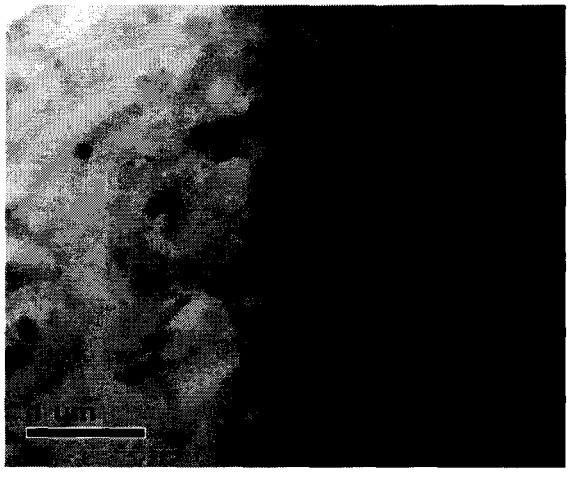

Figure 7.7 A HR-TEM image of Ce031 annealed in flowing N_2 at 1200 °C for 1 hour.

Figure 7.8 shows the XEDS spot analysis results for four selected spots located in the film, worm shape stripe, glue layer and dark particle, respectively. The presence of Ce was only observed from the dark particle. Although the possible presence of Ce element in the three other spots can not be completely excluded due to the sensitivity limit of the instrument, the corresponding concentration should be much lower than that of the dark particle.

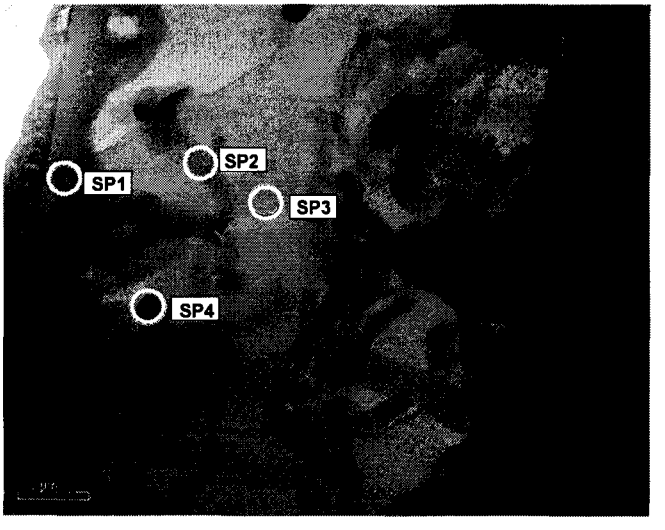

(a)

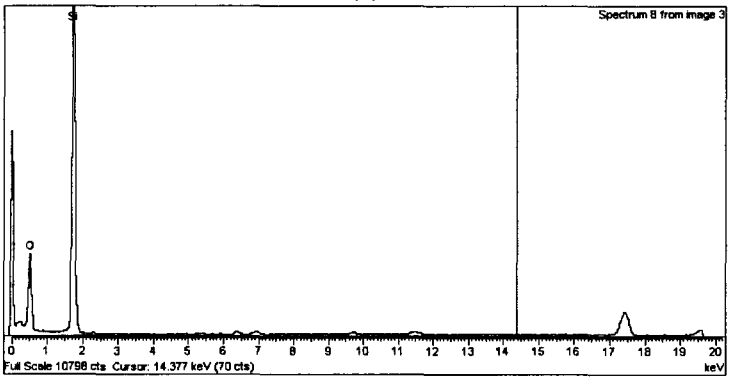

(b)

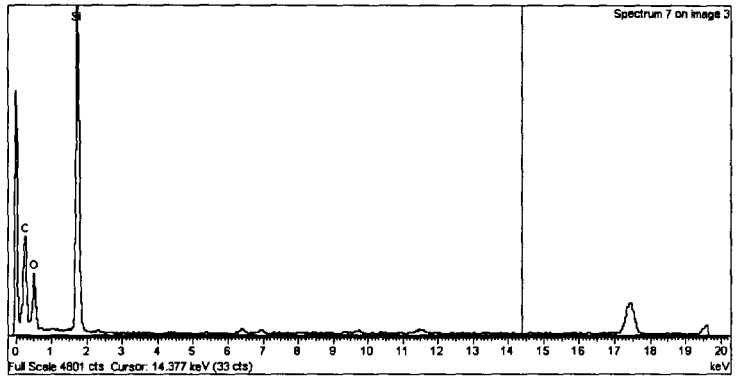

(c)

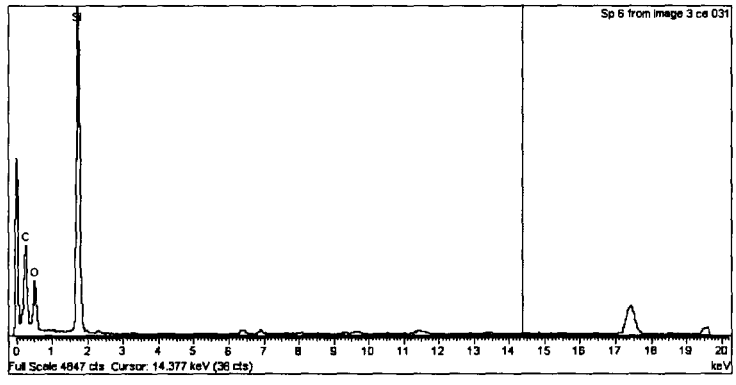

(d)

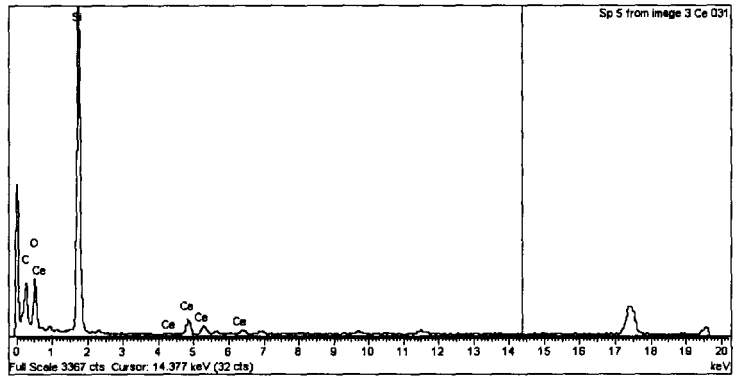

(e)

Figure 7.8 XEDS elemental spot analysis for four selected spots. (a) the locations of selected spots; (b) the elemental analysis of spot 1; (c) spot 2 ;(d) spot 3; (e) spot 4

Figure 7.9 shows the XEDS elemental line-scan across the interface between the film and the substrate for Si, O and Ce. A slight diffusion of O atoms from the film to the substrate was observed. The diffusion length is as little as 5 nm due to the rigid bond structures of silicon oxide and the silicon substrate. Ce was found accumulated near the interface. The observed dark grey line near the interface in Figure 7.9 (a) corresponds to the Ce enrichment layer according to the line-scan spectrum. The broken area of the Ce enrichment layer resulted from the bombardment of electrons in the line-scan process.

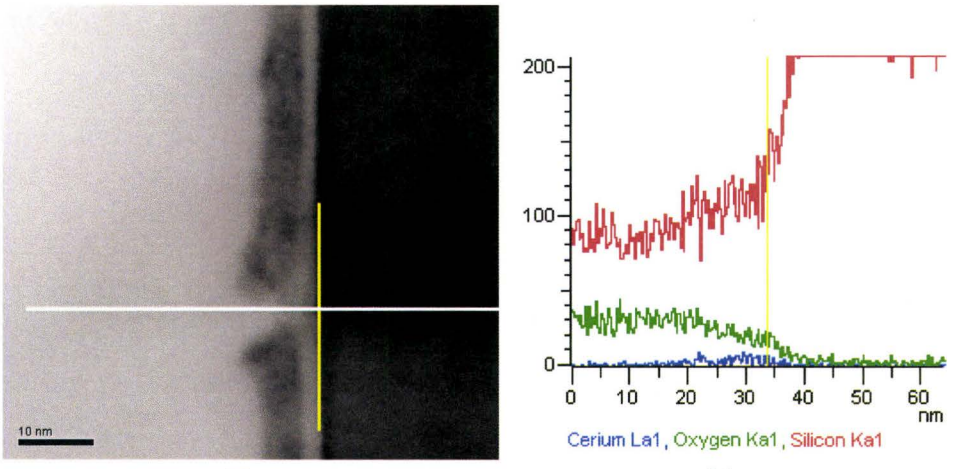

(a) (b)

Figure 7.9 XEDS elemental line-scan analysis. (a) the TEM image containing the line-scan location. The white and yellow lines indicate the line-scan distance and the visual interface between the film and the substrate, respectively, (b) the elemental line-scan profiles for Si, O and Ce

The as-deposited sample exhibits a relatively uniform distribution of Ce through the whole thickness (see Figure 4.2, p.44), while annealing at 1200 ^{o}C caused an

accumulation of Ce near the interface between the film and substrate. It appears that Ce also accumulated near the film surface, and the interface stresses between the Ce abundant and deficient layers caused the delamination of the films. The delaminated layers were separated and pushed into the glue layer during the TEM sample preparation process, and formed the dispersed grey "worms" and dark particles.

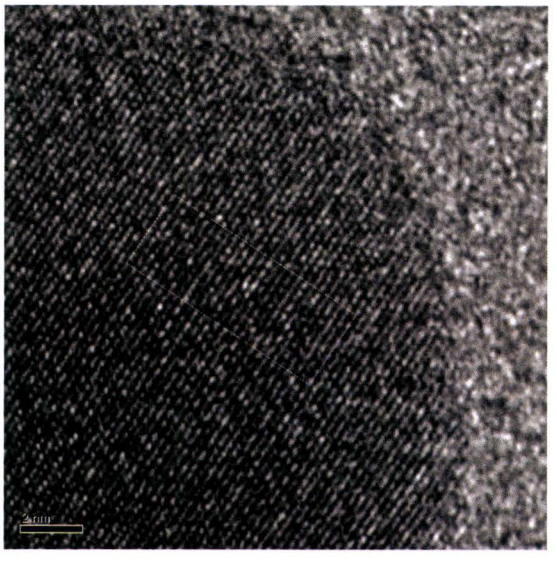

(a)

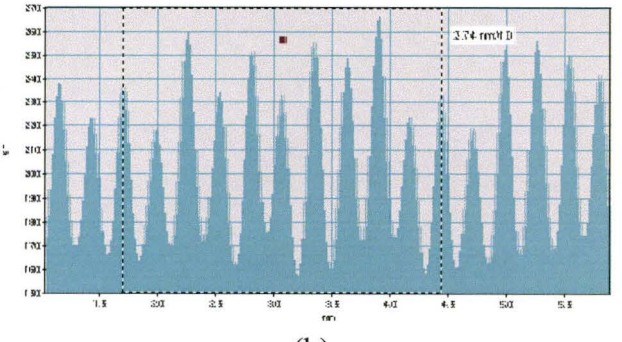

(b)

Figure 7.10 A HR-TEM lattice image of a Ce-containing particle. (a) the lattice image (b) the lattice profile

Figure 7.10 shows a HR-TEM lattice image of a black particle containing Ce. The crystalline structure is clearly visible with a lattice spacing of 0.274 nm as indicated by the lattice profile. This lattice spacing is comparable to that of cerium silicates [59, 60] and provides direct evidence for the formation of cerium silicate. There are a total of six types of cerium silicate crystallites that may form under atmospheric pressure, depending on the Ce:Si:O composition ratio including: Ce_2SiO_5, $Ce_{9.33}(SiO_4)O_2$, $Ce_2Si_2O_7$, $CeSiO_4$ and two additional silicates reported recently [61]. $CeSiO_4$ is the only cerium silicate containing Ce^{4+} which is optically inactive. Therefore, the crystallites observed in this study possibly correspond to one of the other five structures. The lattice parameters for these cerium silicate crystalline structures are quite close and cannot be used for discrimination, while the specific crystalline phase is possibly identified in conjunction with X-ray diffraction analysis (XRD).

7.4 Evolution of PL with Hydrogenation Annealing

The PL spectra and microstructure evolutions for Ce:ORSO samples under annealing in flowing N_2 have been comprehensively investigated in the previous sections. In this section, the effects of annealing in Ar +5% H_2 ambient on PL evolution for four low Ce concentration samples are studied.

Figure 7.11 depicts the representative PL spectra for Ce012, as deposited and annealed in flowing Ar + 5% H_2 at various temperatures for 1hour. The PL spectra

resemble these of Ce012 annealed in flowing N_2 with some differences in spectral shape and peak positions.

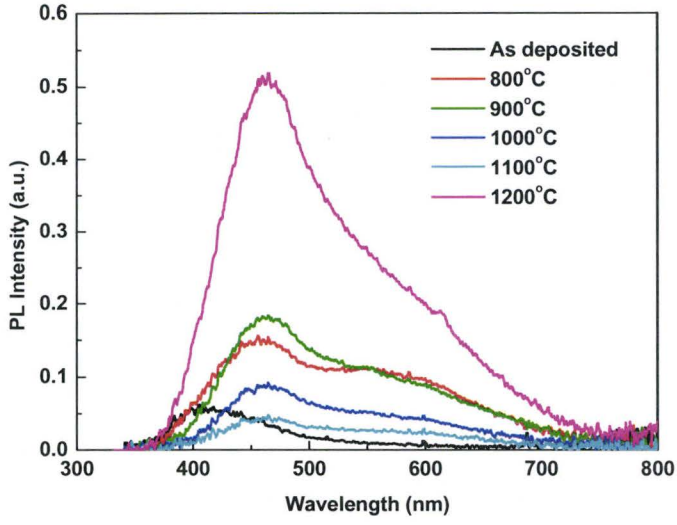

Figure 7.11 PL spectra for Ce012, as deposited and annealed in flowing Ar + 5% H_2 at various temperatures for 1 hour.

Figure 7.12 shows the normalized integrated PL intensities in the 350-700 nm band for various samples annealed in flowing Ar + 5% H_2 for 1 hour as a function of the annealing temperature. The corresponding data for annealing in N_2 is also given and connected by dotted lines for comparison. In general, similar dependencies of the PL intensity with the annealing temperature were observed for both annealing ambients regardless of different Ce concentrations. In comparison with N_2 annealing, hydrogenation annealing results in enhanced PL intensities for temperatures below 1200

°C and reduced PL intensities at 1200 °C.

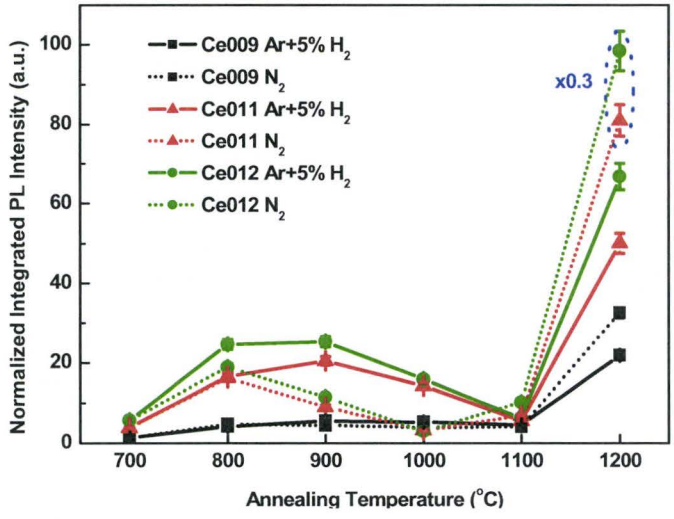

Figure 7.12 Integrated PL intensities in the range 350-700nm for four Ce:ORSO samples annealed in flowing N_2 and Ar + 5% H_2 for 1 hour as a function of the annealing temperature.

As noted previously, the enhancement of the Ce^{3+} PL intensity at 800 °C is related to the Ce^{4+}-Ce^{3+} conversion and the reduction of oxide defects. The hydrogenation annealing is likely to improve Ce^{3+} PL by facilitating both processes. The studies by Estreicher et al. [104] showed that at high annealing temperatures the migration energy for interstitial oxygen in Si can be reduced significantly (2-3 times) in the presence of hydrogen. In addition, the simultaneous motion of hydrogen with oxygen can improve the diffusivity of interstitial oxygen even further. This process may facilitate the Ce^{4+}-Ce^{3+} conversion through more efficient removal of oxygen from the film. On the other hand, it has been

extensively reported that hydrogenation annealing is capable of passivating various oxide defects in the films [105, 106, 107]. Therefore, more efficient passivation of oxide defects coupled to Ce^{3+} can be expected.

The reason for less enhancement of the PL intensity for hydrogenation annealing at 1200 °C remains unclear. It is likely that the presence of hydrogen affects the cerium silicate formation process or even the cerium silicate type. HR-TEM and XRD analysis should be conducted in the future to elucidate the actual process.

The most intense Ce^{3+} PL comes from Ce031 under annealing in flowing N_2 at 1200 °C for 3 hours. Actually, Ce029, 030 and 031 under annealing in flowing N_2 at 800 or 1200 °C for 1 or 3 hours all exhibit such strong emission that it can be easily observed under very bright room lighting conditions. Considering the fact that the excitation power is as low as 17 mW, the emission intensities are quite outstanding. The emission picture for Ce031 under annealing in N_2 for 1 hour at 1200°C anneal is shown in the inset of Figure 7.4 (d) on p.74.

Chapter 8

Studies of Eu-doped Silicon-rich Silicon Oxides

8.1 Evolution of PL with Nitrogen Annealing

Sub-section of Table 6.1

Sample	Absolute Atomic Areal Density [x10^7 atoms/ cm^2]				Si [at.%]	RE [at.%]	Thickness [Å]		Index of Refraction
	Si	O	RE	Ar			RBS	Optical	
Eu020	2.26	4.07	0	0.04	34.78	0.02	974	975	1.59
Eu021	2.14	4.06	0.008	0.02	34.48	0.12	940	946	1.59
Eu022	2.58	4.76	0.185	0.026	35.16	2.15	1350	1270	1.58

The PL evolution with N_2 annealing for three Eu: SRSO samples, Eu020, 021 and 022, has been investigated. To illustrate the structural features of the PL spectra for Eu:SRSO samples, the representative PL spectra for Eu021, as deposited and annealed in flowing N_2 at various temperatures for 1 hour are depicted in Figure 8.1. A series of broad emission bands in the range 400-800 nm with various peak positions and intensities were observed for various annealing temperatures.

The unsymmetric appearances of these emission bands imply the presence of

multiple luminescence centers. To distinguish these luminescence centers, Gaussian deconvolutions for all the PL spectra were attempted. Excellent fits were obtained for most of the PL spectra. However, a perfect fit for the PL spectra of Eu020, annealed at 900 to 1100 °C, cannot be achieved due to their low signal intensities and very low signal to noise ratios.

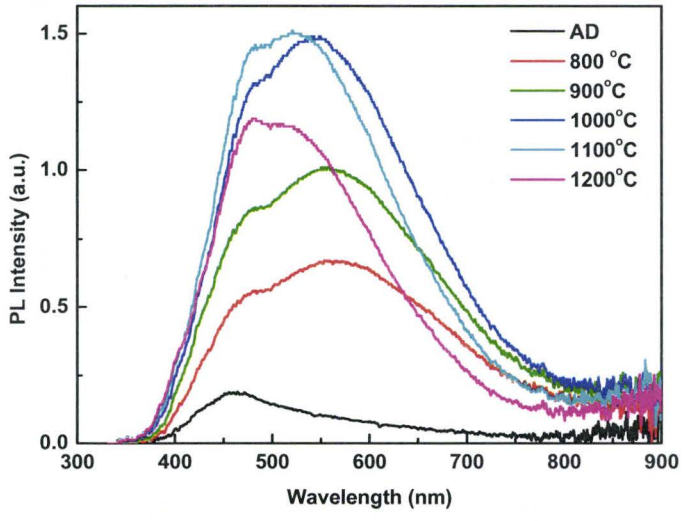

Figure 8.1 Representative PL spectra for Eu021, as deposited and annealed in flowing N_2 at various temperatures for 1 hour.

Figure 8.2 depicts the representative Gaussian fit for Eu021 annealed at 1000 °C. It is interesting to note that all the successfully decomposed PL spectra show three resembling components. A summary of the peak positions, spectral widths (full wavelength at half maximum) and peak intensities for the respective components is given in Table 8.1. The

peak positions of components 1, 2 and 3 are located in the ranges 442-486, 521-568 and 605-687 nm, respectively, and their intensities are comparable to each other. The fluctuation of their spectral widths is small regardless of the different annealing temperatures. Both these features imply that the three components originate from certain luminescence centers. The possible luminescence centers in the films are Eu^{2+}, Eu^{3+}, Si-ncs and radiative oxide defects.

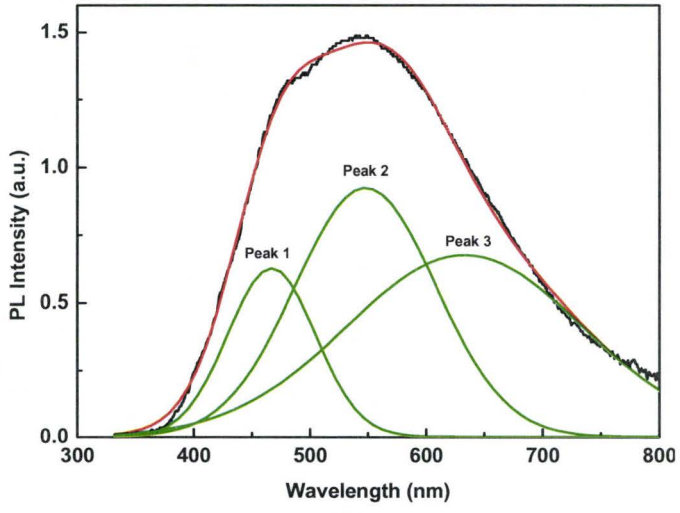

Figure 8.2 Gaussian deconvolution of a representative PL spectrum, Eu021 annealed in flowing N_2 for 1hour at 1000 ^{o}C.

As noted previously, the 5d-4f transition of Eu^{2+} usually corresponds to broad band emission in the range 400-600 nm, and the splitting of 4 $f^6 5d^1$ state gives rise to two separated peaks [66]. On the other hand, at least three types of radiative oxide defects are

Table 8.1 Summary of the deconvolution results for Eu:SRSO samples as deposited and annealed in flowing N_2 for 1hour at various temperatures.

Sample	Anneal Temp (°C)	Peak 1 (nm)	Width 1 (nm)	Height 1 (a.u.)	Peak 2 (nm)	Width 2 (nm)	Height 2 (a.u.)	Peak 3 (nm)	Width 3 (nm)	Height 3 (a.u.)
Eu020	AD	453	82	0.07	556	139	0.11	660	238	0.05
	800	442	83	0.03	529	124	0.02	651	187	0.03
	1200	469	71	0.03	558	184	0.01			
Eu021	AD	454	65	0.13	521	108	0.07	625	226	0.05
	800	458	67	0.25	547	129	0.40	645	213	0.39
	900	458	68	0.39	547	134	0.71	654	203	0.48
	1000	467	76	0.63	547	121	0.921	633	203	0.68
	1100	470	79	0.90	550	99	0.76	609	196	0.66
	1200	470	85	0.82	552	96	0.54	605	199	0.44
Eu022	AD	486	71	0.06	583	131	0.27	647	213	0.39
	800	470	81	0.17	568	153	0.74	687	218	0.40
	900	466	78	0.13	566	154	0.50	679	216	0.35
	1000	471	81	0.29	556	143	0.76	665	206	0.38
	1100	467	81	0.51	549	135	0.88	656	202	0.37
	1200	462	79	0.62	542	120	0.72	625	203	0.45

expected from SRSO including divalent Si, the neutral oxygen vacancy (NOV) and the E_δ' center whose typical emission wavelengths are 285, 450-470 and 520-550 nm, respectively. The formation of these defects is related to the large number of oxygen vacancies and dangling Si bonds existing in SRSO [98, 99, 100]. One would expect a large quantity of oxide defects from as-deposited samples. Therefore, NOV and the E_δ' center are probably responsible for peaks 1 and 2 of the as-deposited samples. They may, however, also contribute to peaks 1 and 2 for annealed samples, while the dominant luminescence centre should be Eu^{2+}, since oxide defects are expected to be significantly

reduced through annealing.

Although the range of 605-687 nm is considered as characteristic wavelength of Eu^{3+} luminescence [68], Eu^{3+} luminescence usually exhibits several distinct narrow bands, and their PL intensity should not be comparable to that of Eu^{2+} because of its very low oscillator strength of the partially allowed transition. On the other hand, the typical PL emission wavelength of Si-ncs is comparable to that of peak 3. The red-shifts of peak 3 observed from both Eu021 and 022 under annealing at 800 °C are characteristic for Si-ncs PL and. therefore, peak 3 is mostly likely attributable to Si-ncs.

To study the effects of annealing on different luminescence centers, the normalized integrated PL intensities for Eu^{2+} PL and Si-ncs PL as a function of the annealing temperature is plotted in Figure 8.3. In all cases, annealing at 800 °C enhances the PL significantly compared with the as-deposited samples. For Eu021, both the Eu^{2+} and Si-ncs PL increase with increasing annealing temperatures up to a maximum at 1000 °C, and then decrease at greater temperatures. For Eu022, there is no evident correlation between Eu^{2+} PL and the annealing temperature, while the Si-ncs PL exhibits the dependence comparable to that of Eu021, with the maximum PL occurring at 1100 °C.

Eu ions exist as trivalent ions in the $Eu(tmhd)_3$ precursor source and were incorporated into the film in an oxygen rich environment. Therefore, most of the Eu ions existed as Eu^{3+} in the as-deposited samples and give rise to a very low Eu^{2+} PL. And

observed PL is mainly attributed to radiative oxide defects. When annealed in N_2 from 800 to 1000 °C, Eu^{3+} were reduced to Eu^{2+} progressively. At the same time, oxide defects should reduce. These two processes both lead to the increase of Eu^{2+} PL for Eu021. At greater temperature, Eu^{2+} ions began to precipitate and its PL was quenched through ion-ion interactions.

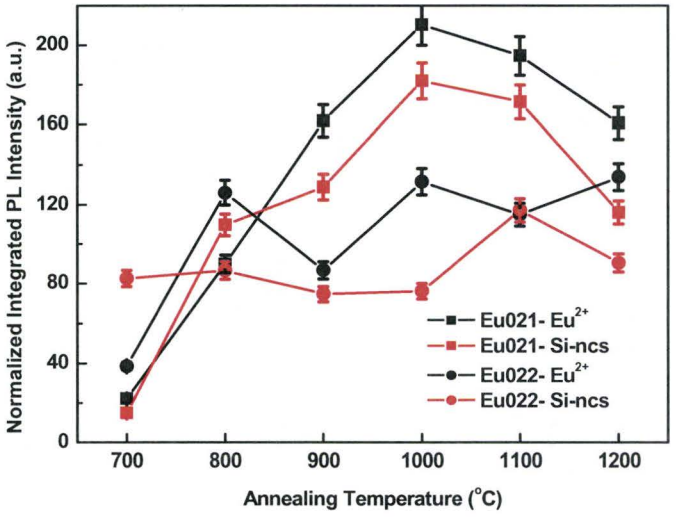

Figure 8.3 Integrated PL intensity for Eu^{2+} and Si-ncs components from Eu021 and 022 as a function of the annealing temperature.

The increase of the Si-ncs PL with increasing annealing temperature reveals the formation of more Si-ncs, while its decrease at 1100 and 1200 °C is likely attributed to the coupling between Si-ncs and Eu ions. A blue shift of the Si-ncs was observed for temperatures higher than 1000 °C. As noted previously, the peak position of the Si-ncs PL

was determined by both, the Si-ncs size and their oxygen-related surface states. Previous work by Iacona et al. showed that Si-ncs sizes tend to increase at higher temperatures due to the Ostwald ripening process [108]. Therefore, the blue shift of the Si-ncs PL peak may imply changes of the Si=O bonding structure at the Si-ncs surface caused by the presence of Eu^{2+}.

Considering the correlation between two luminescence centers, Eu^{2+} and Si-ncs, which both can be excited directly at 325 nm, and the fact that Si-ncs PL intensity is only 10% of that of SRSO without doping, there might be energy transfer between Si-ncs and Eu^{2+}. However, to examine the specific effects of the presence of Si-ncs on Eu^{2+} PL, a study on samples containing no excess Si is necessary in the future.

The odd Eu^{2+} PL dependence for Eu022 on the annealing temperature can not be fully resolved without further film structure characterization, but it is possibly related to the non-uniform distribution of a high concentration of Eu ions (2.15 at.%) in the film. Actually, the annealing treatments gave rise to a very rough surface morphology of Eu022. During the deposition, all other parameters were kept the same and only the Eu cell temperature was increased to achieve greater Eu incorporation through increasing Eu precursor vapor pressure in the reaction chamber. It is likely in the case of Eu022, the precursor molecules were too many to be efficiently cracked before streaming down to the film surface. At very high deposition rates (over 100 Å/ minute), large $Eu(tmhd)_3$

precursor molecules or their fragments stay in the film and are not uniformly distributed. Those volatile molecules tend to leave the film during the annealing, while their non-uniform distribution leads to the different densification rates of the different areas in the film and cause the observed rough surface morphology. The non-uniform distribution of Eu ions and film thickness may lead to the very different Eu^{2+} PL properties for different spots on the film and result in the as yet unexplainable Eu^{2+} PL dependence on the annealing temperature. In addition, it may also aggravate the precipitation of Eu ions and cause the quenching of Eu^{2+} PL. As a result, compared with Eu021, which has a low Eu concentration (0.12 at.%), Eu022 exhibits weaker Eu^{2+} PL for most annealing temperatures.

8.2 Evolution of PL with Hydrogenation Annealing

The evolution of the PL with hydrogenation annealing for Eu020, 021 and 022 has also been investigated. Figure 8.4 depicts the representative PL spectra of Eu 021 annealed in flowing Ar+5% H_2 for 1 hour at various temperatures. The PL line-shapes are quite different in comparison with those of N_2 annealing. For all annealing temperatures, a main peak centered at 450 nm with a long tail extending to 800 nm was observed. The Gaussian deconvolutions for all the PL spectra were attempted and excellent fits were obtained for the PL spectra from Eu020 and 021. The very low PL signal intensities from Eu022 lead to a low signal to noise ratio and a consequent failure of the deconvolution.

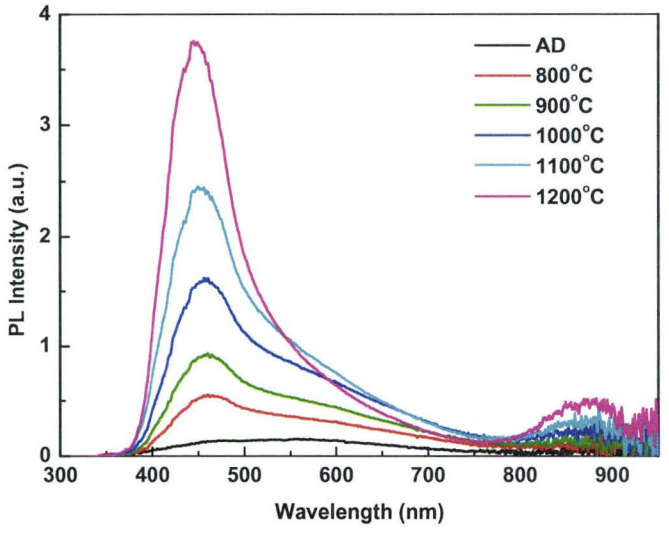

Figure 8.4 PL spectra for Eu021 as deposited and annealed in flowing Ar + 5% H_2 at various temperatures for 1hour.

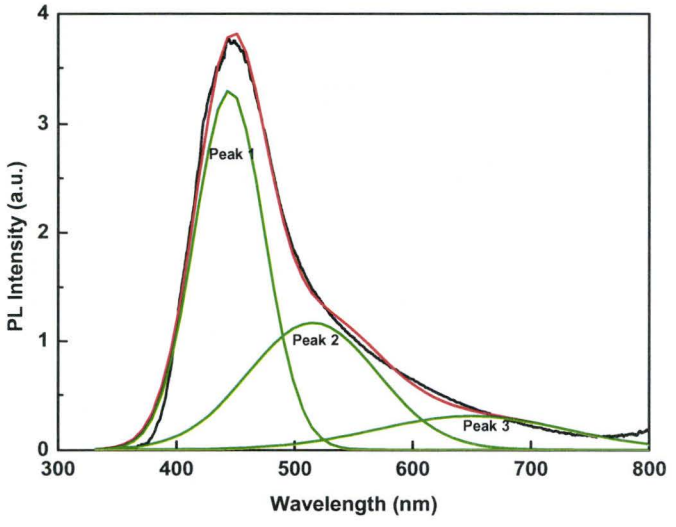

Figure 8.5 Gaussian deconvolution of representative PL spectra for Eu021annealed in flowing Ar + 5% H_2 at 1200 ^{o}C for 1 hour.

Figure 8.5 depicts a representative Gaussian fit for Eu021 annealed at 1200 ^{o}C. All

the successfully decomposed PL spectra also show three components. A summary of the peak positions, spectral widths and peak intensities for all the components is given in Table 8.2. In comparison with Table 8.1, it is clear that peak 1 and 2 correspond to the $4f^6 5d^1$-$4f^7$ Eu^{2+} PL, and peak 3 corresponds to the Si-ncs PL.

Table 8.2 Summary of the deconvolution results for Eu:SRSO samples as deposited and annealed in flowing Ar + 5%H_2 at various temperatures for 1 hour.

Sample	Anneal Temp (°C)	Peak 1 (nm)	Width 1 (nm)	Height 1 (a.u.)	Peak 2 (nm)	Width 2 (nm)	Height 2 (a.u.)	Peak 3 (nm)	Width 3 (nm)	Height 3 (a.u.)
Eu020	800	452	80	0.51	537	128	0.47	642	210	0.31
	900	458	81	0.65	546	132	0.77	652	198	0.35
	1000	453	82	0.75	539	125	0.78	632	213	0.55
	1100	456	79	1.00	536	120	0.92	626	202	0.47
	1200	457	76	0.92	532	116	0.83	611	201	0.49
Eu021	800	454	63	0.39	525	115	0.23	633	205	0.21
	900	452	62	0.69	523	111	0.35	625	200	0.30
	1000	450	61	1.24	519	107	0.59	619	194	0.46
	1100	447	61	1.96	514	107	0.85	615	189	0.49
	1200	445	59	3.30	515	108	1.17	650	158	0.31

Figure 8.6 shows the integrated PL intensity for Eu^{2+} and Si-ncs related components of Eu020 and Eu021 as a function of the annealing temperature. In comparison with N_2 annealing, for Eu020 it is obvious that hydrogenation annealing results in an enhancement of both the Eu^{2+} and Si-ncs PL. On the other hand, for Eu021 and 022 the Eu^{2+} and Si-ncs PL are significantly reduced at most of annealing temperatures. The Eu^{2+} PL for Eu 020

and Si-ncs PL for both Eu020 and 021 exhibit similar dependencies on the annealing temperature, which resemble those of Eu021 under N_2 annealing, while the Eu^{2+} PL for Eu021 increases monotonically with increasing annealing temperature.

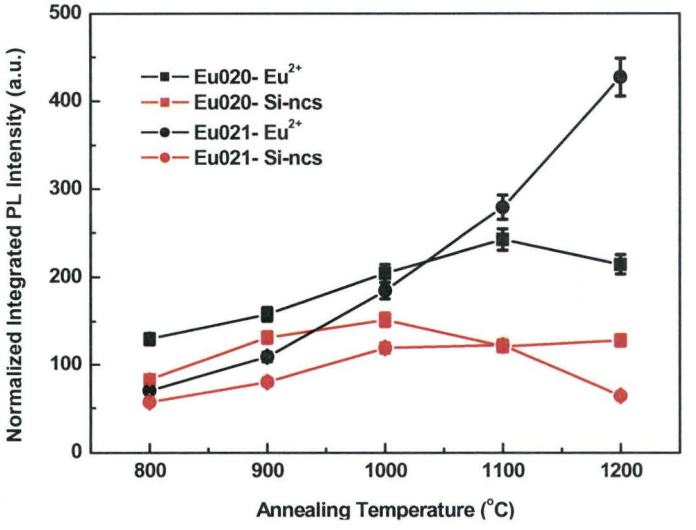

Figure 8.6 Integrated PL intensity of Eu^{2+} and Si-ncs components for Eu020 and 021 annealed in Ar + 5%H_2 for 1 hour as a function of the annealing temperature.

In comparison with N_2 annealing, hydrogenation annealing may simultaneously exert three influences on the film: more efficient reduction from Eu^{3+} to Eu^{2+}, passivation of various oxide defects and diffusion of Eu ions toward Si-ncs. The first two influences are expected to enhance the Eu^{2+} and Si-ncs PL regardless of the different Eu concentrations. In a previous study of hydrogenation effects on Er-doped amorphous silicon quantum dot materials by Park et al. [109], it was suggested that hydrogenation can cause the diffusion

of Er to Si-ncs. A similar process possibly occurs here. This "directional" diffusion of Eu ions may lead to the clustering of Eu ions on the Si-ncs surface for high Eu concentrations. At the same time, this diffusion may cause the coupling between Eu and Si-ncs. Although the details of this coupling remain unclear, the Si-ncs PL is usually quenched by nonradiative energy transfer to RE ions in the vicinity. Therefore, the directional diffusion is likely responsible for the Eu^{2+} and Si-ncs PL quenching observed from Eu021 and Eu022.

At annealing temperatures higher than 1000 °C, Eu022 exhibits a stronger Eu^{2+} PL relative to that of N_2 annealing. At the same time, a blue shift of peak 1 was also observed. As noted previously, multiphase europium silicate can form at 1000-1100 °C in inert or reducing ambients. Therefore, these phenomena may imply the formation of europium silicate in the film. To prove this argument, further studies of the film structure clearly are necessary.

In this study, the most intensive Eu^{2+} PL from Eu:SRSO was observed from Eu021 under annealing in Ar+5% H_2 at 1200 °C.

Chapter 9

Studies of Tb-doped Silicon Oxides

9.1 Evolution of PL with Nitrogen Annealing

9.1.1 Oxygen-rich Films

Sub-section of Table 6.1

Sample	Absolute Atomic Areal Density [x10^7 atoms/ cm^2]				Si [at.%]	RE [at.%]	Thickness [Å]		Index of Refraction
	Si	O	RE	Ar			RBS	Optical	
Tb015	2.13	4.59	0.0517	0.083	31.75	0.75	1060	1059	1.50
Tb016	1.88	4.17	0.0256	0.072	31.25	0.42	922	920	1.49
Tb017	2.14	4.6	0.0248	0.043	31.75	0.36	1020	1018	1.50

Tb016 and 017 have been selected to illustrate the structural features of PL spectra for various Tb:ORSO samples. The PL spectra for Tb015 resemble those of Tb016. Figure 9.1 (a) depicts the PL spectra of Tb016, as deposited and annealed in flowing N_2 at various temperatures for 1hour. Four strong distinct sharp bands were observed sitting on a weak broad band in the range 400-700 nm for all annealing temperatures. The spectral shape and peak positions of the four sharp bands are quite characteristic of Tb^{3+} PL and resemble those of Tb doped SiO_2 achieved by conventional PECVD [82].

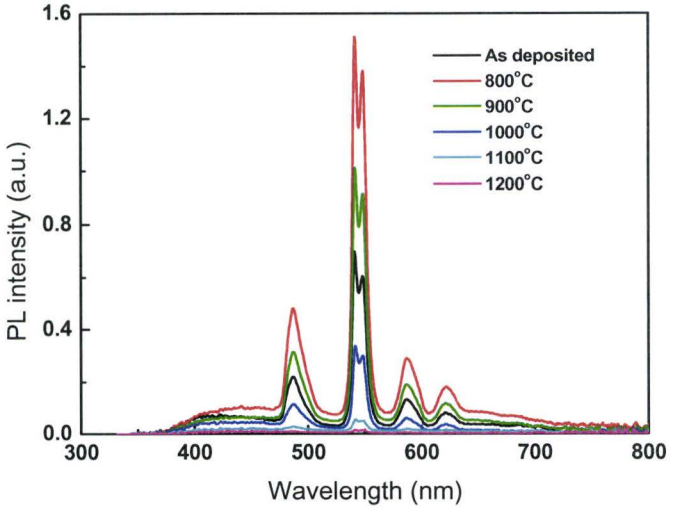

(a)

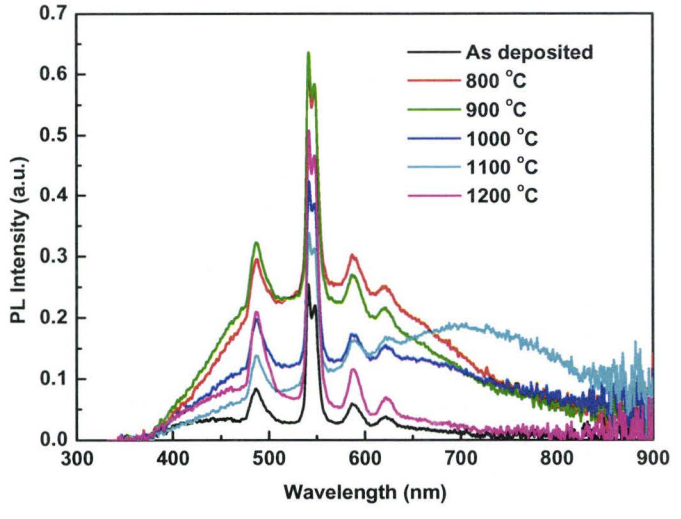

(b)

Figure 9.1 Representative PL spectra of two samples as deposited and annealed in flowing N_2 at various temperatures for 1hour. (a) Tb016, (b) Tb017

According to the energy level diagram of Tb^{3+} ions (see Figure 2.5, p. 25) , the four peaks centered at 487, 546, 588 and 620 nm are related to $^5D_4$-^7F_j (j=6,5,4,3) 4f-4f transitions of Tb^{3+}, respectively. The spectral widths of the four peaks are as narrow as 10

nm, which is indicative of a relatively symmetric surrounding matrix. The 546 nm peak splits into two peaks at 542 and 548 nm due to the Stark splitting [14]. Emissions from the $^5D_3$ state are absent due to the cross-relaxation effect [79]. There are no appreciable changes of peak positions and spectral widths for different annealing temperatures.

A weak broad band ranging from 400 to 700 nm was observed for all annealing temperatures. A similar emission band has often been assigned to radiative oxide defects in silicon oxide whose PL intensity should decrease when annealed at 800 ^oC [110]. In our case, however, the corresponding PL intensity becomes greater when annealed at 800^oC. In addition, it increases with increasing Tb^{3+} PL intensity. It is likely that the radiative oxide defects emitted light through nonradiative coupling to some optically active Tb^{3+} sites. More intensive Tb emission implies the presence of more optically active Tb^{3+} sites, which leads to a greater possibility for the coupling with these oxide defects and an increased PL intensity from them.

It should be noted that 325 nm (3.8 eV) excitation is not resonant with any optical absorption band of Tb^{3+}, and the observation of strong Tb^{3+} PL from the film implies the presence of a highly efficient indirect excitation process. There are two types of indirect excitation mechanisms possible: carrier-mediated excitation and dipole-dipole Förster-Dexter coupling. Previous investigations [84] on Tb-doped silicon oxynitride showed that Tb^{3+} ions can be excited efficiently by a 325 nm excitation source through a

carrier recombination process. The 325 nm He-Cd laser is able excite carriers into the extended above-band-gap states in silicon oxynitride. This process is less likely here, because the bandgap of SiO_2 is as large as 8eV [111]. Since there is no excess silicon in the oxygen-rich film, no or quite few Si-ncs are expected, and thus must be other energy transfer processes in play.

In this study, the organic molecules that came from the metal organic precursor $Tb(tmhd)_3$ during the deposition are likely to serve as sensitizers, since Tb-doped silicon oxides whose Tb incorporation is achieved through a physical method such as ion implantation or sputtering could not be excited by 325 nm excitation source [79, 81]. The presence of organic molecules has been observed from Er-doped a-Si:H prepared by *in-situ* incorporation of $Er(tmhd)_3$ [112]. Similarly, the presence of fragments of $Tb(tmhd)_3$ in the films of this study can be expected. It was found that some RE chelates have broad absorption bands and high absorption coefficients, and can serve as sensitizers to excite RE ions efficiently. A number of RE chelates have been synthesised to exploit this effect [113]. To the best of our knowledge, there has been no report on the sensitizing effect of the $Tb(tmhd)_3$ molecules employed in the present study. Further studies on the absorption properties of the film are clearly necessary.

PL spectra for Tb017 exhibit characteristic Tb^{3+} PL peaks which sit on the broad bands, while these broad bands have different spectral shapes and much greater intensities

in comparison with those of Tb016. A red shift of the broad band at 1100 °C followed by a sudden quenching at 1200 °C was observed. It is attributed to the formation of Si-ncs in local areas. The red shift and the increase of the intensity at higher annealing temperatures are typical for Si-ncs PL due to quantum confinement effects. The broad bands have a similar correlation with Tb^{3+} PL as those of Tb:SRSO samples under annealing at 1100 and 1200 °C (see section 9.1.2). The radiative oxide defects exist no matter whether there are Si-ncs in the films or not. Actually, the related broad band in the range 400-700 nm was still observed at 1200 °C when the PL of Si-ncs was quenched.

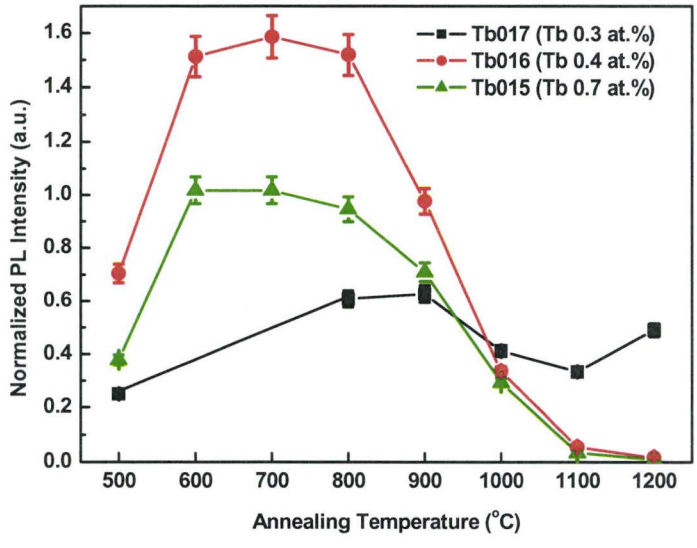

Figure 9.2 Tb^{3+}-related PL intensity at 546 nm from three Tb:ORSO samples annealed in flowing N_2 for 1hour as a function of annealing temperature.

Figure 9.2 depicts the normalized Tb^{3+} PL intensity at 546 nm for three samples with

various compositions as a function of the annealing temperature. In all cases, comparing with as-deposited samples, the PL intensities were enhanced significantly through annealing at 600 to 800 °C. At higher temperatures, the intensities generally decrease with increasing temperature (except for Tb 017).

The PL enhancement at 600 to 800 °C is possibly attributed to the reduction of coupled nonradiative oxide defects and the activation of optically active Tb^{3+}. At annealing temperatures higher than 800 °C, many RE ions tend to precipitate and their emission is quenched through ion-ion interactions. However, this is probably not the case for Tb ions. A previous study on Tb doped SiO_2 revealed that the lifetime of the Tb emission still remains almost constant at concentrations as high as 2.7 at.% [79, 81]. This result suggested that when Tb ions precipitate, the quenching of Tb^{3+} PL is due to the formation of optically inactive compounds instead of ion-ion interactions, since the latter should lead to a significant decrease of the emission lifetime. As noted previously, XAFS analysis confirmed that there existed two types of Tb sites in Tb-doped SiO_2: Tb-2O or Tb-6O, with the formation of the latter being related to the enhancement of the Tb emission [80]. In this study, Tb ions tend to form clusters at higher temperatures, and the number of oxygen atoms associated with each Tb ion is reduced, which may lead to the transformation from Tb-6O to Tb-2O and results in a decrease of the Tb emission. Another possibility is that the organic molecules could be driven out of the films or

become more unstable and begin to dissociate at higher temperatures. As a result, the available sensitizers may be reduced significantly leading to the decrease of Tb emission.

Therefore, Tb^{3+} PL quenching at temperatures higher than 800 °C is possibly attributed to two processes occurring simultaneously: the trend to form clusters which leads to the reduction of optically active Tb-6O sites and the exhaustion of available sensitizers.

9.1.2 Silicon-rich Films

Sub-section of Table 6.1

Sample	Absolute Atomic Areal Density [x10^7 atoms/ cm^2]				Si [at.%]	RE [at.%]	Thickness [Å]		Index of Refraction
	Si	O	RE	Ar			RBS	Optical	
Tb007	2.38	4.21	0.00689	0.038	36.1	0.1	1000	1053	1.57
Tb008	2.37	4.22	0.0064	0.043	35.97	0.1	1000	1025	1.58
Tb009	2.37	4.22	0.00687	0.042	35.87	0.1	1000	1015	1.57
Tb011	1.64	2.7	0.00851	0	37.74	0.2	662	716	1.65
Tb012	2.09	3.76	0.00163	0.004	35.71	0.28	900	938	1.66

Tb012 has been selected to illustrate the structural features of PL spectra of Tb:SRSO samples. Figure 9.3 shows the PL spectra of the Tb012, as deposited and annealed in flowing N_2 for 1 hour at various temperatures. A broad emission band in the range of 400-900 nm was observed from the as-deposited sample. The annealing at temperatures from 800 to 1100 °C results in an increase in the PL intensity with a red shift of the peak position. This band is probably due to the presence of

Si-ncs in the film. The enhancement of the emission intensity indicates the formation of more Si-ncs, while the red shift of the peak suggests the growth of the Si-ncs sizes. A weak emission band peaking at 546 nm emerged after anneal at 1100 °C. After annealing at 1200 °C the Si-ncs emission decreases abruptly. At the same time, the four sharp peaks centered at 487, 546, 588 and 620 nm become dominant. Both the weak 546 nm peak observed after anneal at 1100 °C and the four strong sharp peaks observed after anneal at 1200 °C are related to the 4f-4f transitions of Tb^{3+} ions.

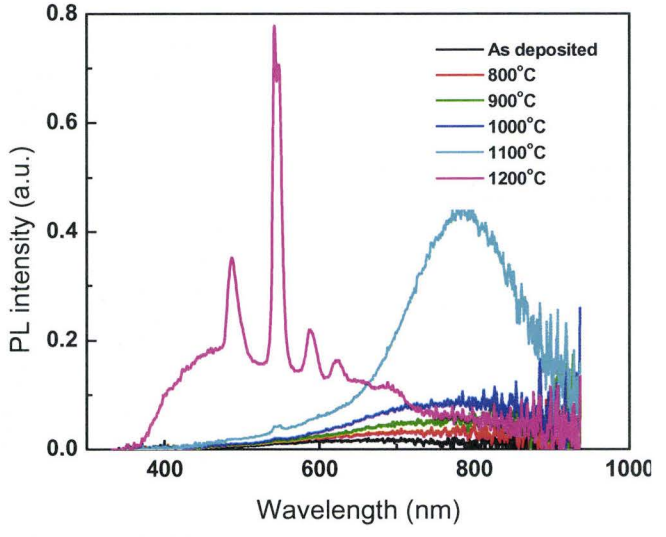

Figure 9.3 PL spectra of Tb012 as-deposited or annealed in flowing N_2 for 1 hour at various temperatures.

Since the 325 nm excitation is not resonant with any absorption band of Tb^{3+} ions, the observation of Tb^{3+} emission indicates the existence of (an) indirect excitation

mechanism(s). The simultaneous quenching of the Si-ncs emission and the abrupt increase of the Tb emission intensity after annealing at 1200 °C suggests the efficient energy transfer from Si-ncs to Tb^{3+}. Here we attribute the observed Tb emission to the exciton-mediated Förster-Dexter energy transfer process. As noted previously, although the Si-ncs PL at 1200 °C is peaking at around 800 nm (1.55eV) and at least 2.5eV (488 nm) energy is required to excite Tb^{3+}, it has been suggested that when the size of Si-ncs reduce to less than 3 nm, the actual bandgap of a Si-nc might be much greater than that indicated by its emission wavelength. The actual band gap of a 2-3 nm Si-nc could be as high as 2.5 eV as a result of quantum confinement [42], which is sufficient for the excitation of Tb^{3+}. In this study, the presence of Si-ncs in the film was confirmed by HR-TEM images which will be shown in the following section.

The Förster-Dexter model involves two possible energy transfer pathways: Förster mechanism refers to the electric dipole-dipole interaction, and a reasonable energy transfer probability can only be achieved when the distance between two dipoles (Si-nc and Tb) is below a critical value. So far there is published value for Si-nc and Tb, while for Si-ncs and Er, this value is as low as 1 nm. The Dexter mechanism involves actual electron exchanges between the acceptor and donor. The occurrence of this process requires the overlap of their wave functions. Since the wave functions of both Si-nc and Tb^{3+} are highly localized, Tb^{3+} is required to be very close to the Si-ncs [114,115].

Therefore, it is clear that in order to make Förster-Dexter energy transfer possible, an extremely small separation between Tb^{3+} and Si-nc is necessary. This could explain why the Tb^{3+} PL only becomes intense at 1200 °C. The distance between Tb^{3+} and Si-nc decreases progressively with the increasing of number and size of Si-ncs. At 1200 °C the distance decreased to the "critical radius" and the significant increase of the energy transfer probability makes the quenching of Si-ncs and Tb emission much more pronounced.

Although the organic sensitizer- the fragments of Tb $(tmhd)_3$ may also be present in the silicon rich films, the absence of Tb emission from the as-deposited samples and those annealed between 800 and 1200 °C indicates that the corresponding excitation is not quite as efficient in silicon-rich films. One possible explanation is that the Si-ncs are dominant in the absorption of excitation photons due to their relatively high absorption coefficient [43]. In particular, the organic sensitizers are unlikely to be responsible for the strong Tb emission when annealed at 1200 °C, since the Tb^{3+} PL intensity of the silicon-rich sample Tb012 is 50 times greater than that of the oxygen-rich sample Tb016 at this temperature, while they have comparable Tb concentrations.

Figure 9.4 shows the normalized peak intensity of Si-ncs PL for the Tb:SRSO samples with various Tb concentrations as a function of the annealing temperature. Tb007, 008 and 009 have very similar compositions and PL spectra for the annealing conditions

discussed in this study, thus only the PL data of Tb009 are presented here in comparison with the samples of different compositions. The inset shows the Tb^{3+} PL intensity at 546 nm for samples annealed at 1200 °C as a function of Tb concentration. When annealed at 1200 °C, the Tb PL intensity increases with Tb concentration, which can be explained by the increase of optically active Tb^{3+} sites. The Si-ncs emission was observed to decrease with Tb concentration at annealing temperatures greater than 900 °C. Although Tb emission was only appreciable from the samples annealed at 1100 and 1200 °C, this decrease indicates that the energy transfer between Tb^{3+} ions and Si-ncs is also occurring at 1000 °C, thereby suppressing the Si-ncs PL.

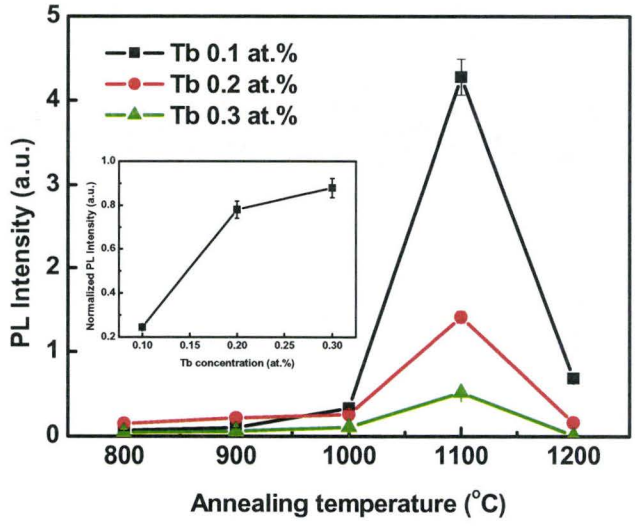

Figure 9.4 PL peak intensities of Si-ncs for Tb:SRSO samples with various Tb concentrations annealed in flowing N_2 for 1 hour as a function of the annealing temperature. The inset shows the Tb^{3+} PL intensity at 546 nm for annealing at 1200 °C as a function of Tb concentration.

9.2 Evolution of PL with Hydrogenation Annealing

9.2.1 Oxygen-rich Films

This section investigates the effects of hydrogenation annealing on the PL spectra of Tb:ORSO films. Figure 9.5 shows the PL spectra of Tb016 annealed in flowing Ar + 5% H_2 for 1 hour at various temperatures. Four characteristic Tb^{3+} PL peaks can be clearly seen. The 400–700 nm broad bands related to radiative oxide defects are less pronounced in comparison with N_2 annealing for temperatures lower than 1200 °C, while at 1200 °C a broad band in the range 400-800 nm emerges. It is likely indicative of the formation of a small quantity of Si-ncs with a wide size range.

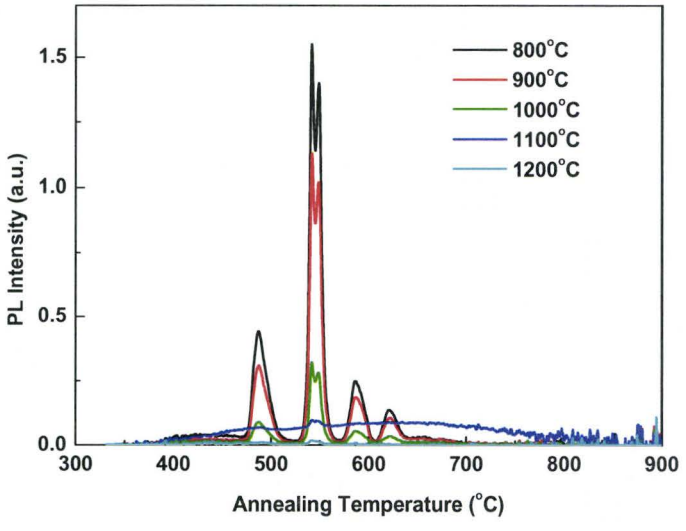

Figure 9.5 PL spectra of Tb 016 annealed in flowing Ar + 5% H_2 for 1 hour at various temperatures.

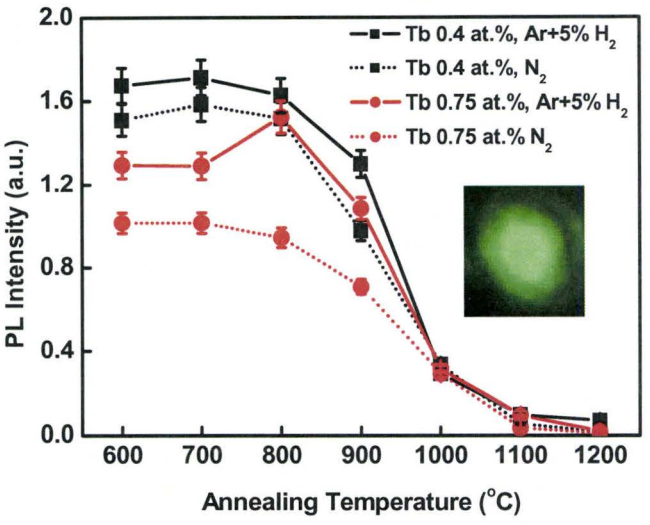

Figure 9.6 The comparison of normalized Tb^{3+}-related PL intensity at 546 nm as a function of annealing temperature for annealing in Ar + 5% H_2 and N_2 for 1 hour, respectively.

Figure 9.6 depicts the normalized Tb^{3+} PL intensity at 546 nm for two samples annealed in Ar + 5% H_2 for 1 hour as a function of the annealing temperature. The corresponding data for N_2 annealing is also given for comparison. For the both samples, the hydrogenation annealing causes greater PL intensities at all annealing temperatures. This may suggest that the hydrogenation ambient is advantageous to the reduction of the radiative oxide defects coupled to the optically active Tb^{3+}. As a result, the oxide defect PL decreased and the Tb^{3+} PL increased. It has been proposed that in SRSO the presence of dangling bonds at the Si-ncs/matrix interface prevents light emission from Si-ncs, and hydrogenation annealing can enhance the PL of Si-ncs through passivating these dangling bonds [105, 106]. This process is likely responsible for the observation of a Si-ncs related

peak at 1200 °C in this work.

9.2.2 Silicon-rich Films

Figure 9.7 shows the PL spectra of Tb012 annealed in flowing Ar + 5% H_2 for 1 hour at various temperatures. The evolution of the PL spectra is analogous to the case of N_2 annealing. An increase in the Si-ncs PL intensity with a slight red shift of the peak position is observed from 800 to 1100 °C, followed by an abrupt quenching at 1200 °C. The Tb^{3+} PL emerges at 1000 °C and increases with increasing annealing temperature, but it exhibits a much weaker intensity in comparison with the case of N_2 annealing.

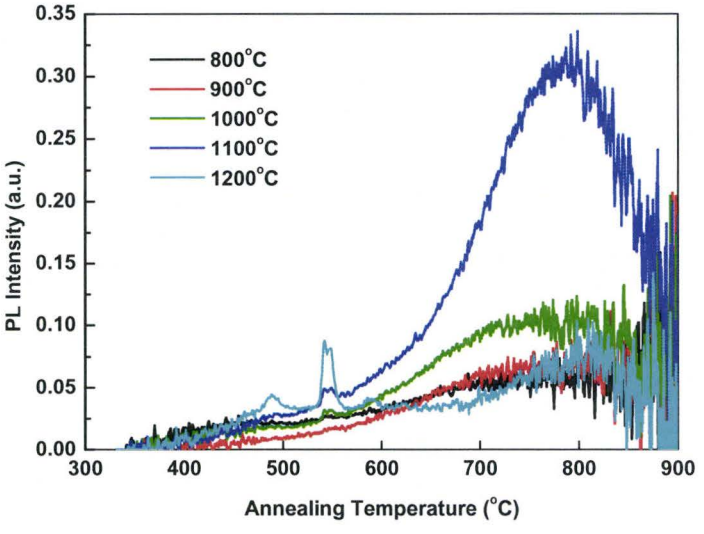

Figure 9.7 PL spectra of Tb 012 annealed in flowing Ar + 5% H_2 for 1 hour at various temperatures.

Figure 9.8 depicts the normalized PL intensities of Si-ncs for Tb:SRSO annealed in

flowing Ar + 5% H_2 and N_2 for 1 hour as a function of the annealing temperature. Hydrogenation annealing results in lower PL intensities at most of temperatures except for 800 and 1200 °C.

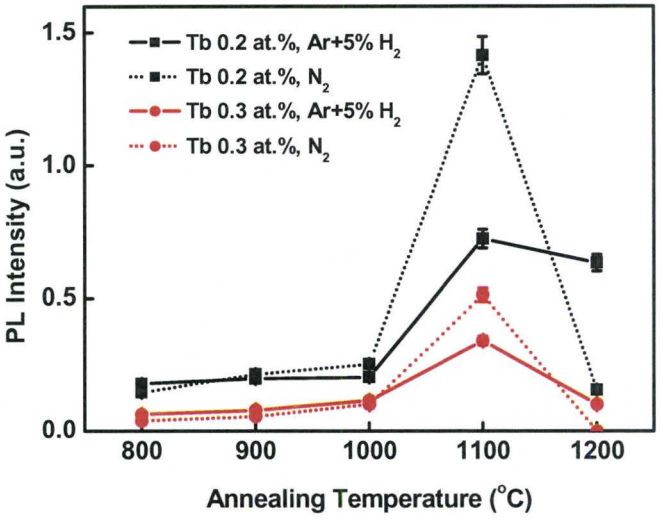

Figure 9.8 Normalized PL intensities of Si-ncs for two Tb:SRSO samples annealed in flowing Ar + 5% H_2 and N_2 for 1 hour as a function of annealing temperature.

The enhancement of Si-ncs PL for hydrogenation annealing at 800 °C is likely due to the passivation effects of the dangling bonds on the surface of Si-ncs. In the above section, it has been proposed that the Tb^{3+} emission from Tb:SRSO films can be excited through the Förster-Dexter energy transfer process between Si-ncs and Tb ions, and the efficiency of this process is highly dependent on the distance between Si-ncs and Tb ions. The "directional" diffusion effect possibly leads to the situation that the distance between

Si-ncs and Tb ions decreased to a certain value at lower annealing temperatures. A more efficient coupling quenched Si-ncs emission result in a lower Si-ncs PL from 900 to 1100 °C. At the same time, the other effect of the directional diffusion is that more Tb ions are accumulated near the surface of Si-ncs. It may lead to the formation of more optically inactive Tb-2O clusters and the decoupling of Tb^{3+} and Si-ncs. This effect should become more severe at higher temperatures. As a result, lower Tb^{3+} PL and greater Si-ncs PL were observed at 1200 °C for hydrogenation annealing.

9.3 HR-TEM Results

Figure 9.9 shows the X-ray Energy Dispersive Spectroscopy (XEDS) elemental line-scan for Tb012 annealed in flowing N_2 for 1 hour at 1100 and 1200 °C. The selected elements are Si and O for 1100 °C and Si, O and Tb for 1200 °C. From the TEM images (Figure 9.9 (a), (c)), three dark to light grey layer can be clearly seen, which correspond to Si substrate, film and glue layer, respectively. The observed thickness of the film is around 950 nm, which is consistent with optical thickness measured by ellipsometry. There is almost no diffusion of O atoms from the film to the substrate for annealing at 1100°C, while diffusion lengths as large as 20 nm were observed for annealing at 1200 °C. Tb in the film was not detectable due to its very low concentration.

Figure 9.10 showed HR -TEM images for Tb012 annealed at 1100 and 1200 °C,

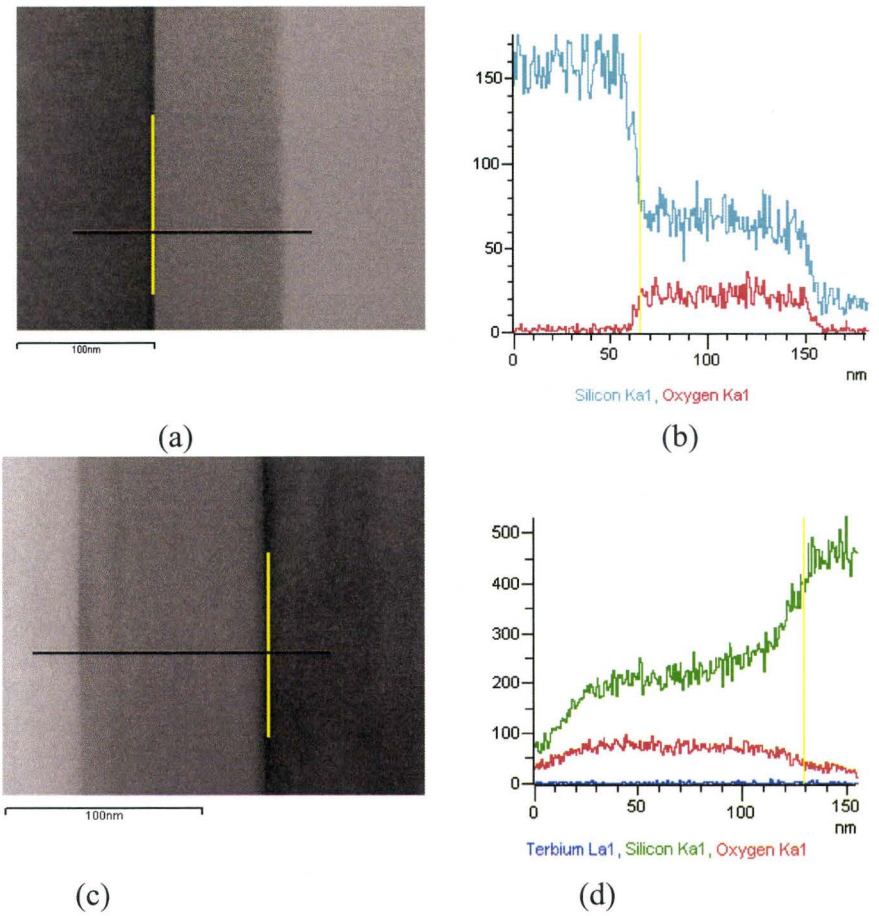

Figure 9.9 XEDS elemental line-scan analysis. TEM images containing the line-scan location for annealing in flowing N_2 for 1hour at (a) 1100 °C (c) 1200 °C. The yellow lines indicate the visual interface between the film and the substrate, and the black lines indicate the scan distance. The elemental line-scan profiles for Si, O and Tb as shown for (b) 1100 °C (d) 1200 °C.

respectively. Both images show the amorphous silicon oxide matrix containing dispersed crystalline particles which are characterized by "paralleled lattice lines". These crystalline particles are confirmed as Si-ncs by XEDS spot analysis. Although the Si-ncs sizes are not uniform, the average Si-ncs size for annealing at 1200 °C is clearly larger. This supports the observed PL results in this study, which showed a red shift at higher

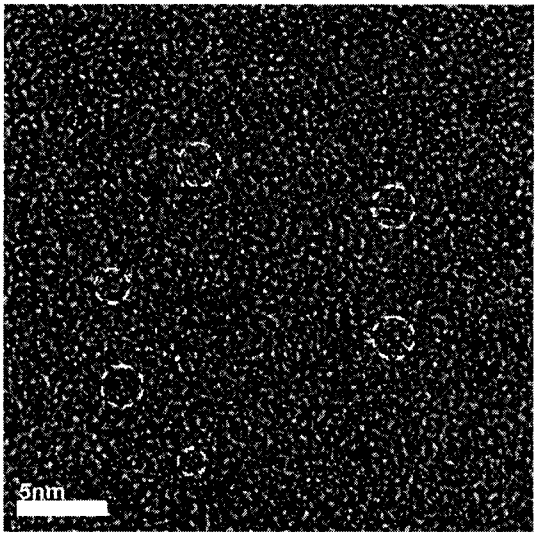

(a)

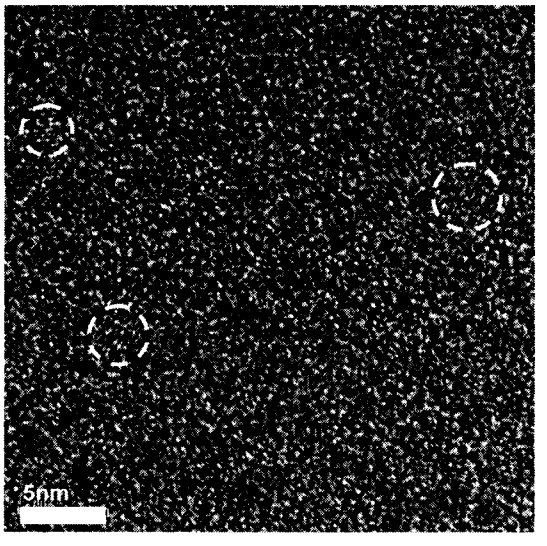

(b)

Figure 9.10 HR-TEM images of Tb012 annealed in flowing N2 for 1 hour at (a) 1100 °C (b) 1200 °C. The areas surrounded by white dashed lines indicate the crystalline particles.

temperatures. More Si-ncs can be clearly seen from the image for 1100 °C annealing, which appears to be in conflict with the trend reported in the literature: the density of Si-ncs increases with the annealing temperature. However, this observation may not

reflect the actual areal density of the Si-ncs in the films, since the TEM sample is not infinitely thin in practice, and observed Si-ncs may come from various depths of the sample. At the same time, it is also possible that some Si-ncs at lower position are blocked by higher Si-ncs and cannot be seen.

The most intense Tb^{3+} emission was observed from Tb016 annealed in flowing Ar+ 5%H_2 at 700 °C for 1 hour. The inset of Figure 9.6 shows the corresponding picture taken with a camera. The emission was quite strong and can be easily observed under bright room lighting conditions.

Chapter 10

Studies of Er-doped Silicon-rich Silicon Oxides

Sub-section of Table 6.1

Sample	Absolute Atomic Areal Density [x10^7 atoms/ cm^2]				Si [at.%]	RE [at.%]	Thickness [Å]		Index of Refraction
	Si	O	RE	Ar			RBS	Optical	
Er242	2.08	3.86	0.00721	0.040	35.09	0.12	900	903	1.57
Er243	2.75	5	0.132	0.024	35.48	1.46	1370	1352	1.59
Er244	6.34	11.4	1.01	0	35.7	4.76	766	731	1.72

Three Er:SRSO samples were annealed in flowing N_2 for 1 hour at temperatures from 800 to 1200 °C. However, for two samples with greater Er concentrations (Er243 and Er244), the films were severely damaged or completely disappeared after the annealing for all the temperatures discussed in this study. Therefore, only the PL results for Er242 are presented in this section. The cause of the damage is likely similar to that of Eu022 discussed in Chapter 8.

The visible and infra-red PL spectra for Er242, as deposited and annealed in flowing N_2 for 1 hour at various temperatures are given in Figures 10.1 (a) and (b), respectively.

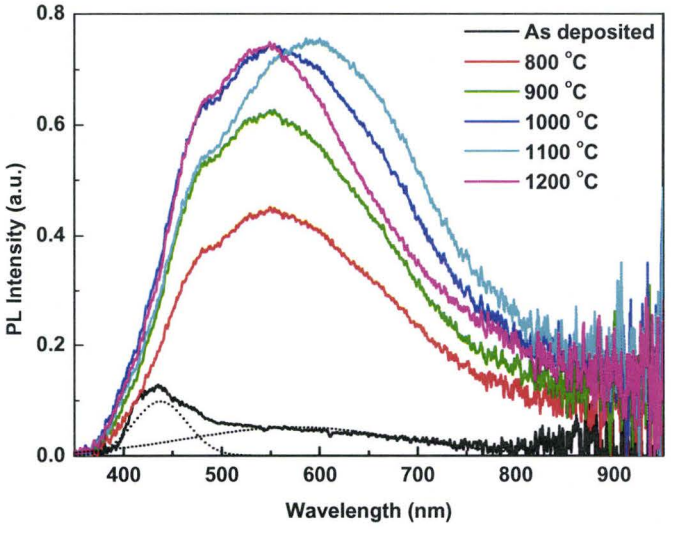

(a)

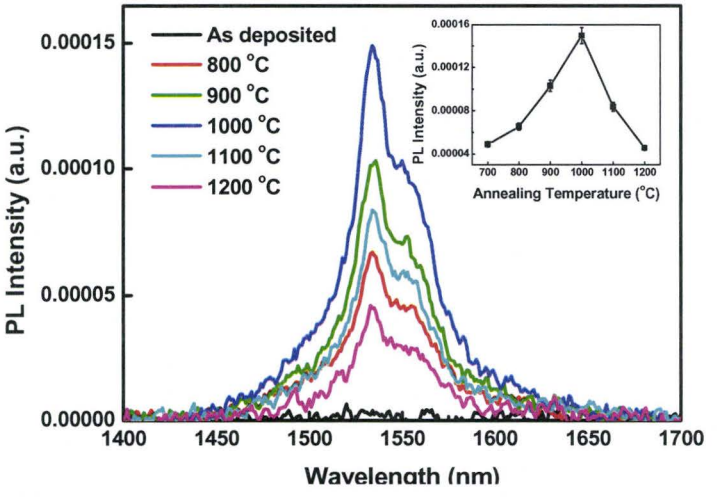

(b)

Figure 10.1 PL spectra for Er242 as deposited and annealed in flowing N_2 for 1hour at various temperatures for (a) the visible to near infra-red regime and (b) the infra-red The dashed lines indicate the two Gaussian components for the deconvolution of the PL spectrum for the as-deposited sample. The inset shows the PL intensity at 1535 nm as a function of annealing temperature. The term "AD" indicates the as-deposited condition.

In the visible regime, for the as-deposited sample, the PL spectrum's main peak is

centered at 430 nm and a long tail extends to 800 nm. This broad band can be decomposed into two Gaussian components centered at 437 and 575 nm, respectively, as indicated by the dashed lines in Figure 10.1(a). The 437 nm component is likely related to NOV, and the other very broad component may suggest the presence of Si-ncs with a wide size range. After annealing at 800 °C, the Si-nc PL becomes dominant and red shifts to 600 nm. Further increase of the PL intensity and red shift occurred at greater temperatures until 1000 °C suggest the increase of both number and size of Si-ncs. A decrease of PL intensity and blue shift were observed at 1200 °C. The decrease of PL intensity can be explained by the nonradiative Förster-Dexter energy transfer from Si-ncs to Er ions. The Si-ncs PL was only slightly quenched due to the very low Er concentration (0.12 at.% Er). As mentioned previously, the PL peak position of Si-ncs is related to their electronic states, which are determined by both Si-ncs sizes and the oxygen related surface states. The latter is possibly responsible for the observed blue shift here since Si-ncs usually tend to grow larger with increasing annealing temperature.

In the infra-red range, there is no appreciable luminescence for the sample as deposited. After annealing, the PL spectra for different temperatures are all characterized by a main peak with a weaker shoulder peaking at 1535 and 1550 nm, respectively. This line-shape is very characteristic of Er^{3+} luminescence and it is related to $^4I_{13/2}$ to $^4I_{15/2}$ transition. The Er^{3+} PL intensity increases with increasing annealing temperature up to

maximum at 1000 °C and then decreases at higher temperatures.

The increase of the Er^{3+} PL for annealing at temperatures lower than 1000 °C is possibly due to three processes occurring simultaneously. First, more optically active Er^{3+} sites formed during the annealing. EXAFS analysis has confirmed the formation of an Er-O complex with an electronic charge distribution similar to that of Er-6O [116]. Second, more Si-ncs with greater size are formed at higher temperatures as indicated by the Si-ncs PL and lead to the reduction of the distance between Er ions and Si-ncs. This process may enhance Er^{3+} PL by improving the Förster-Dexter energy transfer. Finally, oxide defects usually tend to decrease during the annealing. The decrease of the Er^{3+} PL at temperatures higher than 1000 °C is usually attributed to Er precipitation which can lead to the nonradiative energy transfer between neighbouring Er ions and result in the reduction of Er^{3+} PL. However, the Er concentration in the discussed film is quite low, so it is evident that Er ions are not uniformly distributed in the film. Er ions are more likely to accumulate near the Si-ncs surface. Since more defects are present near the interface of Si-nc and the SiO_x matrix due to their mismatched lattice parameters, more NBOs are available to accommodate Er ions. As noted previously, Er ions tend to diffuse toward Si-ncs during hydrogenation annealing. It has also been proposed that the Ostwald ripening of the Si-ncs at temperatures higher than 900 °C is related to the quenching of Er^{3+} PL. It was shown that the number of Si-ncs decreased while their sizes increased

because of Ostwald ripening, and the Förster transfer is less efficient for the larger Si-ncs [91]. However, the present study does not support this argument. The increase of the Si-ncs PL at temperatures higher than 900 °C reveals the increase of the number of Si-ncs. In the previous section for Tb:SRSO studies, although the growth of Si-ncs size at higher temperatures was confirmed by HR-TEM, the PL spectrum at 1200 °C suggests a very efficient energy transfer between Tb ions and large Si-ncs. In summary, it is possible that the main reason for the Er^{3+} PL quenching at temperatures higher than 1000 °C is the precipitation of Er ions near the Si-ncs surfaces instead of the growth of Si-ncs size. The maximum Er^{3+} PL is usually found occurring at lower annealing temperatures around 800 to 900 °C [31, 91]. The increase of the optimum annealing temperature is likely due to less precipitation for this very low Er concentration.

Chapter 11

Conclusions and Future Work

11.1 Conclusions

RE (Ce, Tb, Eu and Er) doped silicon oxide films with or without excess silicon were deposited by ECR-PECVD adapted for RE in-situ incorporation. The films were investigated in terms of their composition, PL properties, bonding structures and microstructures through RBS, PL spectroscopy, FTIR spectroscopy and HR-TEM techniques, respectively. The influence of certain deposition parameters on film composition has been studied, and the successful *in-situ* incorporation of high concentration RE ions has been achieved. The luminescence mechanisms for films with various RE doping have been investigated with the focus on the identification of RE-related luminescence centers, their thermal evolution and the coupling with other possible luminescence centers present in the films, such as Si-ncs and oxide defects. The dependence of the PL properties of the films on RE doping concentration, with or without excess Si and annealing conditions has been investigated to optimize RE-related luminescence.

In this study, it was found that the excess Si in the films can be largely controlled by varying SiH_4 and O_2 gas flow ratios, while the incorporation of RE ions was quite sensitive to a number of variables including microwave power, RE cell temperature, and Ar, SiH_4 and O_2 gas flow rates, which determine the plasma details. By varying these parameters, a series of compositions were achieved, including Si/ Si+O ratios in the range of 30–42%, and Ce, Eu, Tb and Er concentrations in the range of 0.01-0.9, 0.1-0.75, 0.02-2.15, 0.12-4.76 at.%, respectively.

Broadband Ce^{3+} emissions in the range of 350 to 700 nm were observed from oxygen-rich films. Strong Si-ncs emission peaking around 800 nm is dominant in the silicon-rich film. Ce^{3+} emission was severely quenched by the presence of Si-ncs and is not appreciable for annealing temperatures lower than 1200 °C. The most intense Ce^{3+} emission was observed from an oxygen-rich film containing a high Ce concentration (0.9 at.%) under annealing in flowing N_2 at 1200 °C for 3 hours. It is proposed that the enhancement of Ce^{3+} emission under this condition is related to the formation of cerium silicate whose presence has been confirmed by FTIR and HR-TEM analysis in this study.

Eu-doped silicon-rich films emitted strong broad PL from 400 to 800 nm, which can be decomposed into three overlapped Gaussian components peaking around 460, 540 and 640 nm. The first two components correspond to Eu^{2+} PL and the third one corresponds to the Si-ncs PL. The significant quenching of Si-PL with the presence of Eu doping

revealed the coupling between Eu ions and Si-ncs. The most intensive Eu^{2+} PL was observed from the film containing 0.12 at.% Eu under annealing in Ar+5% H_2 at 1200 °C. The formation of europium silicate under these conditions was considered responsible for this PL enhancement.

Strong Tb^{3+} emission peaks centered at 487, 546, 588 and 620 nm were observed from oxygen-rich films under nonresonant 325 nm excitation. This result revealed the presence of a sensitizer-mediated excitation mechanism, and the organic ligands introduced from $Tb(tmhd)_3$ precursor were considered as the possible candidates, while Si-ncs served as sensitizer in silicon-rich films. For silicon-rich films, Si-ncs showed strong emission peaking around 800 nm and exhibited typical quantum confinement effects when annealed at annealing temperatures lower than 1200°C. The simultaneous emergence of strong Tb^{3+} emission and quenching of Si-ncs PL under 1200 °C annealing revealed the energy transfer between Si-ncs and Tb^{3+}. HR-TEM analysis confirmed that Si-ncs of 2-3 nm formed at high annealing temperatures. The most intense Tb^{3+} emission was observed from an oxygen-rich film containing 0.4 at.% Tb under annealing in Ar + 5% H_2 at 700 °C for 1hour.

Both 1535nm Er^{3+} PL and Si-ncs PL peaking around 600-700 nm were observed from the Er:SRSO films, and the strongest Er^{3+} PL was achieved under annealing in N_2 at 1000 °C for 1hour. The severe quenching of Si-ncs PL, which is usually considered as the

evidence of Er – Si ncs coupling was not observed in this study due to the very low Er concentration in the film.

11.2 Suggestions for Future Work

Due to the time constraints of a Master program, only preliminary work has been done in this thesis. There is a lot of work necessary in the future to realize practical devices such as electrically-driven silicon-based full color light emitting devices or waveguide amplifiers. Some necessary future work related to that studied in this thesis is presented in this section.

11.2.1 Continued Materials Characterization

Severe damage was observed in the films containing high concentrations of RE doping after annealing and was considered related to the incorporation of large organic molecules during the deposition. A further investigation of the film surface morphology for the as-deposited sample through atomic force microscopy (AFM) or scanning electron microscopy (SEM) is clearly necessary. FTIR spectroscopy analysis may help to detect bonding structures of the organic molecules that are possibly present in the films.

Although the presence of cerium silicate has been confirmed by FTIR spectra and HR-TEM images, identification of the specific cerium silicate type still requires further crystalline structure analysis, such as X-ray diffraction (XRD) experiments. In this study,

FTIR spectroscopy analysis was only performed on the films with very low Ce concentration. It makes the observation of cerium silicate related absorption peaks less convincing. Therefore, depositing films with higher Ce concentrations and repeating the analysis are quite necessary.

In this thesis, the optical properties of the films were only examined by single-wavelength-excitation PL spectroscopy. It is known that 4f-4f transitions of Tb ions give rise to characteristic narrow and distinct absorption bands and luminescence lifetimes. If there is coupling between Tb ions and sensitizing centers, the absorption spectrum and luminescence lifetime will both change. Therefore, absorption, PL excitation, and time-resolved luminescence spectroscopy experiments should reveal more details on excitation mechanism of Tb ions.

The original intention of developing RE: SRSO structure was to expand the excitation wavelength range and enhance the excitation efficiency for RE luminescence through the coupling between RE ions and Si-ncs. However, for those RE elements whose luminescence is related to 5d-4f transitions, such as Ce and Eu, this study revealed that the coupling between RE ions and Si-ncs tends to quench both Si-ncs and RE luminescence. So, during the RE-related PL optimization in the future, excess Si should be avoided in the films doped with these RE elements.

11.2.2 Device Fabrication

Efforts on designing and fabricating light emitting diodes (LEDs) and Er doped waveguide amplifier (EDWA) are in progress. Conventional LEDs based on Er or Tb doped SRSO giving optimized PL results have been fabricated. Unfortunately, no appreciable emission was observed for applied DC electric fields exceeding 100 V. This result is not entirely unexpected, as it is known that the excitation of the device relies on the hot electrons impact. However, the very large band gap of SiO_2 (over 8 eV) makes efficient carrier injection quite difficult, and operating voltages near or over 100 V are necessary for the excitation. Although the presence of Si-ncs in the films can improve carrier injection by providing conduction pathways, it also increases the risk to break down the silicon oxide at high voltages by generating an inhomogeneous electric field [117]. One promising alternative matrix is silicon nitride whose band gap is only around 4 eV. A high-efficiency visible light emitting diode based on it has been demonstrated [118]. Previous work by Boudreau [90] and Tyler [119] revealed that the McMaster ECR-PECVD system has the ability to deposit silicon nitride. Thus the realization of RE doped silicon nitride based devices can be considered in the future.

With respect to EDWA, the design for ridge waveguide structures and a gain measurement system is under way. The preliminary optical simulation for the waveguide structure using commercial software RSOFT BEAM PROP indicates good confinement

of the fundamental mode in the core of the designed ridge waveguide structure. The fabrication and characterization of the device should be realized in the near future.

References

[1] J. D. Plummer, M. D. Deal and P. b. Griffin, Silicon VLSI Technology Fundamentals, Practice and Modeling, Prentice Hall, Upper Saddle River, N.J. (2000).

[2] A. Allan, D. Edenfeld, W. H. Joyner, Jr., A. B. Kahng, M. Rodgers and Y. Zorian, 2001 Technology Roadmap for Semiconductors, Computer 35, 42 (2002)

[3] L. Kimerling, Appl. Surf. Sci. 159, 8 (2000).

[4] H.W ong, V. Filip, C.K.Wong and P.S. Chung, Microelectronics Reliability, 47, 1 (2007).

[5] G. T. Reed and A. P. Knights, Silicon Photonics: An Introduction, John Wiley & Sons Ltd., Etobicoke, ON (2004).

[6] G. Masini, L. Colace and G. Assanto, Mater. Sci. & Eng., B89, 2 (2002).

[7] R. Soref, Proc. IEEE 81, 1687 (1993).

[8] Sean Koehl, Market Dynamics, Sept. 26 (2005).

[9] L. Pavesi and D. J. Lockwood, Silicon Photonics, Spring-Verlag, New York (2004).

[10] H. Rong, A. Liu, R. Jones, O. Cohen, D. Hak, R. Nicolaescu, A. Fang and M.

Paniccia, Nature, 433, 292 (2005).

[11] A. Liu, M. Paniccia, Physica E 35, 223 (2006)

[12] D. J. Lockwood, Light Emission in Silicon: From Physics to Devices, Academic Press, USA (1998)

[13] A.J.Kenyon, Progress in Quantum Electronics 26, 225 (2002).

[14] R. Reisfeld and C. K. Jorgensen, Lasers and Excited States of Rare Earths, Springer, New York (1977).

[15] G. H. Dieke, Spectra and Energy levels of Rare-Earth Ions in Crystals, Wiley, New York (1968).

[16] M. Leskela, Proc. of the SPIE - The International Society for Optical Engineering 5062, 18 (2003).

[17] N. D. Vieira Jr., I. M. Ranieri, L. V. G. Tarelho, N. U. Wetter, S. L. Baldochi, L. Gomes, P. S. F. de Matosa, W. de Rossi, G. E. C. Nogueira, L. C. Courrol, E. A. Barbosa, E. P. Maldonado and S. P. Morato, J. Alloys Compd. 344, 231 (2002).

[18] J. K. Sahu, Y. Jeong, D. J. Richardson and J. Nilsson, Opt. Commun. 227, 159 (2003).

[19] B. V. Shul'gin, V. L. Petrov, V. A. Pustovarov, V. I. Arbuzov, D. V. Raikov, K. V. Ivanovskikh, A. V. Ishchenko, Physics of The Solid State, 47, 1412 (2005).

[20] L. Galambos, S.S. Orlov, L.Hesselink, Y. Furukawa, K. Kitamura, S. Takekawa, J.

Cryst. Growth 229, 228 (2001).

[21] V.S. Sastri, J. Bunzli, V. R. Rao, G.V.S. Rayudu and J.R. Perumareddi, Modern Aspects of Rare Earths and their Complexes, Elsevier, Netherlands (2003).

[22] M. Gaft, R. Reisfel and G. Panczer, Mordern Luminescence Spectroscopy of Minerals and Materials, Springer, Germany (2005).

[23] P. G.. Kik, and A. Polman, MRS Bulletin 23, 48 (1998).

[24] A. Polman and F .C.J.M. van Veggel, J.Opt. Soc,Am.B 21, 871 (2004).

[25] A. J. Kenyon, Semicond. Sci. Technol. 20, R65 (2005).

[26] M. Flynn, J. Wojcik, S. Gujrathi, E. Irving and P. Mascher, Mater. Res. Soc. Symp. Proc. 866, V5.7.1/FF5.7.1 (2005).

[27] X. D. Pi, O. H. Y. Zalloum, J. Wojcik, A. P. Knights and P. Mascher, J. Appl. Phys. 97, 096108 (2005).

[28] D. E. Blakie, O. H. Y. Zalloum, J. Wojcik, E. J. Irving, A. P. Knights and P. Mascher, Proc. of SPIE. 5970, 13 (2005).

[29] A. Podhorodecki, J. Misiewicz, J. Wojcik, E. Irving and P. Mascher, J. Lumin. 121, 232 (2006).

[30] D. E. Blakie, O. H. Y. Zalloum, J. Wojcik, E. J. Irving, A. P. Knights and P. Mascher, Proc. of SPIE 6343, S-1(2006).

[31] X. D. Pi, O. H. Y. Zalloum, T. Roschuk, J. Wojcik, A. P. Knights, P. Mascher and

P.J. Simpson, Appl. Phys. Lett. 88, 103111 (2006).

[32] C. L. Heng, O. H. Y. Zalloum, T. Roschuk, D. Blakie, J. Wojcik and P. Mascher, Electrochem. Solid-State Lett. 10, K20 (2007).

[33] E.Desurvire, Erbium-Doped Fiber Amplifiers: Principles and Applications, John Wiley & Sons, Inc., New York (1994).

[34] P.C. Becker, N.A. Olsson and J.R.Simpson, Erbium-Doped Fiber Amplifier: Fundamentals and Technology, Academic Press, USA (1999).

[35] M. A. Marcus and A. Polman, J. Non-Crystalline Solids 136, 260 (1991).

[36] D. L. Adler, D. C. Jacobson, D. J. Eaglesham, M. A. Marcus, J. L. Benton, J. M. Poate and P. H. Citrin, Appl. Phys. Lett. 61, 2181 (1992).

[37] K.Arai, H. N amikawa, K.Kumata, T.Honda, Y. Ishii and T.Handa, J. Appl. Phys. 59, 3430 (1986).

[38] M.Achtenhagen, R.J.Beeson, F.Pan, B.Nyman and A.Hardy, J. Lightwave Technology, 19, 1521 (2001).

[39] G.Franzò, V.Vinciguerra, F.Priolo, Applied Physics A: Mater. Sci. Process. 69, 3 (1999).

[40] C. S trohhöfer and A. Polman, Appl. Phys. Lett. 81, 19 (2002).

[41] O. Park, S.Seo and B. Bae, Proc. of SPIE - The International Society for Optical Engineering, 4990, 62 (2003).

[42] M. V. Wolkin, J. Jorne, P. M. Fauchet, G. Allan and C. Delerue, Phys. Rev. Lett. 82, 197 (1999).

[43] T. Roschuk, J. Wojcik, E. A. Irving, M. Flynn and P. Mascher, Proc. of SPIE 5577, 450 (2004).

[44] N. Daldosso, G. Das, S. Larcheri, G. Mariotto, G. Dalba, L. Pavesi, A. Irrera, F. Priolo, F. Iacona, F. Rocca, J. Appl. Phys. 101, 113510 (2007).

[45] P.G. Kik, A. Polman, Mater. Sci. Engin. B 81, 3 (2001).

[46] P. G. Kik, M. L. Brongersma and A. Polman, Appl. Phys. Lett. 76, 2325 (2000).

[47] A.J. Kenyon, P. F. Trwoga, C. W. Pitt and G.. J. Rehm, J. Appl. Phys. 79, 9291 (1996).

[48] J. Lee, J. Shin and N. Park, J. Li ghtwave Technology 23, 19 (2005).

[49] A. Paul, M. Mullholl and and M. S. Zaman, J. Mater. Sci. 11, 2082 (1976).

[50] G. H. Siegel Jr., J. Non-Cryst. Solids 13, 372 (1973).

[51] M. Yamaga, D. Lee, B. Henderson, T. P. J. Han, H. G. Gallgher and T. Yoside, J. Phys: Condens, Matter 10, 3223 (1998).

[52] R. Reisfeld , A. Patra, G. Panczer and M. Gaft, Opt. Mater. 13, 81（1999）.

[53] R. Reisfeld, H. Minti a, A. Patra, D. Ganguli and M. Gaft, Spectrochimica. Acta. Part A 54, 43 (1998).

[54] G. Q. Xu, Z. X. Zheng, W. M. Tang, and Y. C. Wu, J. Lumin. 124, 151 (2007).

[55] G. Q. Xu, Z. X. Zheng, W. M. Tang and Y. C. Wu, J. Lumin. 126, 475 (2007).

[56] H. Bi, W. Cai, H. Shi, B. Yao and L. Zhang, J. Phys. D: Appl. Phys. 33, 2369 (2000).

[57] A. H. Morshed, M. E. Moussa, S. M. Bedair, R. Leonard, S. X. Liu and N. E. Masry, Appl. Phys. Lett. 70, 1647 (1997).

[58] G. E. Malashkevich, E. N. Poddenezhny and I. M. Melnichenko, J. Non-Cryst. Solids 188,107 (1995).

[59] W. C. Choi, H. N. Lee, E. K. Kim, C. Seoul, Y. Kim, C. Park , H. C. Kim, J.Y. Lee and Y. Ku, Appl. Phys. Lett. 75, 2389 (1999).

[60] W. C. Choi, H.N.Lee, Y. Kim, H. M. Park and E. K. Kim, Jpn. J. Appl. Phys. 38, 6392 (1999).

[61] L. Kepinski, D. Hreniak and W. Strek, J. Alloys Compd. 341, 203 (2002).

[62] L. Kepinski, M.Wolcyrz, M. Marchewka, J.Solid State Chem. 168, 110 (2002).

[63] G. Qian, M. Wang, X. Fan and Z. Hong, J. Lumin. 75, 63 (1997).

[64] G. Stein and E. Wurzberg, J. Chem. Phys. 62, 208 (1975).

[65] Y. Zhou, Y. L. Lam, S. S. Wang, H. L. Liu, C. H. Kam and Y. C. Chan, Appl. Phys. Lett. 71, 587 (1997).

[66] H. N. Russell, W. Albertson and D. N. Davis, Phys.Rev. 60, 641 (1941)

[67] H. Murrieta, S. J. Hernandez, A. Rubio and O.J. Kinam, Journal of Alloys and

Compounds, 75, 121 (1983)

[68] J. A. Caird, Cr ystalline Paramagnetic Ion Lasers, CRC, Handbook of Laser Science and Technology (Suppl 1), M.J. Weber (Ed.), CRC Press, Boca Raton, FL (1998).

[69] J. Garc´ıa, M.A. Mondragón, O. Maya, A. Campero, Journal of Alloys and Compounds, 275-277, 273 (1998).

[70] M. Nogami, T. Yamazaki and Y. Abe, J. Lumin. 78, 63 (1998).

[71] J. Qi, T. Matsumoto, M. Tanaka and Y. Masumoto, J. Phys. D: Appl. Phys. 33, 2074 (2000).

[72] F. Liu, M. Zhua, L. Wanga and Y. Houb, Journal of Alloys and Compounds. 311, 93 (2000).

[73] H. Tsuboi, K. Soga, H. Inone, A. Makishima, J. Am. Ceram. Soc. 81, 1197 (1998).

[74] E. Kaldis, P. Streit and P. Wachter, J. Phys. Chem. Solids. 32, 159 (1971).

[75] K. Machida, G. Adachi, J. Shiokawa, M. Shimada, M. Koizumi, K. Suito and A. Onodera, Inorg. Chem. 21, 1512 (1982).

[76] M. W. Shafer, J. Appl. Phys. 36, 1145 (1965).

[77] W. T. Carnall, P. R. Fields and K. Rajank, J. Chem. Phys. 49, 4447 (1968).

[78] S. P . Depinna and, D. J. Dunston, Philos. Mag. B50, 579 (1984).

[79] H. Amekura, A. Eckau, R. Carius, and Ch. Buchal, J. Appl. Phys. 84, 3867 (1998).

[80] H. Ofuchi,, Y. Imaizumi, H. Sugawara, H. Fujioka, M. Oshima andY. Takeda, Nucl.

Instrum. Methods Phys. Res. B 199, 231 (2003).

[81] H. Amekura, A. Eckau, R. Carius, and Ch. Buchal, Proc. of the International Conference on Ion Implantation Technology 2, 925 (1999).

[82] M.Y oshihara, A. Sekiya, T. Morita, K. Ishii, S. Shimoto, S. Sakai and Y. Ohki, Phys. D: Appl. Phys. 30, 1908 (1997).

[83] S. Seo and J. Shin, Appl. Phys. Lett. 84, 4379 (2004).

[84] H. Jeong, S.Seo, J. Shin, Appl. Phys. Lett. 88, 161910 (2006).

[85] G . Franzò, V. Vinciguerra, F. Priolo, Appl. Phys. A 69, 3 (1999).

[86] S. Ossicini, F.Iori, E. Degoli, E. Luppi, R. Magri, R. Poli, G. Cantele, F. Trani, D. Ninno, IEEE Journal of Selected Topics in Quantum Electronics, 12, 1585 (2006).

[87] S. S. R ink, C. M. Varma and A. F. J. Levi, Phys. Rev. Lett. 66, 2782 (1991).

[88] J. von Behren, T. Van Buuren, M. Zacharias, E. H. Chimowitz and P. M. Fauchet, Solid State Commun. 105, 317 (1998).

[89] S. Schupple r, Phys. Rev. B 52, 4910 (1995).

[90] M. G. Boudreau, SiOxNy Waveguides Deposited by ECR-PECVD, M.Eng. Thesis, McMaster University (1993).

[91] D. E. Blakie, Coupled Luminescence Centres in Erbium-Doped Silicon Rich Silicon Oxide Thin Films Deposited by ECR-PECVD, M.A.Sc thesis, McMaster University (2006).

[92] L.C. Feldman, J. W. Mayer, Fundamentals of surface and thin film analysis, Elsevier, New York (1986).

[93] W. N. Lennard, Notes on Ion Beam Techniques, Department of Physics and Astronomy, University of Western Ontario (2004). Available online at publish.uwo.ca/~wlennard/.

[94] O. H. Y. Zalloum, M. Flynn, T. Roschuk, J. Wojcik, E. Irving and P. Mascher, Rev. Sci. Instrum. 77, 023907 (2006).

[95] Brockhouse Institute for Materials Research Canadian Centre for Electron Microscopy, Preparation Instructions for TEM samples, Mcmaster University (2006).

[96] S. Munekuni, T. Yamanaka, Y. Shimogaichi, R. Tohmon, Y. Ohki, K. Nasagawa, and Y. Hama, J. Appl. Phys. 68, 1212 (1990).

[97] M. A. Stevens Kalceff and M. R. Phillips , Phys. Rev. B 52, 3122 (1995).

[98] A. Paleari, N. Chiodini, D. Di Martino and F. Meinardi, Phys. Rev. B 71, 075101 (2005).

[99] H. J. Fitting, A. N. Trukhin, T. Barfels, B. Schmidt and A. V. Czarnowski, Radiat. Eff. Defects Solids 157, 575 (2002).

[100] H. Nishikawa, E. Watanabe, D. Ito, Y. Sakurai, K. Nagasawa and Y. Ohki,J. Appl. Phys. 80, 3513 (1996).

[101] Y. Sakurai and K. Nagasawa, J.Appl. Phys. 88, 168 (2000).

[102] M. Vollmer and A. Weber, Z. Phys. Chem., Stoechiom. 119, 227 (1926).

[103] R. Becher and W. Doring, Ann. Phys. 24, 719 (1935).

[104] S. K. Estreicher, J. L. Hastings, P. A. Fedders, Phys. Rev. B 57, R12663 (1998).

[105] A. R. Wilkinson and R. G. Elliman, Appl. Phys. Lett. 83, 5512 (2003).

[106] A. R. Wilkinson and R. G. Elliman, J. Appl. Phys. 96, 4018 (2004).

[107] D. Comedi, O. H. Y. Zalloum, and P. Mascher, Appl. Phys. Lett. 87, 213110 (2005).

[108] F. Iacona, C. Bongiorno, C. Spinella, S. Boninelli, and F. Priolo, J. Appl. Phys. 95, 3723 (2004).

[109] N. M. Park, T. Y. Kim, K. H. Kim, G.Y. Sung, K. S. Cho, J. H. Shin, B. H. Kim, S. J. Park, J. K. Lee, and M. Nastasi, Electrochemical and Solid-State Letters 8, G63 (2005).

[110] A. Polman, D. C. Jacobson, A. Lidgard, J. M. Poate, Nucl. Instrum. Methods Phys. Res. B 59, 1313 (1991).

[111] M. E. Castagna, S. Coffa, M. Monaco, L. Caristia, A. Messina, R. Mangano and C. Bongiorno, Physica E. 16, 547 (2003).

[112] L. R. Tessler, J. L. Coffer, J. Ji, and R. A. Senter, J. Non-Crystalline Sol. 299, 673 (2002).

[113] J. Thompson, R. I. R.Blyth, V. Arima, Y. Zou, R. Fink and E. Umbach , Mater. Sci.

Eng. B 105, 41 (2003).

[114] D. L. Dexter, J. Chem. Phys. 21, 836 (1953).

[115] A. J. Kenyon and F. Lucarz, Electrochem. Soc. Proc. 2004-13, 255 (2005).

[116] C. Maurizio, R. D'Acapito, F. Priolo, G. Franzò, F. Iacona, E. Borsella, S. Padovani, and P. Mazzoldi, Opt. Mater. 27, 900 (2005).

[117] J. M. Sun, W. Skorupa, T. Dekorsky, M. Helm, A. N. Nazarov, and R. Rizk, Opt. Mater. 27, 1050 (2005).

[118] S. Cho, N. Park, T. Y. Kim, K. H. Kim, G. Y. Sung and J. H. Shin, Appl. Phys. Lett. 86, 071909 (2005).

[119] Tyler Roschuk, Characterization of Amorphous Silicon (a-Si) and Silicon Rich Silicon Oxide Materials Produced by ECR-PECVD, McMaster University (2005).